Surface and Interface Characterization by X-ray and Electron Spectroscopies - Revealing the Peculiarities of $Cu(In,Ga)Se_2$ Chalcopyrite and $CH_3NH_3PbI_{(3-x)}Cl_x$ Perovskite-based Thin Film Solar Cell Structures

Von der Fakultät für MINT - Mathematik, Informatik, Physik,
Elektro- und Informationstechnik
der Brandenburgischen Technischen Universität Cottbus-Senftenberg

zur Erlangung des akademischen Grades

Doktor der Naturwissenschaften
(Dr. rer. nat.)

genehmigte Dissertation

vorgelegt von

M. Sc.
Evelyn Handick

geboren am 12.11.1987 in Würzburg

Gutachter: Prof. Dr. Marcus Bär
Gutachter: Prof. Dr. Dieter Schmeißer
Gutachter: Prof. Dr. Bernd Rech
Tag der mündlichen Prüfung: 07. April 2017

For my parents and my sister
...for always believing in me

Abstract

This thesis focuses on the investigation and characterization of the surfaces and interfaces of chalcopyrite-based Cu(In,Ga)Se_2 (CIGSe) and organo-metal mixed halide perovskites, specifically $CH_3NH_3PbI_{(3-x)}Cl_x$, thin film solar cells using various x-ray and electron spectroscopies. In particular, the impact of alkali treatments on the chemical and electronic surface and near-surface structure of CIGSe absorbers is studied. For $CH_3NH_3PbI_{(3-x)}Cl_x$ the compound formation is monitored and the peculiarities of the interface formation of $CH_3NH_3PbI_{(3-x)}Cl_x$ on compact and mesoporous TiO_2 are examined.

Laboratory-based photoelectron spectroscopy (XPS) and synchrotron-based hard x-ray photoelectron spectroscopy (HAXPES) are used to gain a depth-dependent picture of the chemical structure in the surface and near-surface region of CIGSe and the influence of NaF and NaF/KF post-deposition treatments (PDT) on alkali-free CIGSe absorbers. Two different absorber series are studied using an alkali-rich and an alkali-poor PDT, each consisting of an alkali-free, NaF-PDT, and NaF/KF-PDT sample. The alkali-free and NaF-PDT absorbers show similar chemical properties, having a Cu- and Ga-depleted surface region and the same chemical environment for indium and selenium is revealed by deriving the modified Auger parameter α'(In) and α'(Se) using the kinetic energy of most the prominent Auger line together with the binding energy of the chosen core level. For both NaF/KF-PDT samples a K-In-Se compound is present on top of a Cu-In-Ga-Se compound, with a nanopatterned surface being more distinct for the alkali-rich treatment. The alkali-poor NaF/KF-PDT shows a further Cu- and Ga-depletion compared to the alkali-free and NaF-PDT sample and the alkali-rich NaF/KF-PDT has a surface region almost devoid of Cu and Ga. The findings of the depth-dependent measurements reveal a bilayer structure of K-In-Se/Cu-In-Ga-Se for the NaF/KF-PDT absorbers. This is in agreement with x-ray emission spectroscopy (XES) studying the local Se density of occupied states showing the same chemical environment for alkali-free and NaF-PDT CIGSe samples. For the NaF/KF-PDT an additional feature is exhibited indicating the formation of Se-K bonds which is more distinct for the alkali-rich NaF/KF-PDT sample.
The findings of the chemical structure also reflect on the electronic structure. Here, ultraviolet photoelectron spectroscopy (UPS) and HAXPES is used to gain a depth-dependent picture of the valence band region and valence band maximum (VBM). Inverse photoemission (IPES) is used to determine the position of the conduction band minimum (CBM). The alkali-free and NaF-PDT samples as well as the alkali-poor NaF/KF-PDT sample exhibit almost the same shift in VBM away from the Fermi level (E_F) for more surface sensitive

measurements. For the alkali-rich NaF-PDT sample a near-surface electronic band gap of E_g^{surf}=(1.61[+0.14/-0.51]) eV is observed. In contrast, a large and more gradual change towards the surface is obtained for the alkali-rich NaF/KF-PDT absorber. Here, a significant band gap widening of the surface is observed with E_g^{surf}=(2.52[+0.14/-0.51]) eV. This can be ascribed to the formation of a K-In-Se surface compound and a Cu- and Ga-devoid surface region.

To in-situ monitor the compound formation of $CH_3NH_3PbI_{(3-x)}Cl_x$ on compact TiO_2 (c-TiO_2) HAXPES is used. While annealing a drop-casted layer of precursor solution on c-TiO_2 shifts in perovskite core levels during the transition temperature of 80-100°C are observed. The complete formation of the film to perovskite is confirmed with a standard $CH_3NH_3PbI_{(3-x)}Cl_x$ on c-TiO_2 sample with a nominal thickness of 300 nm. Further the Cl signal decrease at the onset of annealing and shows a depletion in the surface region above annealing temperatures of 50°C.
The chemical and electronic structure of $CH_3NH_3PbI_{(3-x)}Cl_x$ on mesoporous TiO_2 (mp-TiO_2) and c-TiO_2 using nominal perovskite layer thickness of 10, 30, 60, and 300 nm is studied with HAXPES. With increasing layer thickness the perovskite related peaks increase, while the substrate related core levels attenuate. For thinner layers, especially on mp-TiO_2, a second species is forming indicating the formation of Pb-Ti-(I) bonds. On c-TiO_2 metallic lead is present for thicker layers. All studied absorbers show island formation which is confirmed with scanning electron microscopy (SEM). Further, for both structures on mp- and c-TiO_2 thickness induced core level shifts are determined.
This thickness induced shift is also present for the electronic structure within the VBM. A shift away from E_F is determined for thinner layers revealing the influence of TiO_2 valence states. VBM values of about 1.6-1.7 ($\pm$0.1) eV are observed for layers where the VBM is mainly derived of iodine states from the perovskite cover layer. VBM positions of (3.27$\pm$0.10) eV and (3.62$\pm$0.1) eV are determined for c-TiO_2 and mp-TiO_2, respectively. For both structure types on mp- and c-TiO_2 valence band offsets (VBO) of about 1.6 eV considering interface induced band bending (IIBB) with an average IIBB value of (-0.10$\pm$0.19) eV for 10 nm perovskite on c-TiO_2 and (-0.30$\pm$0.19) eV for 10 nm perovskite on mp-TiO_2 is derived.

In the last years chalcopyrite-based solar cells reached a recent boost in efficiency due to alkali treatments. The findings of this thesis give insight on the beneficial effects caused by the treatments. The chemical and electronic changes at the absorber surface are characterized.

This will help to further improve the buffer/absorber interface in the future. The material properties of the $CH_3NH_3PbI_{(3-x)}Cl_x$ / TiO_2 interface are probed. The findings will help to comprehend favorable or detrimental effects on device performance in future.

Contents

1

Introduction

The challenges in energy production and the urgent energy revolution led to an awakening demand in renewable energies. Especially thin film solar cells gained more and more interest compared to the already established silicon solar cells. One of the main advantages of thin film solar cells is the promise to reduce production cost and the direct band gap, resulting in a higher absorption coefficient, for those materials. Two of the most promising candidates are chalcopyrite-based $Cu(In_{1-x},Ga_x)(S_ySe_{1-y})_2$ (CIGSSe) and inorganic-organic halide perovskite $CH_3NH_3PbI_{(3-x)}Cl_x$ solar cells to supersede Si solar cells. Recent progress has led to conversion efficiencies for CIGSSe and perovskite solar cells over 22%. [1–3]

On the one hand, for chalcopyrite-based (CIGSSe) solar cells the recent boost in power conversion efficiencies was mainly brought about by using alkali post-deposition treatments (PDT), in particular NaF and/or KF and lately also RbF and CsF. This trend for CIGSe solar cells started gaining a new record efficiency at that time of 20.4% [4] using a combination of NaF/KF-PDT for CIGSe on polyamide foil, an alkali-free substrate material. It is been well establish, that Na diffusion into the absorber from the substrate material through the Mo layer, in general soda lime glass, has a beneficial effect on device performance. So not

only for alkali-free substrates, like poylimide foil, a NaF-PDT led to further improve device efficiency without relying on the sodium diffusion from the substrate. Especially the additional incorporation of other alkali elements, also on alkali-containing substrates led to a constant improvement in device performances for $Cu(In_{1-x},Ga_x)(S_ySe_{1-y})_2$ within the last three years.[1, 2, 5–7]

On the other hand, the new and fast-emerging hybrid organic-inorganic perovskite-based solar cells, e.g. $CH_3NH_3PbI_3$ and $CH_3NH_3PbI_{(3-x)}Cl_x$, that started 2009 with an efficiency of 3.8% [8] exceeding now 22% [3]. This steep increasing in efficiency over the past few years is achieved through different improvements and changes within the solar cell structure, by varying the organic and/or inorganic part and different types of layer structure using mesoporous or planar electron transport materials.[9–14] Further, the addition of chlorine led to an increase in efficiencies.[14–17]

To constantly improve device efficiencies and to overcome theoretical limits for single-junction solar cells, tandem solar cells in various device structure are fabricated using advantages of two absorber structures. In the last few years the fabrication of such tandem solar cells with perovskite-based solar cells as top cells have gained more and more interested. Not only in the combination of high-efficient silicon solar cells [18, 19] but also the use of chalcopyrite-based solar cells is emerging.[19–21]

The aim of this thesis is to understand the crucial surfaces and interfaces of the two most promising thin film solar cells, in particular $Cu(In,Ga)Se_2$ and $CH_3NH_3PbI_{(3-x)}Cl_x$ by characterizing the chemical and electronic properties and relate them to device performances.
The beneficial role of alkali treatments on CIGSe-based absorbers and the influence on topography, the chemical, and electronic structure is not yet fully understood. Especially the chemical and electronic properties between the absorber surface and the adjacent emitter is of interest.
For $CH_3NH_3PbI_{(3-x)}Cl_x$ the fundamental properties regarding the material composition, electronic structures, and role of chlorine are not yet understood.
Therefore we used a variety of non-destructive depth-dependent laboratory- and synchrotron-based electron and x-ray spectroscopies to study the topography, chemical, and electronic properties of those two thin film solar cell absorbers and related structures.

In chapter 2 the two types of solar cell structures which are studied within this thesis are introduced.

Chapter 3 focuses on the theoretical description of the applied measurement techniques, analysis methods and data evaluation applied to characterize the absorber surfaces and interfaces, and the experimental details on the used instrumentations.

The effect of alkali post-deposition treatment on the topography of Cu(In,Ga)Se_2 absorbers, the chemical structure, in particular the influence of potassium on the surface and near-surface structure of CIGSe, and the electronic structure will be elucidated in Chapter 4.

Chapter 5 discusses compound formation from precursor solution to $CH_3NH_3PbI_{(3-x)}Cl_x$, which was monitored during in-situ annealing and the presence of chlorine, the chemical and electronic properties of the interface between $CH_3NH_3PbI_{(3-x)}Cl_x$ and the most common electron transport materials mesoporous and compact TiO_2.

2

Studied Thin Film Solar Cell Structures

In this chapter a brief introduction on the basics of thin film solar cells as energy conversion devices will be given. The main focus will be on the two types of solar cell absorbers, namely chalcopyrites and mixed-halide perovskites, which are studied within this thesis.

In a solar cell photons with an energy hν greater than the band gap E_g get absorbed and excite electrons from the valence band into the conduction band. The hereby generated electron-hole pairs get separated by an internal voltage generated by, e.g. a pn-junction. One can differentiate between two types of pn-junctions, either a pn-homojunction where one semi-conducting material gets doped differently or the pn-heterojunction where a n-doped material and a p-doped material are different.
To absorb the highest amount of photons in the solar cell absorber the band gap should match the terrestrial sun spectrum which is displayed in the left panel of Figure 2.1. Here the solar spectrum is shown under mean-earth distance sun-air mass AM (AM0 - extraterrestrial) just outside the Earth's atmosphere and under AM1.5. Here the solar radiation passes 1.5 times the atmosphere under not perpendicular incidence. This causes losses in intensity due to scattering and absorption.
AM1.5 conditions are also used to test the efficiencies η of the respective solar cells and

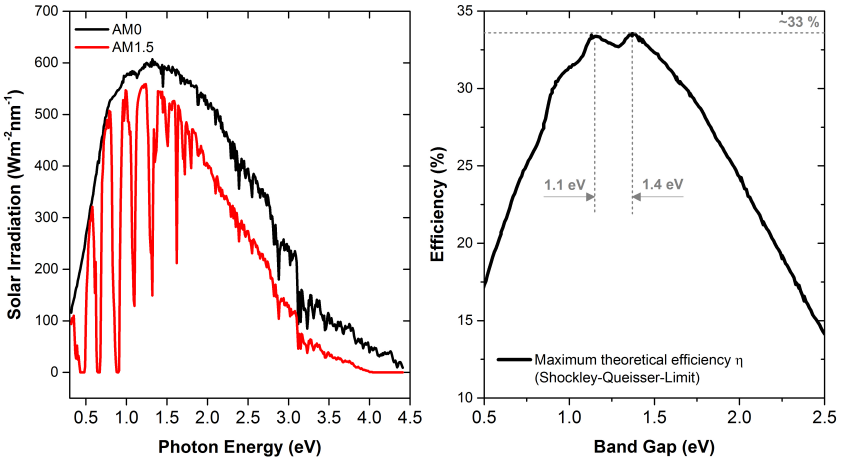

Figure 2.1: *The left panel shows the solar irradiation at mean-earth distance (AM0- extraterrestrial (black)) and under AM1.5 (red) as a function of photon energy (data taken from table in [22]). The right panel shows the maximum theoretical efficiency* η *for a solar cell under AM1.5 illumination. The maxima in energy and efficiency are marked with gray dashed lines. Data taken from [23].*

were taken into account by Shockley and Queisser [24] in their calculation of the maximum theoretical efficiency η of a given solar cell. The theoretical limit, called Shockley-Queisser-Limit, is displayed in the right panel of Figure 2.1. Thus the maximum efficiency of a single junction solar cell is approximately 33% with a band gap of 1.1 to 1.4 eV.

2.1 Chalcopyrite-based Thin Film Solar Cell Devices

Chalcopyrite-based thin film solar cells are made from the $Cu(In_{1-x},Ga_x)(S_ySe_{1-y})_2$ material system (hereafter CIGSSe) and have gained more and more interest due to their high perfomance. In comparison to crystalline silicon-wafer based solar cells chalcopyrite-based absorbers have some advantages. First of all the CIGSSe material features a direct band gap [25] and therefore a higher absorption coefficient. Moreover chalcopyrite-based absorbers have a tunable band gap from $E_g = 1.00$ eV for $CuInSe_2$ [26] to $E_g = 2.43$ eV for $CuGaSe_2$ [26]. This allows to reach best efficiencies according to the Shockley-Queisser-Limit and also allows a band gap grading to be incorporated into the absorber layer.[27] The commonly used device structure is shown in Figure 2.2 where each layer fulfills a different purpose in the solar cell. Usually soda-lime glass (SLG) is used as substrate material followed by a

molybdenum layer as the back contact. However, alternative substrate materials like polyimide [28] or metal foils [29] are also applied as substrate materials. The CIGSSe absorber is covered with a thin buffer layer that is commonly CdS (alternatively ZnO, In_2S_3, In_2Se_3...), and the ZnO window bi-layer that acts as front contact with an undoped (intrinsic) i-ZnO and an aluminum doped n-ZnO layer. The in principle simple preparation of CIGSSe is another advantage. For good reproducibility and deliberate optimization the stability of each material used for the individual layers needs to be guaranteed throughout device deposition and preparation.

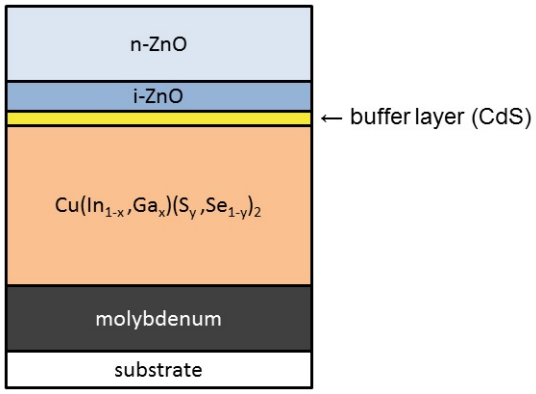

Figure 2.2: *Schematic of a typical CIGSSe solar cell layer stack.*

2.1.1 Material Properties of Cu(In,Ga)Se_2 Absorbers

The most efficient chalcopyrite-based solar cell absorbers have a Cu(In,Ga)Se_2 composition (hereafter CIGSe), i.e., they are sulfur-free (y=1). Besides the already listed advantages of this material system, chalcopyrite-based absorbers exhibit more peculiarities. It is already been long known that the formation of a good interface between buffer and absorber needs an In-rich (Cu-poor) surface.[29] In general, a copper deficient surface region is accompanied by a band gap widening and/or band bending.[30, 31] This results in a conduction type inversion of the p-type absorber at the surface/interface and a minimization of interface recombination.[32, 33]
Moreover sodium-diffusion from the underlying soda-lime glass was found to be crucial for high-efficient CIGSe solar cells.[34–37] Recent record efficiencies were reached using a controlled incorporation of elements, mainly NaF and/or KF, in the absorber via a post-deposition treatment (PDT) (further explanation in 2.1.2).[4, 7] It is already known that a

NaF-PDT can further improve device efficiencies without relying solely on the sodium diffusion from the substrate.[36, 38–40] Recently it has been exhibited that adding potassium even further improves the device perfomance.[4, 7] These treatments, especially providing potassium, can be applied during [41] or after [4, 7, 42–44] the absorber growth.

2.1.2 Deposition Method and Sample Properties

The Cu(In,Ga)Se_2 absorbers used for the studies within this thesis were prepared by the Laboratory for Thin Films and Photovoltaics of the Empa-Swiss Federal Laboratories for Materials and Science Technology (Empa) using a low-temperature multistage process (<500°C). They are grown according to Ref. [28] on commercially available 25 μm thick polyimide (PI) films coated with a 600 nm thick molybdenum back contact. The roughly 2 μm thick CIGSe absorber layers are grown by co-evaporation in a high-vacuum chamber with a base pressure of $\sim 1.0 \cdot 10^{-7}$ mbar equipped with Cu, In, Ga, and Se effusion cells.[28]
The PI films are inherently sodium free, and so an in-situ NaF-PDT was applied for 20 min on some samples after the CIGSe growth according to Ref. [45]. Additionally several samples were treated with a KF-PDT for additional 20 min after the NaF-PDT in the presence of selenium.[4] Two sample series were prepared including an alkali-free (i.e., untreated) CIGSe absorber, a CIGSe absorber only treated with a NaF-PDT, and an absorber with a combined NaF/KF-PDT. The difference between the two series is in the variation of the alkali treatments and PDT rates: an "*alkali-rich*" treatment using an evaporation rate of approximately 1.5-2 nm/min with thicker covering layers on top of the CIGSe absorber and an "*alkali-poor*" (rate=1-1.5 nm/min) treatment resulting in thinner cover layers.

For each studied sample another absorber was simultaniosly prepaired from which solar cell devices were fabricated. For this the CdS layer was grown using a chemical bath deposition [46] followed by radio frequency (RF) sputter deposition of the i-ZnO/ZnO:Al window layer, and evaporation of the grid as electric contacts.[4] For the sample series prepared under alkali-rich post-deposition treatment conditions no anti-reflection coating (MgF_2) was applied and the evaporation of the grid was not deposited directly after sample growth due to failure of the evaporator. This needs to be kept in mind looking at the solar cell results in Table 2.1. For the second sample series (alkali-poor) the complete device was fabricated immedialty after absorber growth.

For better understanding of the impact of the potassium treatment on the CIGSe structure and to check the formation of a possible K-In-Se layer a KF-PDT In_2Se_3 reference sample was prepared by Empa. Soda-lime glass was used as substrate material with a diffusion barrier in this case together with a molybdenum layer. In_2Se_3 was deposited followed by a KF and Se co-evaporation. The porous structure shows a film thickness of roughly 400 nm. Secondary ion mass spectrometry (SIMS) shows the presence of potassium through the entire film with a quasi-constant Se amount and a higher In amount towards the back. Ga and Na impurities are present in the SIMS profile due to a hot Ga source during evaporation and sodium from the K source material.

Table 2.1: *Values for the open-circuit voltage (V_{OC}), the short-circuit current density J_{SC}, the fill factor (FF) and the efficiency η for the studied Cu(In,Ga)Se_2 samples.*

sample	V_{OC} (mV)	J_{SC} (mA/cm^2)	FF (%)	η (%)
alkali-free	579	34.1	67.9	13.4
NaF-PDT (alkali-rich)	645	34.2	69.4	15.3
NaF/KF-PDT (alkali-rich)	652	33.6	75.1	16.5
alkali-free	543	33.0	63.5	11.4
NaF-PDT (alkali-poor)	629	32.6	71.1	14.5
NaF/KF-PDT (alkali-poor)	639	32.3	74.7	15.4

To prevent surface contamination and minimize air exposure, all samples were sealed and packed in a N_2-filled glovebag attached to the deposition chamber at Empa and opened in a N_2-filled glovebox attached to the UHV-system at HZB. To remove the remaining alkali fluoride from the surface of the PDT CIGSe samples the standard protocol developed at Empa was followed: the samples were immersed in aqueous ammonia solution (1 mol/l) for 1-2 min and rinsed/stored in deionized (DI) H_2O until introduced in the load lock chamber of the glovebox where they were vacuum dried. The KF-PDT In_2Se_3 sample was only washed in DI water. Unless specifically mentioned, no further cleaning (by, e.g. Ar+ sputtering) of the sample surface was performed before measurements. All CIGSe samples on PI foil were cut and taped on glass substrates before measurement to ensure a plane in surface.

2.2 Hybrid Organic-Inorganic Perovskite Solar Cells

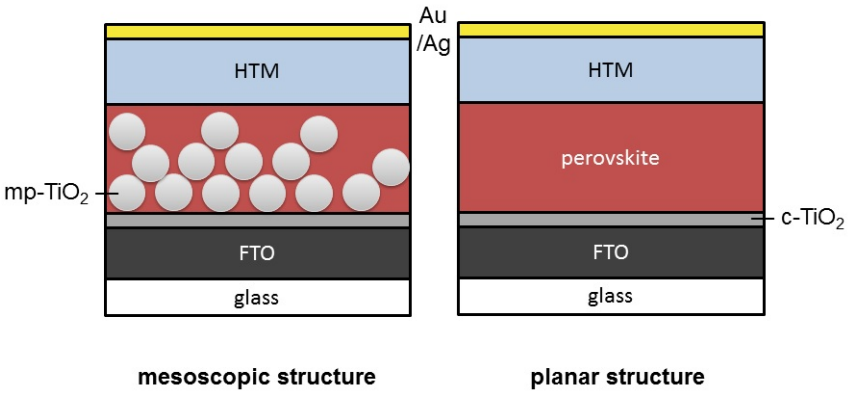

Figure 2.3: *Schematics of two layer stacks for perovskite solar cells. The mesoscopic structure with a mesoporous TiO_2 (mp-TiO_2) scaffold on top of a compact TiO_2 (c-TiO_2) layer on FTO/glass covered with a perovskite layer, a hole-transport material (HTM), and Au/Ag contact. On the other side is the planar structure with a c-TiO_2 on FTO/glass cover with a perovskite layer, HTM, and Au/Ag contact. Adapted from [47].*

Hybrid organic-inorganic perovskite-based solar cells are a relativly new and fast-emerging type of thin film solar cells that have shown a steep efficiency gain in the last few years. This new era goes somewhat back to the so called "Grätzel-cells", i.e., dye-sensitized solar cell first described by Michael Grätzel [48] in 1991. His research has laid the research foundation for solid-state sensitized perovskite solar cells. Initiated with a dye as the absorbing light material/harvester introduced in porous semiconductors for a larger covering area, they were replaced by organic-inorganic perovskite-based materials with the first reported cell in 2009 [8] with an efficiency of 3.8% that has increased to over 21% [49], recently.
The material has an ABX_3 crystal structure with A as the organic part, B the metal, and X the halide part for the use as solar cell material. The most efficient and common type for hybrid organic-inorganic solar cells is $CH_3NH_3MX_3$ with M=Pb or Sn and X=I, Br, Cl (or a mixture thereof), which was first reported in 1978 by Weber [50]. At present, the organic part methylammonium ($CH_3NH_3^+$, MA) is often replaced by formamidinium ($HN{=}CHNH_3^+$, FA) and the inorganic metal part with Sn, Cs, or a mixture of Pb,Sn, and/or Cs.
For these hybrid solar cells no universal layer stack structure has yet been established. However, the most efficient devices consist either of $MAPbX_3$ on top of a thin mesoporous TiO_2 (mp-TiO_2) capped with a solid perovskite layer [9, 10], a solid perovskite layer as absorber

on top of a mesoporous insulating scaffold [11, 12], or a solid perovskite layer on top of a flat/compact TiO_2 (c-TiO_2) [13, 14]. The mesoscopic and the planar structure are sketched in Figure 2.3.
Besides the low material and production cost another advantage is the low process temperature of around 100°C. This is of benefit when applying this material as a top layer in e.g. a tandem solar cell, especially when heat sensitive materials are used in the solar layer stack. Nevertheless, the not yet established working principle of the solar cell, the fast degradation, and the use of heavy metal are major disadvantages.

2.2.1 $CH_3NH_3PbI_{3-x}Cl_x$ Absorbers

One of the most and commonly used methylammonium lead halide perovskites are $CH_3NH_3PbI_3$ and $CH_3NH_3PbI_{(3-x)}Cl_x$. The addition of chlorine results in an improved performance. This type of hybrid perovskite solar cell shows a longer diffusion length [51], a high optical absorption coefficient as well as better charge mobility and lifetime [52] in comparison to Cl-free triiodide perovskites. However, the role and the exact presence and location of Cl in the device remains unclear. One of the crucial points in performance is the strong dependence on the processing parameters.
The addition of chlorine in the precursor solution reduces charge recombination [53] and results in a high open-circuit voltage (V_{OC}) [9]. According to Yu et al., "the function of Cl (or Cl^-) is to facilitate the release of excess $CH_3NH_3^+$ at a relatively low annealing temperature", because a rich $CH_3NH_3^+$ environment negatively affects the crystal formation.[54] After crystal formation the x-ray diffraction (XRD) structure of $CH_3NH_3PbI_{(3-x)}Cl_x$ is identical to the triiodide perovskite $CH_3NH_3PbI_3$ [54] which leads to the conclusion that although a ratio of 3:1 of CH_3NH_3I : $PbCl_2$ is applied for the precursor solution, little to no chlorine is left in the transformed perovskite film.
For methylammonium mixed lead halide perovskites a band gap of approximately 1.5 eV [55, 56] is found, but a tunable band-gap can be achieved by replacing chlorine with bromin and a variation in I:Br ratio. It is also proposed that a p-i-n structure is present in a $CH_3NH_3PbI_{(3-x)}Cl_x$ based device [57, 58], which is very different from the established working principle in dye-sensitized solar cells.

2.2.2 Deposition Methods

There are different approaches to deposit perovskite on various substrates. The widely used methods are either the one-step method [9], the two-step or sequential deposition [59] or evaporation [15]. Although evaporation of CH_3NH_3I and $PbCl_2$ leads to the most uniform films with the best coverage, the solution process methods are the standard techniques.
The absorber / ETM layer stack, $CH_3NH_3PbI_{(3-x)}Cl_x$ / c-TiO_2 and $CH_3NH_3PbI_{(3-x)}Cl_x$ / mp-TiO_2 (see Figure 2.3) used within the studies of this thesis, if not specifically mentioned otherwise, were prepared by the Clarendon Laboratory, Department of Physics, of the University of Oxford (hereafter U Oxford) following the one-step method and are explained below.

2.2.2.1 TiO_2 Substrate

To prepare the compact and mesoporous TiO_2 substrates a commercially available fluorine-doped tin oxide (FTO) coated glass (Pilkington TEC7) 7 Ω/sq was used. The compact TiO_2 was prepared by spin-coating a solution of titanium isopropoxide in ethanol mildly diluted with hydrochloric acid on FTO substrates at 2000 rpm for 60 s. The layers were dried at 150°C and annealed for 45 min at 500°C.
The mesoporous TiO_2 layer was formed by spin-coating diluted in an anhydrous ethanol TiO_2 paste at 2000 rpm and sintered in air for 30 min at 550°C.

2.2.2.2 Precursor Solution and $CH_3NH_3PbI_{(3-x)}Cl_x$ Deposition

The precursor solution was prepared according to Ref. [9, 13]. Methylammonium iodide CH_3NH_3I (MAI) was prepared by reacting a solution of methylamine (CH_3NH_2) 33 wt% in ethanol with hydriodic acid (HI) 57 wt% in water at room temperature. HI, which is stabilized with 1.5% phosphoric acid (H_3PO_4), was added dropwise while stirring. For crystallization of CH_3NH_3I a rotary evaporator was used and during drying at 100°C a white powder was formed.
The $CH_3NH_3PbI_{(3-x)}Cl_x$ precursor solution was formed by dissolving methylammonium iodide (CH_3NH_3I, MAI) and lead (II) chloride ($PbCl_2$) in anhydrous N,N-dimethylformamide (DMF) in a 3:1 molar ratio with a final concentration of 2.64 M MAI and 0.88 M $PbCl_2$. This solution will result in a later film thickness of approximately 300 nm on c-TiO_2 when preparing the absorbers. For thinner film thicknesses the precursor solution was diluted with

DMF for thicknesses of about 60, 30, and 10 nm.

The respective $CH_3NH_3PbI_{(3-x)}Cl_x$ precursor solution, for layer thicknesses of 300, 60, 30, and 10 nm on c-TiO_2, were spin-coated on compact and mesoporous TiO_2 at 2000 rpm for 45 s in a nitrogen filled glovebox. After spin-coating, the respective films dried for 30 min in N_2 environment before annealing at 90°C for 2.5 h in a N_2 atmosphere to complete crystallization and perovskite formation.
For a complete solar cell device a hole transporting material (HTM) like 2,2',7,7'-Tetrakis-[N,N-di(4-methoxyphenyl)amino]-9,9'-spirobifluorene (spiro-MeOTAD) would be spincoated on top of the perovskite layer. The solar cell layer stack is finished by thermally evaporating a gold or silver electrode. However, in our study we look at samples without the HTM.

Due to extreme moisture sensitivity and fast degradation, the samples where stored and transported in a dry nitrogen environment. Sample exposure to ambient air was kept at minimum. No further cleaning or sample preparation was performed before measurements.

3

Characterization Methods and Instrumentation

This chapter focuses on the theoretical descriptions and explanations of the various measurement techniques used within this thesis: XPS, UPS, HAXPES, XAES, IPES, XAS, XES, SEM, and EDX. The data evaluation and analysis methods applied to absorber and interface characterization are described. Last, the laboratory- and synchrotron-based instrumentation and the respective experimental details are explained.

3.1 Direct Photoemission (UPS, XPS, HAXPES)

Photoelectron spectroscopy (PES) is based on the external photoelectric effect first discovered by H. Hertz and W. Hallwachs in 1887/88.[60, 61] The theoretical description of this effect, i.e., releasing an electron, if the sample gets irradiated with light, was successfully done by A. Einstein in 1905.[62]

During the photoemission process an electron gets excited from its ground (initial) state $|\Psi_i>|$ into a final state $|\Psi_f>|$ by a photon with the energy hν. The transition probability $w_{i\to f}$ can be generally described by Fermi's golden rule [63]:

$$w_{i\to f} \propto |<\Psi_f|\widehat{H}|\Psi_i>|^2\ \delta(E_i - E_f - h\nu) \tag{3.1}$$

Here, $\widehat{H}$ is the perturbation operator assigned to the interaction of the system with an electromagnetic field $\widehat{A}$. The δ-function represents the conservation of energy between the initial state E_i and the final state E_f by means of the photon energy hν.
Note, that here a single particle system is described, excluding many-body effects.

In general, to describe the photoemission process equation 3.1 can be simplified using various approximations (more details can be found elsewhere [63–65]) and depicted in terms of the kinetic energy E_K of an electron in its final state outside matter:

$$E_K = h\nu - E_B - \varphi \tag{3.2}$$

with E_B as the binding energy of the electron inside matter, the work function $\varphi = E_{vac} - E_F$ as the difference between the Fermi level E_F and the vacuum level E_{vac}, and hν as the photon energy releasing an electron from solid.

Depending on the photon energy hν, i.e hν>E$_B$+φ, several "types" of electron states can be released, i.e., electrons from core levels, shallow core levels, and valence band, representing the respective occupied states. This is illustrated on the left side for a semiconductor in Figure 3.1. In our case, if x-rays with an energy of about hν=1 keV are used, the technique will be referred to as x-ray photoelectron spectroscopy (XPS) and hard x-ray photoelectron spectroscopy (HAXPES) when hν is between 2-8 keV. If ultraviolet (UV) excitation (e.g. hν=21.22 eV) is used, the technique will be referred to as ultraviolet photoelectron spectroscopy (UPS) to probe the valence band.
In PES the electrons get detected with respect to their kinetic energy and therefore directly related to the materials core and valence levels through the respective binding energy. Hence, PES is used to determine the chemical and electronic properties of the surface and near-surface region.
XPS and HAXPES are applied in complementary fashion to gain a depth-dependent picture

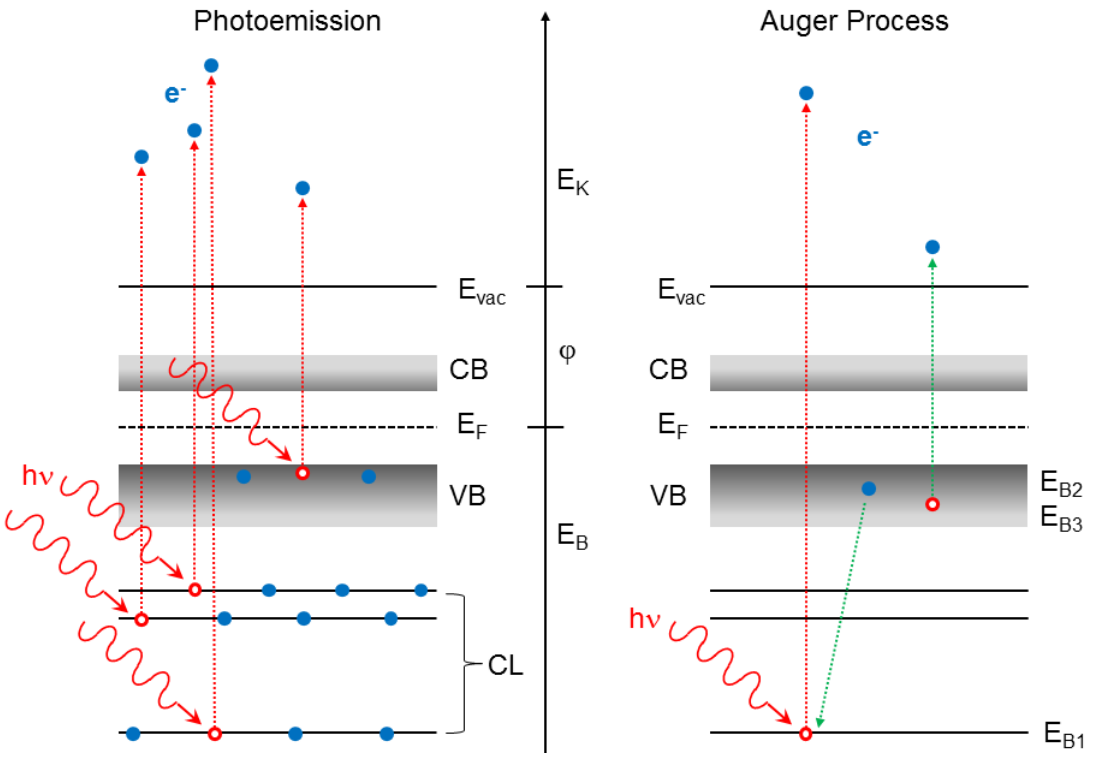

Figure 3.1: *Left: Schematic of the photoemission process in a semiconductor where photons with energies hν excite electrons from core levels (CL) and valence band (VB) states above the vacuum level (E_{vac}). Right: Schematic of the secondary Auger process showing the electronic recombination of the CL hole (green dotted line).*

of the chemical structure varying the excitation energy hν. This enables us to use the intensities of the respective core levels to determine a depth-dependent compositional profile. HAXPES and UPS is used in this thesis to study the valence band (VB) region and in particular to determine the valence band maximum (VBM). The valence band region can be used in a first approximation as the total occupied density of states (TDOS) and determine changes in the electronic structure.

3.2 X-ray Excited Auger Electron Spectroscopy (XAES)

A core hole that is generated by the photoemission process can get filled with an electron from an outer shell, i.e., lower binding energy, by emitting an Auger electron or resulting

in a fluorescence decay (see XES chapter 3.4). The emission of this Auger electron during the Auger process is schematically drawn on the right side in Figure 3.1. The emission of x-rays or Auger electrons are competing processes, however, the Auger decay is more likely depending on the atomic number Z and the core level.[66–68] In our case the generated core hole for the Auger process is excited with x-rays (XAES); electrons can be also used, then this technique is often called AES.
The relaxation of an outer shell electron into the core hole requires an amount of energy equal to $(E_{B1} - E_{B2})$ to be released. This energy excites the Auger electron at E_{B3} above the vacuum level (E_{vac}). This process can be written as:

$$E_K = E_{B1} - E_{B2} - E_{B3} - \Delta_{2,3} - \varphi \tag{3.3}$$

with $\Delta_{2,3}$ as the Coulomb interaction of the involved electronic states. This formulation also shows that the kinetic energy of the Auger electron is independent of the excitation energy and only depends on the binding energy of the involved final state holes.

Auger lines, like XPS and HAXPES, are highly influenced by the chemical surrounding and can be used to identify chemical environment/chemical bonds. Commonly, pairs of photoemission and Auger lines are used to obtain the modified Auger parameter [69]:

$$\alpha' = E_B + E_K \tag{3.4}$$

with E_B as the binding energy of the respective core level and E_K the kinetic energy of the most prominent Auger line of the element of interest. The advantage of the modified Auger parameter is to be independent of sample charging and surface potentials like band bending.[70–72] By pairing a binding energy and kinetic energy, the energy hν cancels out, making α' independet of the excitation energy as well.
The best way to present the modified Auger parameter α' is within a Wagner plot [69, 73], where the derived Auger parameters, indicating the same chemical environment are located along the diagonal lines, i.e., represented by a liner function with a slope of -1, plotting Auger kinetic energy over binding energy.[73] Further information also on the nomenclature can be found for example in [65].

3.3 Inverse Photoemission (IPES)

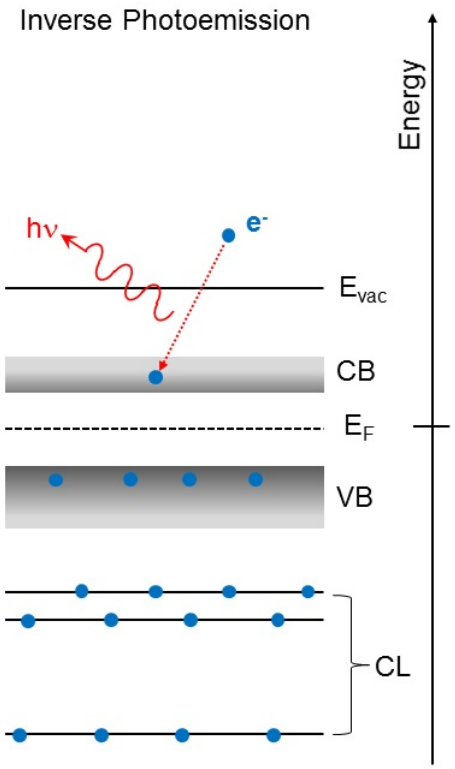

Figure 3.2: *Schematic of the inverse photoemission process in a semiconductor where low-kinetic energy electrons couple into unoccupied states of the conduction band (CB), releasing photons with the energy hν.*

In comparison to the direct photoemission where the occupied states are measured, inverse photoemission (IPES) is used to study the unoccupied states of the conduction band (CB). Here, low-kinetic energy electrons couple into unoccupied states of the CB by releasing photons with the energy hν (see Figure 3.2). The resulting photon can either be detected at constant electron energy, i.e., all possible transitions are detected simultaneously using a spectrometer, or with a bandpass detector, used in our study, at constant detection energy:

$$h\nu = E_K + E_B + \varphi_{e-gun} \tag{3.5}$$

with E_K as the kinetic energy of the incoming electron and φ_{e-gun} as the work function of the electron gun.

The major challenge using IPES is the significantly lower cross-section in the UV-regime in the order of 10^{-5} in comparison to PES [74], resulting in longer measurement times and potential radiation damage. Additional information about IPES can be found for example in [74–76].
In this thesis IPES is used to probe the conduction band states and to determine the conduction band minimum (CBM).

3.4 X-ray Emission and Absorption Spectroscopy (XES, XAS)

As already mentioned in section 3.2 the emission of an Auger electron and fluorescence are two competing processes to fill the generated core hole. The detection of the fluorescence photon over energy is called x-ray emission spectroscopy (XES) and schematically drawn on the right in Figure 3.3. XES can be measured in resonant and non-resonant excitation. However, in the following only the non-resonant excitation process is explained, considering the absorption and emission of the excited and emitted photon as separate processes. In this case Fermi's golden rule (equation 3.1) can be used to describe the transition probability of the two processes in matter. The intensity of photons having energy $h\nu_2$ can then be ascribed by replacing the δ-function with the density of states ρ in equation 3.1, considering also dipole selection rules for initial and final state within ρ:

$$I(h\nu_2) \propto | < \Psi_f | \widehat{H} | \Psi_i > |^2 \, \rho(E_i);\; E_i = E_f + h\nu_2 \tag{3.6}$$

The transition probability for fluorescence is much lower (<1%) than for emitting an Auger electron for low atomic numbers (Z<30). Therefore to generate enough fluorescence photons to measure the x-ray emission process, high excitation intensities are needed, which can be provided by synchrotron facilities.

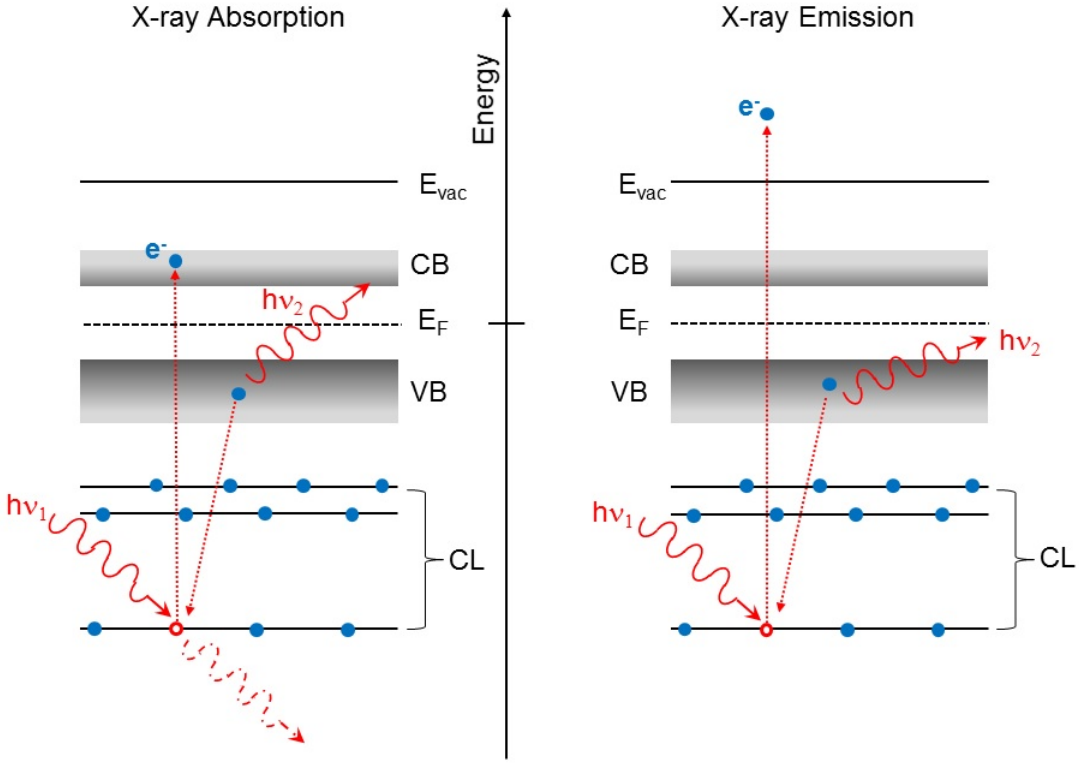

Figure 3.3: *Left: Schematic of x-ray absorption, photon with the energy $h\nu_1$ excites an electron into an unoccupied state of the conduction band (CB), resulting in this case in the fluorescence decay $h\nu_2$ as the secondary process. Right: x-ray emission, photon with the energy $h\nu_1$ excites an electron above the vacuum level E_{vac}; photo-generated hole gets filled with an electron of lower binding energy emitting a photon of $h\nu_2$.*

XES is used to probe the local occupied density of states (LDOS) in the vicinity of the excited core hole and hence characteristically for each element. This enables us to monitor the specific chemical environment of the selected material and element. XES is also insensitive to sample charging.

X-ray absorption spectroscopy (XAS) can be used to study the unoccupied states, by varying the photon energy $h\nu_1$ to excite a core electron into an unoccupied state in the conduction band. The absorption probability can be ascribe by following equation equal to 3.6

$$A(h\nu_2) \propto |<\Psi_f|\widehat{H}|\Psi_i>|^2 \, \rho(E_i);\; E_i = E_f + h\nu_2 \tag{3.7}$$

also considering the respective dipole selection rules and the overlap of the wave functions between initial and final state. The absorption process gets detected using secondary processes like Auger electrons, secondary electrons or fluorescence. The emission of a fluorescence photon of the energy $h\nu_2$ (fluorescence yield (FY)) is displayed on the left in Figure 3.3. In this thesis, XAS data are only shown in total fluorescence yield (TFY).

3.5 Scanning Electron Microscopy (SEM) and Energy Dispersive X-ray Spectroscopy (EDX)

Scanning electron microscopy (SEM) and energy dispersive x-ray spectroscopy (EDX) are both spatially resolved measurement techniques.
SEM is used to image the surface morphology of different materials with high resolution using electrons to irradiate the sample. The accelerated electron beam penetrates the sample interacting elastically and inelastically with matter releasing various types of radiation, i.e., secondary electrons (SE), backscattered electrons (BSE), x-rays, and sometime cathodoluminesence.[77] This interaction, i.e., SE and BSE, and the penetration depth of the electrons are characteristic for the determination of the SEM image, measuring the result of those interactions.

EDX, usually combined in the same set-up as SEM uses the fluorescence photons to study the local chemical compositions.[77] The x-rays are element-specific. Their energy is equal to the difference between the generate core hole and the lower bound electron of the secondary process, comparable to XES (see section 3.4) and XAES (see section 3.2) using electrons instead of photons to excite the sample.

For SEM and EDX electrons with an energy of a few keV are used containing the risk of beam exposure-induced artifacts due to altering the material properties. This is in particular important for the inorganic-organic perovskite materials. Here, beam induced artifacts can be avoided by constantly changing the sample spot.

3.6 Data Evaluation of Absorber and Interface Structures

3.6.1 Inelastic Mean Free Path and Attenuation Length

For most surface-sensitive spectroscopy techniques electrons are used. Their dependence in penetration depth on the kinetic energy (E_K) is illustrated in Figure 3.4.

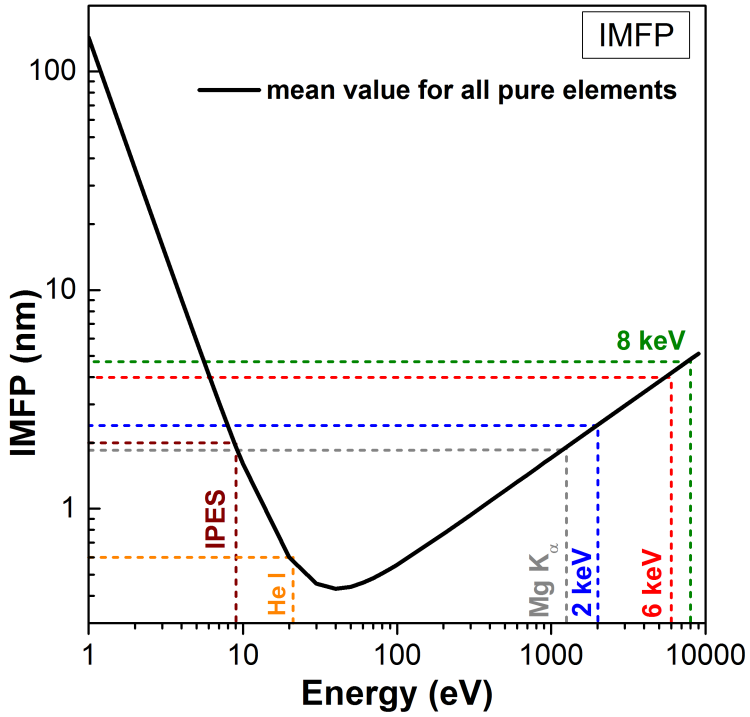

Figure 3.4: *Inelastic mean free path (IMFP) of electrons in pure elemental materials over their kinetic energy as the "universal curve" according to Seah and Dench [78]. Lines mark the used energies for this thesis.*

The trend shown in Figure 3.4 for pure elements is called "universal curve" and shows the behavior of in that case pure elements with respect to their inelastic mean free path (IMFP) over the kinetic energy. This curve exhibits a minimum at around 40 eV with an IMFP lower than 0.5 nm. Electrons with a kinetic energy <40 eV are mainly elastically scattered, whereas for energies >40 eV electrons get inelastically scattered due to interactions with other electrons.
The universal curve displays the electron reactions, where an electron only travels once through matter. This is the case in PES, since a photon excites the electron.

Further, by varying the excitation energy hν and therefore the kinetic energy this results in differences in IMFP, as shown in Figure 3.4. The colored lines mark the maximum IMFP that can be gained by the applied excitation energies used within this thesis.
To get material specific values the respective IMFP was calculated using the QUASES IMFP TPP2M code.[79] This code only calculates reliable values for kinetic energies above 100 eV. Hence, for IPES and UPS the IMFP was taken from the universal curve by Seah and Dench [78].

The intensity from a certain information depth I(d) for PES and XAES is limited by the IMFP of the respective photoelectron attenuating from the distance d and the attenuation due to inelastic scattering under normal emission:

$$I(d) = I_0 e^{-\frac{d}{IMFP}} \tag{3.8}$$

The actual probing depth, where 95% of the signal originates is 3·IMFP, however more than 60% of the signal comes from within less than a distance of one IMFP from the surface.
Although the largest contribution to any photoemission signal always comes from the sample surface, increasing excitation energies, and thus increasing IMFP, shifts the distribution of signal according to equation 3.9, increasing the relative contributions of near-surface bulk states to the measurement.[80]

For spectroscopy techniques using photons, e.g. XES and XAS, the limiting factor for the probing depth is the attenuation length of the respective photon and therefore the transmission of the photon through matter. For calculating the effective attenuation length d_{att} both the exciting and the emitted photons have to be considered with an attenuation length of d_{exc} and d_{em}, respectively and combined in equation [81]:

$$d_{att} = \frac{d_{ex} \cdot sin\alpha \cdot d_{em} \cdot sin\beta}{d_{ex} \cdot sin\alpha + d_{em} \cdot sin\beta} \tag{3.9}$$

with α and β as the angles between the sample surface and exciting and emitted photon.
This attenuation length d_{att} can be used in equation 3.8 instead of the IMFP to calculate the

probing depth for photon transmission.

The material and energy-dependent photon attenuation length d_{ex} and d_{em} are obtained from Henke et al.[82, 83]

3.6.2 Photoionization Cross-section

Using photoemission-based characterization methods the angular distribution of photoelectrons within the electric dipole approximation has to be considered.[84–86] For each core level at each excitation energy the photoionization cross-section is distinct and has to be taken into account.

Figures 3.5 and 3.6 show the energy dependence of the photoionization cross-sections of the shallow core levels for the collected XPS/HAXPES Cu(In,Ga)Se_2 data, namely Cu $3p_{3/2}$, In $4d_{5/2}$, Ga $3d_{5/2}$, Se $3d_{5/2}$, K 3s, and Na 2s.[84, 86] Asymmetry parameters are used to correct the cross-sections for the experimental geometry of the HiKE, BL47XU, and BL15XU endstations (i.e., horizontally-polarized x-rays, with the direction of polarization normal (gracing incidence) to the emission from the sample) as well as the geometry for the laboratory set-up (magic angle). Panel 3.5a shows the photoionization cross-sections in kbarns calculated for polarized hν in the endstation geometry. Figure 3.5b shows the photoionization cross-sections in kbarns calculated for unpolarized hν and the laboratory geometry. Figure 3.6 displays the cross-sections used for quantifying the intensity of the shallow core levels as a function of the inelastic mean free path (IMFP) of the respective excitation energy. For accurate and material specific values for the IMFP for 1253.56 eV (Mg K_α), 2 keV, 6 keV, and 8 keV we used the TPP2M code [79] resulting in approximately 3, 4, 10, and 12 nm, respectively.

For the 2 keV HAXPES data for $CH_3NH_3PbI_{(3-x)}Cl_x$ on TiO_2 the respective photoionization cross-sections for Pb $4f_{7/2}$, I $3d_{5/2}$, Ti $2p_{3/2}$, Cl $2p_{3/2}$, and I 4s can be directly calculated from Ref. [84, 85].

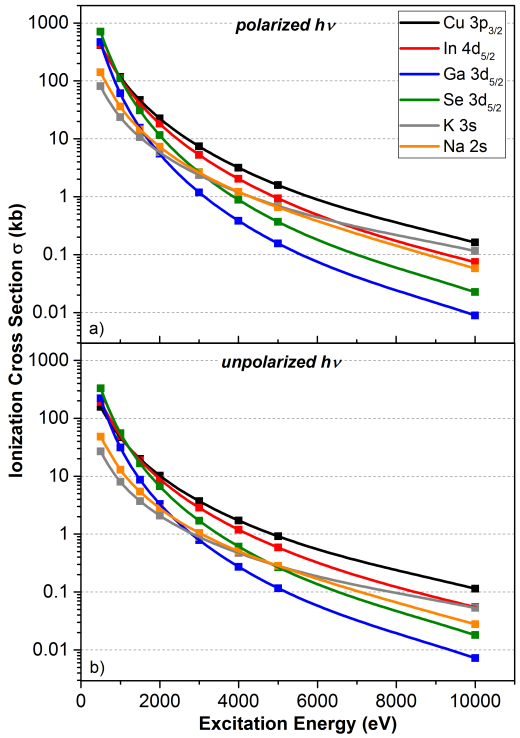

Figure 3.5: *Excitation energy dependent photoionization cross-section of selected shallow core levels. a) Cross-sections corrected for the experimental geometry of the HAXPES setups for polarized photons. b) The cross-sections for the laboratory setup for unpolarized photons.*

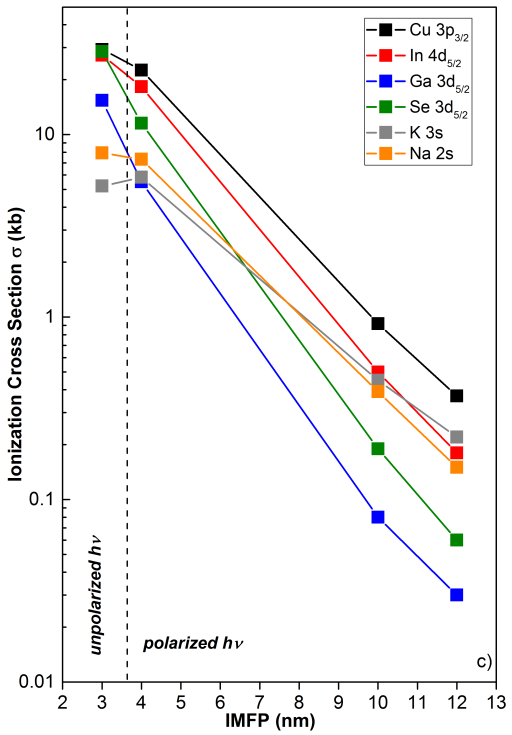

Figure 3.6: The cross-sections of the shallow core levels used for the quantification of the data collected with the respective excitation energy converted to IMFP according to Ref. [79]

3.6.3 Determination of the Valence Band Maximum, Conduction Band Minimum

For determining the valence band maximum (VBM) and conduction band minimum (CBM) measured with UPS, HAXPES, and IPES, respectively, extrapolation of the leading edge is used according to Ref. [87–89].
Several effects can have an impact on the derived VBM values. There is the change in photoionization cross-section (see also section 3.6.2) and, for low excitation energies (i.e., He I), also k-selective effects have to be considered.[88, 89] The band dispersion can lead to a shift in the measured valence state positions. If the shifts and intensity changes significantly affect the states of the uppermost valence band, this can lead to further uncertainty in the

determination of the VBM. These effects, particularly the intensity changes related to photoionization cross-section, are minimized by the linear approximation method. [80]

For deriving the electronic surface band gap E_g^{surf} the CBM value determined with IPES is used together with the VBM value of the 2 keV HAXPES measurement. This approach is used due to the more similar IMFP values (see Figure 3.4) of those two excitation energies compared to the commonly used UPS/IPES method.

3.6.4 Interface Induced Band Bending and Band Offsets

The derived positions of the VBM and CBM can be used to estimate band offsets of the valence and conduction band to characterize the behavior at the interface. Hence, this position can be influenced by interface and surface properties between the substrate (S) and the cover layer (Cl) and affect the band bending, hereafter referred to as interface induced band bending (IIBB).[90] To determine such effects at the interface the changes in core levels due to depositions of a cover layer need to be monitored with increasing thickness. For calculating the IIBB a bare sample (0 nm), i.e., no covering layer, one with a thick cover layer with no substrate signals (y nm), and an intermediate cover layer thickness (x nm) including signals from the substrate and the cover layer need to be measured using the respective core level positions, resulting in an IIBB value:

$$IIBB = -(E_S(0\ nm) - E_S(x\ nm)) + (-E_{Cl}(x\ nm) + E_{Cl}(y\ nm)) \tag{3.10}$$

This value together with the derived position of the VBM and CBM can be used to calculate the valence band offset (VBO) and conduction band offset (CBO)

$$VBO = VBM_S - VBM_{Cl} + IIBB \tag{3.11}$$

$$CBO = CBM_S - CBM_{Cl} + IIBB \tag{3.12}$$

Positive values for the conduction band offset result in a so-called spike, negative CBO values describe a cliff, and a vanishing CBO reveals a flat band alignment as illustrated in

Figure 3.7. Depending on the band offset, this can have positive or negative effects on the solar cell performance and are discussed where appropriate.

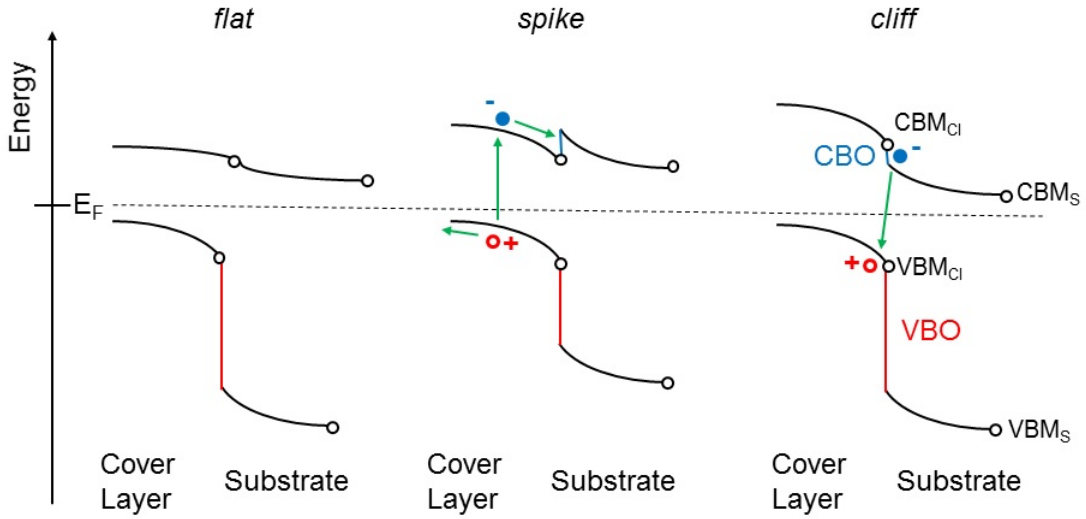

Figure 3.7: *Schematics of band offset and alignment occurring in thin film solar cells.*

3.7 Instrumentation/Experimental Details

3.7.1 Laboratory-based Techniques

For this thesis all laboratory-based XPS measurements were conducted using non-monochromatized Mg K_α (1253.56 eV) and Al K_α (1486.58 eV) radiation and a SPECS PHOIBOS 150 MCD-9 electron energy analyzer positioned in the "magic angle" with a base pressure of the analysis chamber of $< 3 \cdot 10^{-10}$ mbar. The electron energy analyzer was calibrated according to D. Briggs et al.[91] For the collection of the (shallow) core levels and Auger lines, the pass energy of the electron analyzer was set to 30 eV resulting in a combined experimental resolution of approximately 1 eV. For survey spectra the pass energy was set to 50 eV.

UPS measurements were conducted using non-monochromatized He I (21.22 eV) radiation source. For the collection of the UPS valence band spectra a pass energy of 1 eV was used, resulting in a combined energy resolution of $<$100 meV.

IPES measurements were conducted using a commercial PSP Vacuum Technology setup

consisting of a low-energy electron gun and a solid-state photon detector. The electron gun used a cathode with a BaO dispenser resulting in a sample current of 5-10 μA. The detector consists of a photon energy bandpass filter (i.e., fluoride window in combination with a NaCl coated Ta cone) and an electron multiplier. The energy resolution was approximately 1 eV. The base pressure in the IPES chamber was $< 5 \cdot 10^{-9}$ mbar.
For a common UPS and IPES energy scale, the Fermi level (E_F) of a gold foil was measured using both techniques.

SEM of Cu(In,Ga)Se_2 (see chapter 4.1.1) was performed at Empa by Patrick Reinhard using a Hitachi S-4800 with an in-lens detector. An acceleration voltage of 5 kV, a working distance of 5 mm and a magnification of 60000 were used for the measurements.

SEM of $CH_3NH_3PbI_{(3-x)}Cl_x$ (see chapter 5.2.1.2) was performed in-house using a commercially available Zeiss UltraPlus scanning electron microscope at a working distance of 47.8 mm and an acceleration voltage of 5 kV for the primary electron beam.
EDX was performed at the same microscope using an Oxford Instruments X-Max 80 X-ray detector and the AZtec acquisition and evaluation software. The beam energy and current were 7 keV and about 1 nA, respectively. This set-up was used to study $CH_3NH_3PbI_{(3-x)}Cl_x$ layers on compact and mesoporous TiO_2.

3.7.2 Synchrotron-based Techniques

3.7.2.1 Synchrotron radiation

Most of the experiments done within this thesis were conducted at three different synchrotron light sources: Berliner Elektronen Synchrotron (BESSY II) in Berlin, Advanced Light Source (ALS) in Berkeley, and Super Photon Ring - 8 GeV (SPring-8) in Hyõgo.
Synchrotrons are large scale facilities functioning as an energy-tunable source using the principle of relativistic electromagnetism to gain synchrotron radiation. Here, a charged particle is moving at relativistic energies, i.e., near the speed of light, in a curved trajectory, the so called storage ring. Before, those particles are generated as a beam in a linear accelerator, accelerated in a booster ring and then inserted into the storage ring. The curved trajectory of the charged particles is caused by bending magnets along the storage ring and insertion devices placed in the straight section of the storage ring. To compensate the energy losses

due to bending magnets and insertion devices, klystrons are used.
The following brief description is based on Ref. [92], which can be used for a more detailed explanation:

In general, an accelerated particle emits electromagnetic waves. A particle that is constrained to a circular trajectory is subjected to a centripetal force and therefore is accelerated leading to radiation. In the case of synchrotron radiation, with particle having a velocity v close to the speed of light c, the Lorentz factor γ describes the shape and direction of the radiation [92]:

$$\gamma \equiv \frac{1}{\sqrt{1-\frac{v^2}{c^2}}} \tag{3.13}$$

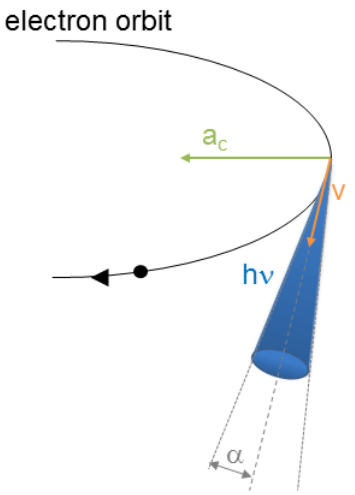

Figure 3.8: *Scheme of the radiation emission of an electron traveling through a constant magnetic field with the relativistic velocity v being accelerated towards the center with a_c, emitting radiation in a cone with an angle α. Adapted from Ref. [92].*

Figure 3.8 shows schematically the emission collimated along the tangential direction with an angle $\alpha \cong \frac{1}{2\gamma}$ of a charged particle at relativistic speed traveling through a constant magnetic field.[92]
The spectrum of the emitted radiation covers the entire electromagnetic spectrum and the energy can be expressed as the critical energy E_C [92]:

$$E_C = \frac{3ehB\gamma^2}{4\pi m} \tag{3.14}$$

with the charge e, the mass m, the Plank constant h, and the magnetic flux B of the bending magnetic. E_C is the energy that divides the radiation emission into two equal parts of the intensity.

Equation 3.14 can be rewritten for synchrotron radiation using electrons with the energy E_r and $\gamma = \frac{E_r}{mc^2}$ to [92]:

$$E_C\ [keV] = 0.655 E_r^2\ [GeV]\ \cdot\ B\ [T] \tag{3.15}$$

This energy has a peculiar spectrum depending on the particle trajectory influenced by the magnetic field of the emitting devices which can be divided into bending magnets, wigglers, and undulators. Bending magnets are simple dipole magnets, generating a uniform magnetic field perpendicular to the electron orbit. Wigglers are high field superconducting magnet arrays causing the electron to oscillate with large deviation angles around the ideal trajectory compared to undulators using lower field arrays of magnets. Here the electrons slightly oscillate around the ideal trajectory.[92] The basic principle of such insertion devices is schematically shown in Figure 3.9.

They consist of stacked permanent magnet arrays with alternating polarity with a distance of λ_U as the undulator frequency. The magnetic field B_0 causes the electrons traveling through to oscillate, emitting radiation. Under certain conditions the emission cones can overlap resulting in constructive interference and therefore an increase in intensity at specific photon energies.[92] These conditions can be described with the non-dimensional magnetic strength K defined as [92]:

$$K \equiv \frac{eB_0\lambda_U}{2\pi mc} = 0.9337 \cdot B_0\ [T]\ \lambda_U\ [cm] \tag{3.16}$$

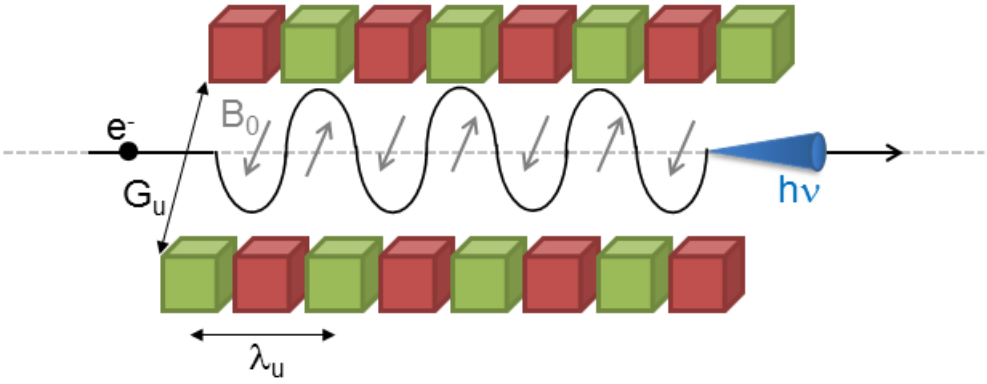

Figure 3.9: *Schematic of insertion device with alternating polarity of permanent magnets with a magnetic field density of B_0. The path of the electron (black) and the resulting synchrotron radiation (blue) is indicated. G_U represents the undulator gap, i.e., the distance between the magnetic arrays and λ_U as the undulator frequency, i.e., the distance between equally poled magnets.*

For K$\gg$1 the insertion device is a wiggler, resulting in similar emission as bending magnets. K=1 or smaller is characteristic for an undulator resulting in constructive interference of the emission cones raising the photon intensity at a wavelength λ. Changes in B_0 caused by a change of the undulator gap G_U results in changes of the photon energy.[92]

After synchrotron radiation is produced using bending magnets and insertion devices, this radiation is led through beamlines to the endstation where the experiments are conducted.

3.7.2.2 Instrumentation and Experimental Details

BESSY II

BESSY II has a specific ring energy E_r of 1.7 GeV and a critical energy E_C of 1.9 keV and is therefore most intense in the soft x-ray regime.
The HAXPES measurements were performed with an excitation energy of hν=2 keV at the HiKE endstation [93] of the KMC-1 beamline [94]. The base pressure at HiKE was $< 1 \cdot 10^{-8}$ mbar and it is equipped with a Scienta R4000 hemispherical electron energy analyzer positioned almost normal to the sample surface. The KMC-1 beamline uses a bending magnet and a double crystal monochromator (DCM), allowing to tune the excitation energy

between 2.0-10.0 keV. A pass energy of 200 eV was used for all detail spectra and 500 eV for all survey spectra, respectively. The excitation energy was calibrated by measuring multiple Au Fermi edges and 4f spectra of a grounded clean Au foil and setting the Au $4f_{7/2}$ binding energy equal to 84.00 eV. Spectra were recorded using photon energies of 2 keV using the Si(111) DCM crystal. For detail spectra the combined analyzer plus beamline resolution is approximately 0.25 eV.

SPring-8

The ring energy E_r of SPring-8 is 8 GeV resulting in a critical energy of E_C=42.6 keV and therefore suitable in the hard x-ray regime.
HAXPES experiments with an excitation energy of 6 keV were performed at the BL15XU beamline [95, 96]. Beamline BL47XU [97] was used for experiments with an excitation energy of 8 keV. The base pressure at BL47XU endstations was $< 1 \cdot 10^{-8}$ mbar and better than $< 1 \cdot 10^{-7}$ mbar at BL15XU. Each endstation is equipped with a Scienta R4000 hemispherical electron energy analyzer with similar geometrical setups for beamline and analyzer, as for the measurements at HiKE. Both beamlines uses undulators and are equipped with double crystal monochromators (DCMs), allowing to tune the excitation energy between 4.0-36.0 keV at BL15XU, and between 5.2-37.7 keV at BL47XU. Pass energy and energy calibration were the same as for the measurements at HiKE, using the 1^{st}, 3^{rd}, and 4^{th} reflection order of the Si(111) DCM crystal resulting in a combined analyzer plus beamline resolution of approximately 0.25 eV.

Using undulators as insertion devices instead of bending magnets and the much higher ring energy results in higher photon intensities and energies. The higher flux at beamline BL15XU and BL47XU compared to the KMC-1 yields in a higher count rate reducing the measurement time significantly, especially for the valence band region due to the decrease in photoionization cross-sections for higher excitation energies (see section 3.6.2).

ALS

The ALS has a specific ring energy E_r of 1.9 GeV and a critical energy E_C of 2.4 keV and also most intense in the soft x-ray regime.

XES and XAS were performed in the soft x-ray fluorescence SXF endstation [98] of beamline 8.0.1 using an undulator. Photon energies of 120 eV and a range of 280-306 eV were used for selenium $M_{4,5}$ XES and carbon K / potassium $L_{2,3}$ XAS measurements, respectively. The XES energy scale was calibrated using elastically scattered photons in the range of 100-120 eV in 2^{nd} diffraction order. XAS spectra were recorded in the total fluorescence yield mode using a channeltron detector. To account for the strong background that arises from the proximity of the K $L_{2,3}$ edge to nearby C K edge, the absorption spectrum of HOPG (highly-oriented pyrolytic graphite) was measured; this measurement was also used for energy calibration.

4

Impact of NaF/KF Post-depostition Treatments on the Chemical and Electronic Structure of $Cu(In,Ga)Se_2$ Thin Film Solar Cell Absorbers

Much of the content in this chapter has been published in:

1. E. Handick, P. Reinhard, J.-H. Alsmeier, L. Köhler, F. Pianezzi, S. Krause, M. Gorgoi, E. Ikenaga, N. Koch, R. G.Wilks, S. Buecheler, A. N. Tiwari, and M. Bär, "Potassium postdeposition treatment-induced band gap widening at $Cu(In,Ga)Se_2$ surfaces – reason for performance leap?", ACS Applied Materials & Interfaces **7**, 27414–27420 (2015). (Ref. [80])

2. E. Handick, P. Reinhard, R. G. Wilks, F. Pianezzi, R. Félix, M. Gorgoi, T. Kunze, S. Buecheler, A. N. Tiwari, and M. Bär, "NaF/KF Post-Deposition Treatments and their Influence on the Structure of $Cu(In,Ga)Se_2$ Absorber Surfaces", Proceedings of the *43rd* IEEE Photovoltaic Specialist Conference (PVSC), 0017-0021 (2016). (Ref. [99])

3. E. Handick, P. Reinhard, R. G. Wilks, F. Pianezzi, T. Kunze, D. Kreikemeyer-Lorenzo, L. Weinhardt, M. Blum, W. Yang, M. Gorgoi, E. Ikenaga, D. Gerlach, S. Ueda, Y. Yamashita, T. Chikyow, C. Heske, S. Buecheler, A. N. Tiwari, and M. Bär, "Formation of a K-In-Se surface species by NaF/KF post-deposition treatment of Cu(In,Ga)Se_2 thin-film solar cell absorbers" ACS Applied Materials & Interfaces **9**, 3581-3589 (2017). (Ref. [100])

In this chapter the properties of chalcopyrite-based thin film solar cell absorbers, in this case Cu(In,Ga)Se_2 (CIGSe), will be discussed. In the last years, alkali treatments of CIGSe absorber surfaces have gained more and more interest due to the beneficial impact on the device performance, but the influence on topography, the chemical, and electronic structure is not yet determined. For a solar cell device one of the most crucial interfaces is formed between the surface of the absorber and the adjacent emitter there in particular the chemical and electronic properties are of interest.
First, the effect of alkali post-deposition treatment on the topography of those absorbers will be elucidated. Second, the impact of such alkali treatments on the chemical structure will be discussed. In particular the influence of potassium on the chemical surface structure is derived, suggesting a possible bilayer structure. Finally, the effect on the electronic structure most significantly a surface band gap widening for alkali-rich surfaces, is shown.

4.1 Impact of Alkali Treatments on Topography and the Chemical Structure of CIGSe Absorbers

4.1.1 Topography study by SEM

Scanning electron microscope (SEM) measurements (conducted by Empa) show the topography of the investigated samples and the impact of different alkali post-deposition treatments (alkali-rich and alkali-poor) as introduced in chapter 2.1.2. Prior to imaging, all alkali treated samples underwent a rinsing procedure as explained in 2.1.2.
Figure 4.1 allows comparing SEM top-view images of the alkali-rich (left column) and alkali-poor (right column) CIGSe absorbers as well as alkali-free (a, d), NaF-PDT (b, e), and NaF/KF-PDT (c, f) samples. Both alkali-free absorbers displayed in a) and d) show the well-known facet-like CIGSe topography. This is also the case for the NaF-PDT CIGSe absorbers subjected to an alkali-rich (b) and alkali-poor treatment (e). However, for the

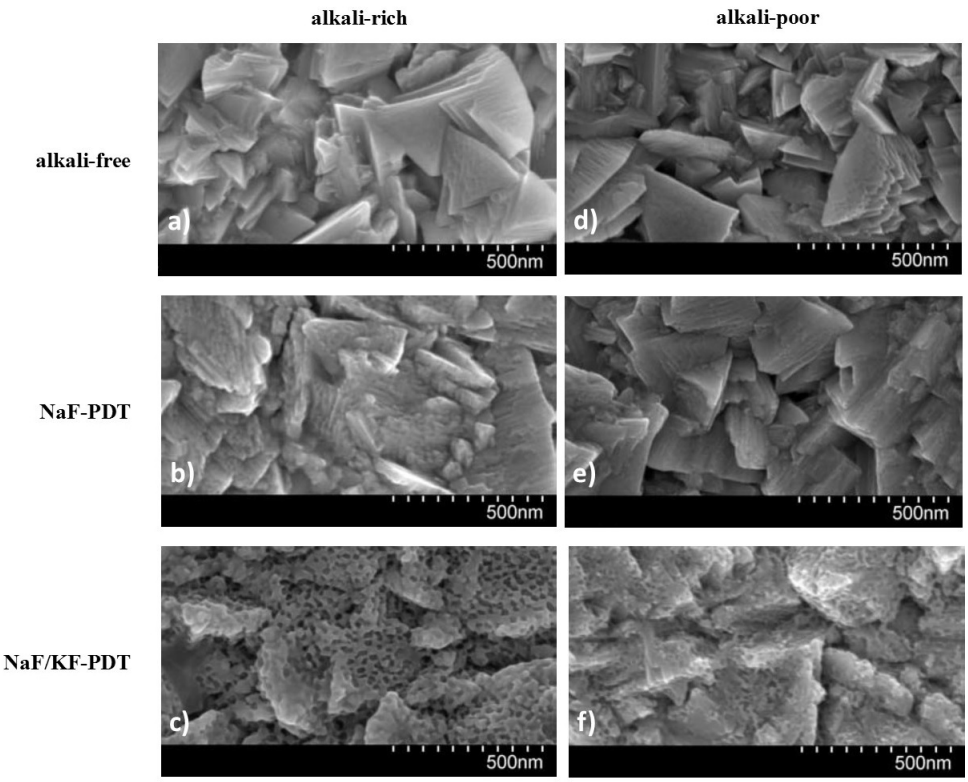

Figure 4.1: *SEM top-view image of alkali-rich CIGSe absorbers (left column) and alkali-poor CIGSe absorbers (right column) with an untreated (i.e., alkali-free) CIGSe (a, c) and subjected to NaF-PDT (b, d), and NaF/KF-PDT (c, f). Adapted from [99].*

alkali-rich NaF-PDT CIGSe the facet-like structure appears to be smoother which might be a result of the stronger degree of NaF-PDT. The most prominent impact of alkali treatments on the topography is apparent for the NaF/KF-PDT CIGSe samples (4.1c, f) confirming the formation of a nanopatterned surface structure after applying an additional KF- treatment as was previously reported by Empa [101]. This nanopatterned surface structure is more pronounced, i.e., a presumably thicker surface layer with more distinct features is formed for the alkali-rich NaF/KF-PDT, almost covering the well-known CIGSe structure (see also Figure 4.1a). The SEM image of the alkali-poor NaF/KF-PDT CIGSe (Figure 4.1f) also seems to show this nanopatterning but significantly less pronounced so that the facet-like CIGSe topography is still dominating. These findings of the topography suggest that a higher degree of surface nanopatterning results from the alkali-rich NaF/KF-PDT in comparison to the respective alkali-poor PDT. Thus, just by varying the PDT parameters the topography of the absorbers can deliberately be "tuned".

For the samples studied here the alkali-rich NaF/KF-PDT CIGSe is most similar to the material that is described in Ref. [101] to achieve the highest efficiency. Nevertheless, the alkali-poor NaF/KF-PDT CIGSe can to some extend also be related to the findings in Ref. [101] with an increase in hole size and a wider distribution over the sample leads to a reduction in efficiency mainly due to some losses in FF and V_{OC} (see also Table 2.1).
Note, that other high-efficiency CIGSe solar cell devices prepared by other groups, e.g. at Zentrum für Sonnenenergie- und Wasserstoff-Forschung Baden-Württemberg (ZSW), never shown this kind of surface patterning but reached (even higher) efficiencies. Therefore comparing the alkali-rich absorber with a more pronounced nanopatterning to the alkali-poor absorber is of importance.

For further evaluation of these samples the differences in nanopatterning, i.e., possibly a noncontinuous surface layer which might result in different optoelectronic properties, have to be taken into account evaluating the impact of these alkali treatments. As becomes already apparent from the SEM study the nanopatterning surface for the NaF/KF-PDT CIGSe absorbers also exhibit variations in domain size and also variations in the thickness of the formed surface region, already suggesting an explanation for the difference in device performance displayed in Table 2.1. For such nanostructured surfaces it has already been suggested that they can act as passivation layers [80] (see also chapter 4.2) and that point openings can be present in the surface layer [101]. Thus, the formation of point contacts seems possible due to NaF/KF-PDT that could also beneficially impact open circuit voltage and fill factor as proposed in [101]. Furthermore it would be consistent with our dataset for device performance, showing an increase in V_{OC} and fill factor for the alkali-rich NaF/KF-PDT CIGSe (see Table 2.1).

4.1.2 Depth-resolved XPS/HAXPES Measurements

This subchapter compares the "depth-dependent" compositions of the differently treated CIGSe absorbers with alkali-rich and alkali-poor PDTs. Here, the main question is how the PDT influences the chemical structure of the Cu(In,Ga)Se_2 absorber. To characterize the samples we use photoelectron spectroscopy with different excitation energies (1253.56 eV, 1486.58 eV, 2 keV, 6 keV, and 8 keV) resulting in a variation in inelastic mean free path (IMFP) of the photoele ctrons of maximum 2.7, 3.1, 4.0, 9.7, and 12.3 nm [79].

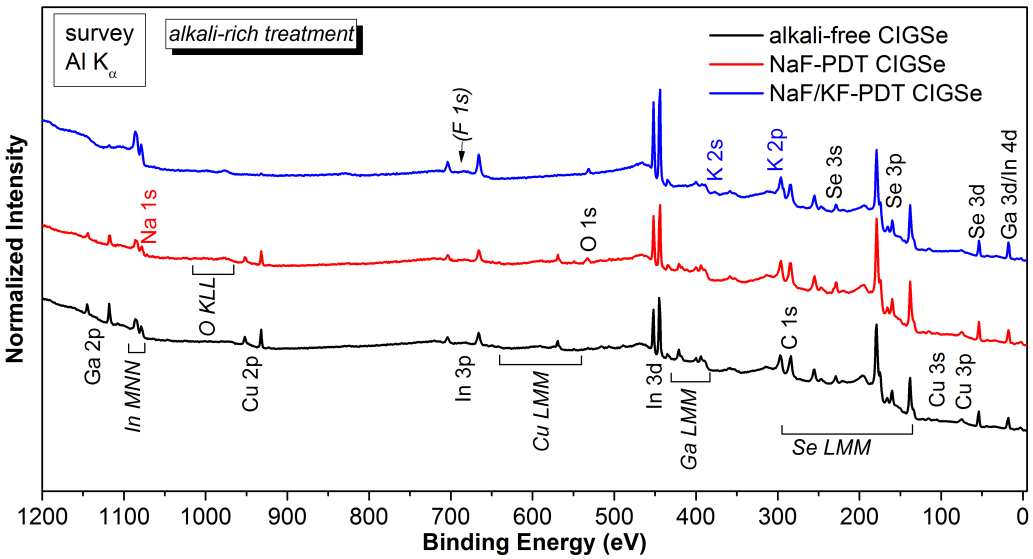

Figure 4.2: *Survey spectra of an alkali-free (black), a NaF-PDT (red), and a NaF/KF-PDT (blue) CIGSe absorber measured with an excitation energy of $h\nu$=1486.58 eV (Al K_α). The post-deposition treated absorbers obtained an alkali-rich treatment. The respective core level and Auger lines are marked. Vertical offset added for clarity.*

The most common method to study the depth profile of materials and layer structures but also most prone to artifacts in particular of thin film solar cell absorbers is secondary ion mass spectroscopy (SIMS), which uses high energy ions to destructively sputter through the sample. Our approach uses non-destructive XPS/HAXPES measurements where depth-sensitivity is reach just with a variation in IMFP from approximately 2.7 to 12.3 nm [79]. Using the shallow core levels (Cu 3p, Se 3d, K 3s, and Ga 3d/In 4d/K 3p) the composition of the surface and the near-surface region can be derived neglecting electron analyzer transmission and IMFP effects. By using synchrotron-based photoelectron spectroscopy with better resolution than laboratory-based XPS in particular the separation of the different contributions in the region where Ga 3d, In 4d, and K 3p unambiguosly be possible, different species can be detected and assigned.

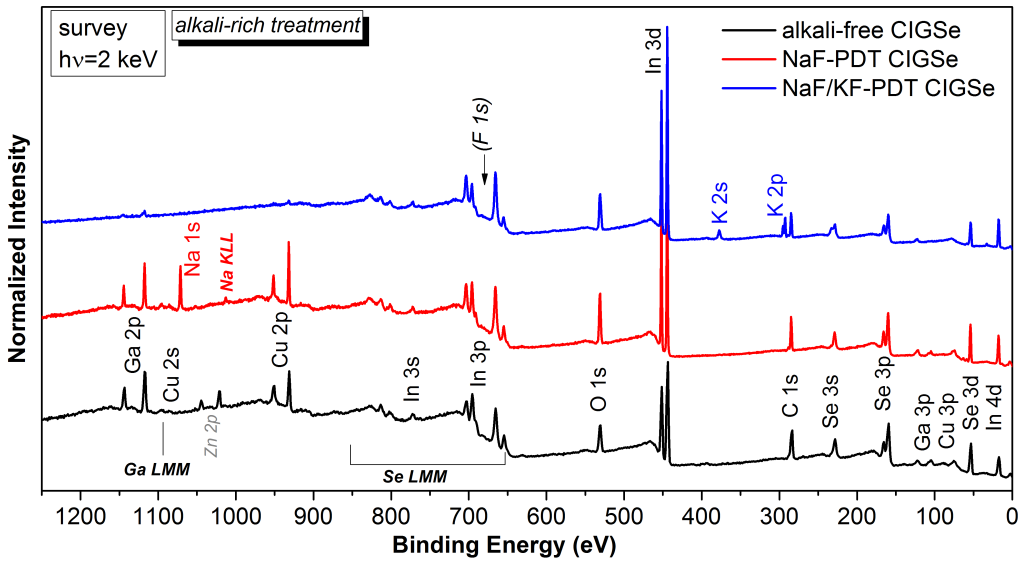

Figure 4.3: *Survey spectra of an alkali-free (black), a NaF-PDT (red), and a NaF/KF-PDT (blue) CIGSe absorber measured with an excitation energy of hν=2 keV. The post-deposition treated absorbers underwent an alkali-rich treatment. The core level and Auger lines are marked. The alkali-free absorber shows a slight Zn contamination of the surface. Vertical offset added.*

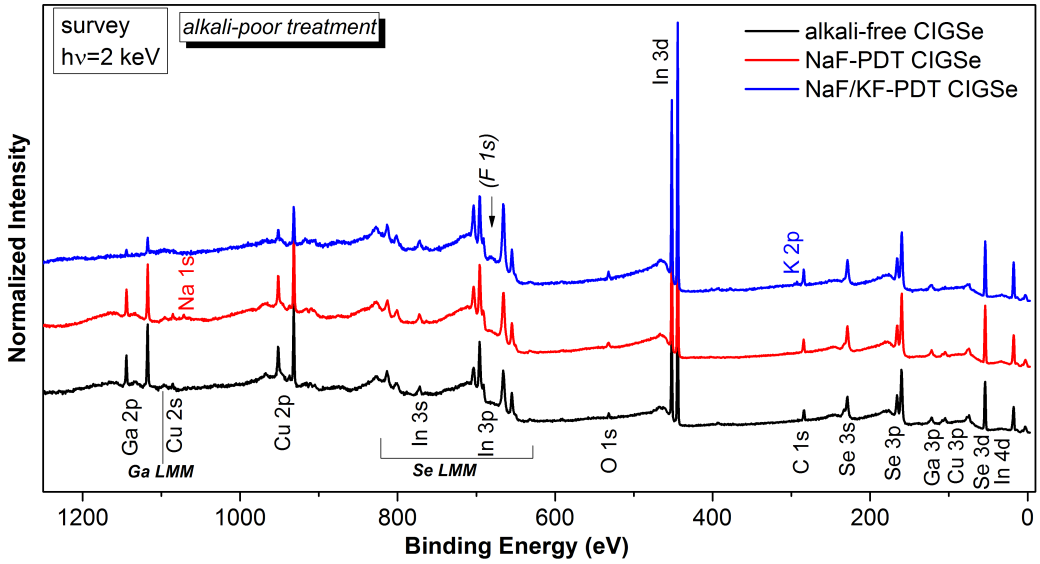

Figure 4.4: *Survey spectra of an alkali-free (black), a NaF-PDT (red), and a NaF/KF-PDT (blue) CIGSe absorber measured with an excitation energy of hν=2 keV. The post-deposition treated absorbers underwent an alkali-poor treatment. The core level and Auger lines are marked. Vertical offset added.*

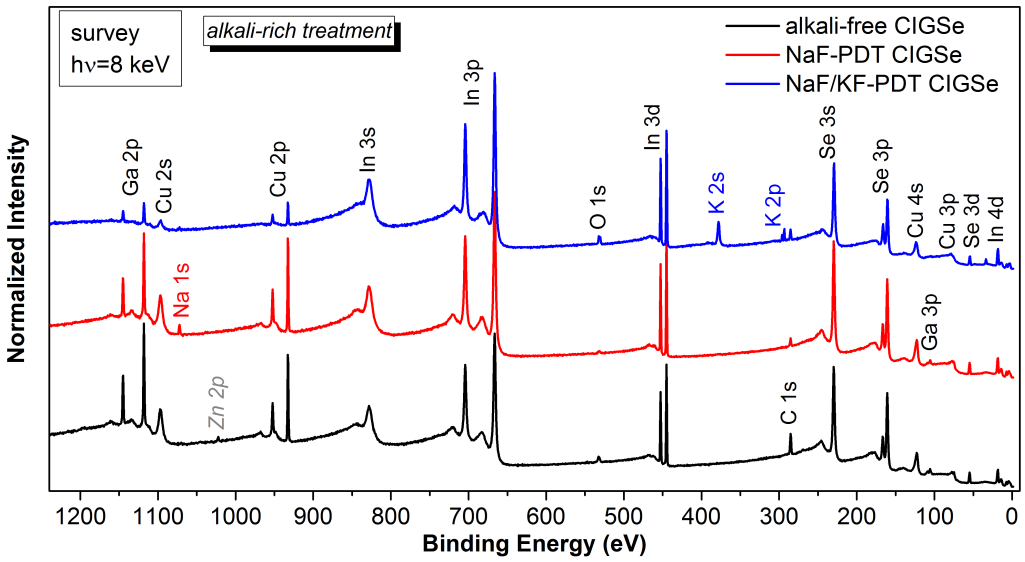

Figure 4.5: *Survey spectra of an alkali-free (black), a NaF-PDT (red), and a NaF/KF-PDT (blue) CIGSe absorber measured with an excitation energy of hν=8 keV. The post-deposition treated absorbers underwent an alkali-rich treatment. The core level and Auger lines are marked. The alkali-free absorber shows a slight Zn contamination of the surface. Vertical offset added.*

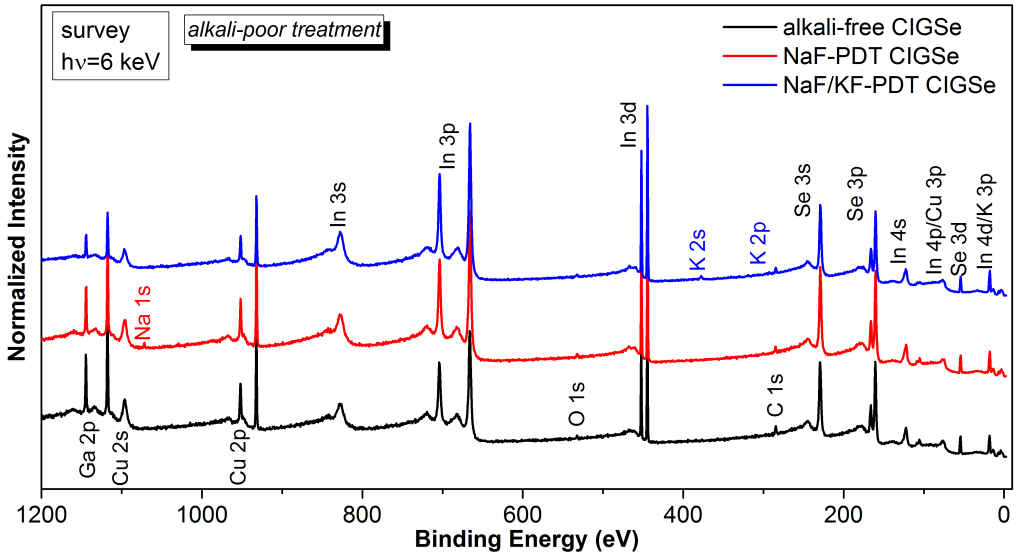

Figure 4.6: *Survey spectra of an alkali-free (black), a NaF-PDT (red), and a NaF/KF-PDT (blue) CIGSe absorber measured with an excitation energy of hν=6 keV. The post-deposition treated absorbers underwent an alkali-poor treatment. The core level and Auger lines are marked. Vertical offset added.*

Figure 4.2 shows the survey spectra of the first set of samples with an alkali-rich treatment of the respective CIGSe absorbers measured with Al K_α. For the alkali-free and the NaF-PDT CIGSe absorbers all Cu(In,Ga)Se_2 related core and Auger lines are present. The NaF/KF-PDT CIGSe shows a Cu- and Ga-depleted surface, which is almost devoid of Cu and Ga, in agreement with Ref. [4, 80]. Additionally, the corresponding alkali elements K (for the NaF/KF-PDT) and Na (only for the NaF-PDT) are present due to the incorporation during the PDT. It has already been suggested that K replaces Na during the PDT due to an ion-exchange mechanism [4, 102]. Note, there is no clear indication of F remnants from the NaF and KF treatments. Hence, the surface of the NaF/KF-PDT seems to be only composed of K-In-Se. Further, C 1s and O 1s are detected most likely due to surface contamination and will be intensively discussed in chapter 4.1.2.1.

Synchrotron-based HAXPES measurements were performed at 2 keV and 8 keV excitation, and the respective survey spectra are displayed in Figure 4.3 and Figure 4.5. Again, the alkali-free and NaF-PDT sample show the same behavior and all CIGSe related peaks. For the NaF/KF-PDT CIGSe Cu and Ga core levels can be noticeably detected for 8 keV measurements, however it is still Cu- and Ga-depleted compared to the NaF-PDT and alkali-free CIGSe. Even with more bulk-sensitive 8 keV measurements a distinct Na signal is only visible for the NaF-PDT CIGSe sample and only a weak signal for the NaF/KF-PDT CIGSe sample which is in agreement with the suggested ion-exchange [4, 102]. Even for 8 keV a distinct K signal can be detected for the NaF/KF-PDT CIGSe absorber.

A second set of samples, also prepared by Empa, with an alkali-poor treatment was measured at excitation energies of hν=2 keV and 6 keV and used for comparison. In this series the alkali-free and NaF-PDT CIGSe spectra show all material related core and Auger lines. As for the alkali-rich treatment Na is only detected for the NaF-PDT CIGSe but no Na signal for the NaF/KF-PDT CIGSe. A weak K signal compared to the alkali-rich series for the NaF/KF-PDT absorber can be detected. Again the NaF/KF-PDT shows a Cu- and Ga-depleted surface in comparison to the alkali-free and NaF-PDT CIGSe of this sample series. This first comparison of the survey spectra between the alkali-rich and alkali-poor series also reveals the further differences in PDT in addition to the SEM studies. Both Na and K are less pronounced for all excitation energies for the alkali-poor series. A more detailed analysis and explanation is given below in section 4.1.2.2. Also the alkali-rich sample set shows an increase in O 1s and C 1s signal intensity compared to the alkali-poor and is discussed in

chapter 4.1.2.1.

4.1.2.1 Effect of Surface Contamination and Oxidation

Before starting a detailed analysis and explanation of the CIGSe samples and the influence of alkali treatments on the chemical and later on the electronic structure, the effect of surface contamination/oxidation must be discussed.
It is already known that surface contamination and/or oxidation of the absorber surface can highly influence the performance of the solar cell [103–105], although these surface contaminants and oxides mainly get washed away during chemical bath deposition of CdS or KCN etch. However, for our analysis of the absorber surfaces it is important to discuss the influence of surface contamination and possible oxidation of the respective samples.

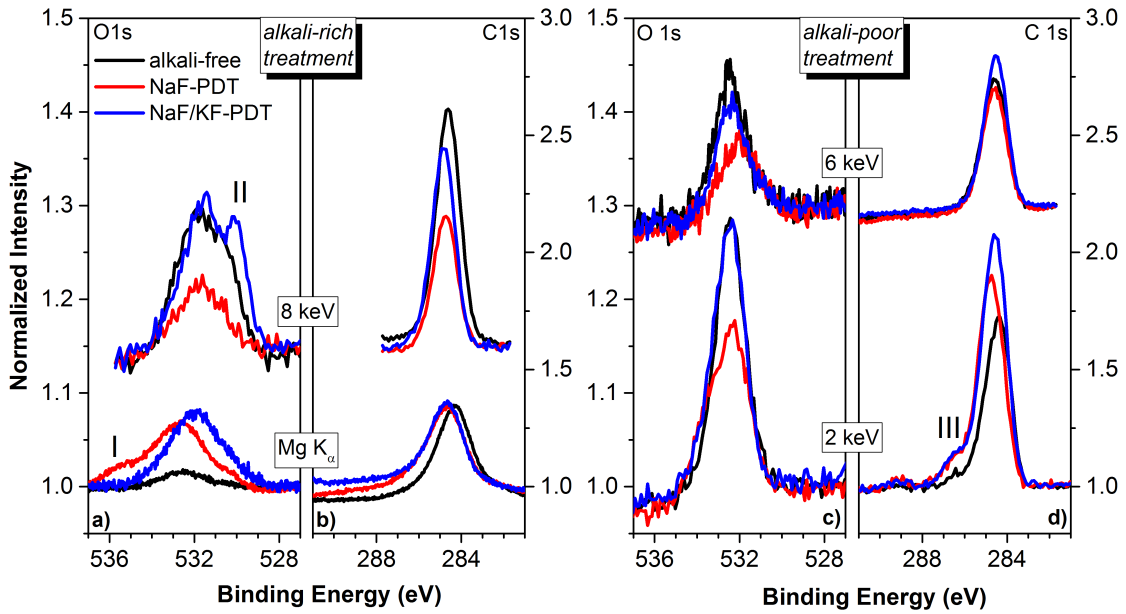

Figure 4.7: *O 1s and C 1s lines measured with excitation energies of hν=1253.56 eV (Mg K_α) and 8 keV for alkali-rich absorbers (a,b) and with hν=2 keV and 6 keV for the alkali-poor series (c,d). For each sample set the most surface sensitive and the "most" bulk-sensitive measurements are shown. The spectra are background normalized. Vertical offset added.*

As already seen in the survey spectra of Figure 4.2 to 4.6, O 1s and C 1s features can be detected for all examined samples, indicating varying degrees of contamination/oxidation. Figure 4.7 displays the O 1s and C 1s lines for each sample set (alkali-rich, alkali-poor) with the most surface sensitive measurement (Mg K_α, 2 keV) and the more bulk sensitive measurement (8 keV, 6 keV).

For the alkali-rich sample set the alkali-free absorber exhibits almost no oxygen for Mg K_α; by comparison the NaF-PDT and NaF/KF-PDT shows a significantly increased amount of oxygen on the sample surface. This increase in surface oxidation might be the result of the ammonia wash in ambient air and the vacuum drying process of the deionized water film and possible water remnants in the molybdenum frame. This might also explain the second species (indicated as I in Figure 4.7a) of surface contamination for the NaF-PDT sample, possibly due to a shorter storage time in UHV of the NaF-PDT CIGSe sample. All three samples show the same C 1s signal intensity for the Mg K_α-excited spectra (IMFP 2.7 nm). The 8 keV measurements (IMFP 12.3 nm) show also oxygen and carbon.
Although the samples were stored in a nitrogen filled glovebox the 8 keV measurements were conducted significantly later (about five month), and the samples had to be mounted in air, trying to keep the exposure time to ambient conditions at minimum. Especially, the second oxygen species (indicated as II in Figure 4.7a) for NaF/KF-PDT most likely indicates a surface-oxide compound.
However, if we compare the O 1s core level to In $3d_{5/2}$ we get less than 6% for the O1s:In3d ration for Mg K_α taking only the photoionization cross-sections in account, excluding the IMFP and the transmission function of the analyzer due to the close binding energy window for O 1s and In 3d. For 8 keV we get less than 14% O 1s:In 3d ration again only taking the respective photoionization cross-sections into account.
The same samples were used for the measurements with an excitation energy of 2 keV, which were performed 2-3 weeks after the 8 keV measurements. The results for the alkali-rich samples therefore show a significant amount of surface contamination/oxidation, which needs to be kept in mind for later analysis (and will be discussed where appropriate).
Note, that for this set of samples the 2 and 8 keV measurement of the alkali-free absorber show contamination by a Zn species. However, the Zn 2p:Cu 2p ratio for both excitation energies is only about 5%. This contamination will in particular effect the electronic structure, especially if it is a metallic Zn species. This surface contamination occurred during mild Ar^+-treatments and analyzing the sample in a different UHV system and are therefore only surface impurities.

To support all findings and measurements a second set of samples was prepared; differing deposition conditions at Empa resulted in an alkali-poor treatment. For this sample set, all absorbers show O 1s and C 1s signal for 2 and 6 keV measurements. The O 1s:In 3d ratio is about 15% for 2 and 6 keV measurements, except the alkali-free CIGSe sample exhibits an O 1s:In 3d ratio of about 30% for 6 keV. For 2 keV most likely carbonates (indicated as III in Figure 4.7d) at higher binding energy ($E_B \sim 288$ eV) are detected. Here, the time between sample preparation and measurements was kept as short as possible and the samples were mounted in nitrogen atmosphere and only briefly saw air (<5 min) while introducing into the UHV system.

However, both sample sets show a contamination/oxidation layer of the sample surface most likely due to physisorption effects. Incorporation of carbon and oxygen into the absorber during absorber growth also cannot be excluded, especially given the significant signal observed in the more bulk sensitive 6 and 8 keV measurements. In this context differences in analyzer transmission function for electrons at different kinetic energies and difference in cross-section (see chapter 3.6.2) cannot be neglected. Furthermore as already explained in chapter 3.6 despite varying excitation energy and therefore probing-depth, due to exponential behavior, signal from the sample surface will always be detected.

4.1.2.2 Depth-dependent Composition

In order to get a depth-dependent picture of the composition of the alkali-rich and alkali-poor absorber sample sets, we used photoelectron spectroscopy with different excitation energies (Mg K_α, 2 keV, 6 keV, and 8 keV) resulting in a variation in IMFP of the photoelectrons from around max. 2.7-12.3 nm [79] (see also section 3.6) for high kinetic energies. To derive the sample-specific compositions, we have used the intensity of the shallow core levels Cu 3p, Na 2s, Se 3d, K 3s, Ga 3d, and In 4d, which fall within a narrow energy range (approximately 70 eV). With this approach we are able to neglect the variations in electron analyzer transmission and IMFP on signal intensity when quantifying the XPS/HAXPES results. Additionally when using the shallow core levels we have similar low binding energies and therefore comparable high kinetic energies (between ∼1180 and 1240 eV for Mg K_α, ∼1925 and 1990 eV for 2 keV, ∼5875 and 5937 eV for 6 keV, and ∼7865 and 7927 keV for 8 keV) and the samples are least affected and similarly attenuated by surface contamination and/or oxidation of a given sample. As already discussed in section 4.1.2.1 for these data sets it is important to consider contamination/oxidation, as oxygen and carbon are detected

on all investigated samples for all excitation energies. However, we do not include carbon and oxygen in the quantitative analysis assuming those contaminants are mainly located on the surface.

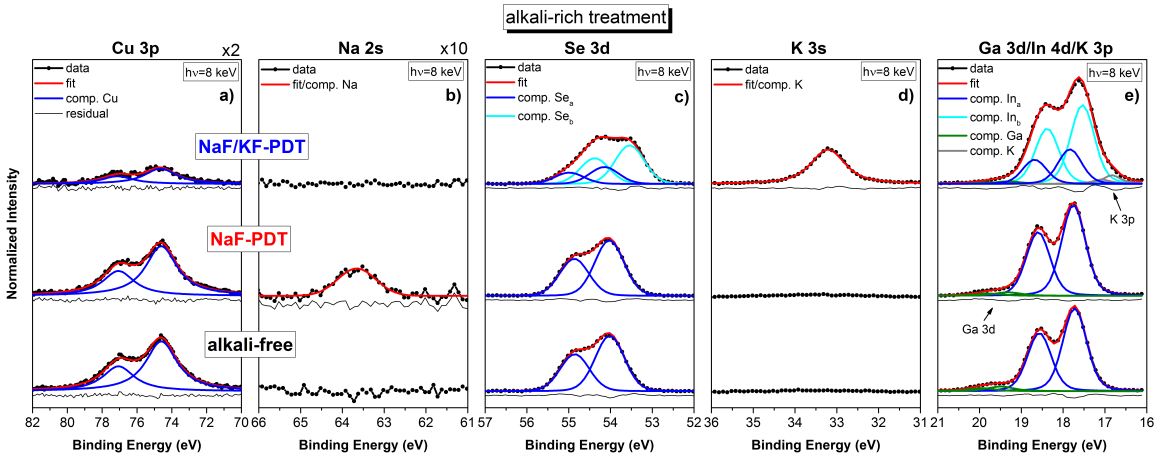

Figure 4.8: *Shallow core level photoemission data of the CIGSe absorber with an alkali-rich NaF-PDT and NaF/KF-PDT taken with an excitation energy of hν=8 keV. Cu 3p (a), Na 2s (b), Se 3d (c), K 3s (d), and Ga 3d/In 4d/ K 3p (e) are displayed with their respective doublet Voigt fits and residua. Vertical offset added. Adapted from [100].*

Figure 4.8 and Figure 4.9 exemplarily display Cu 3p, Na 2s, Se 3d, K 3s, and Ga 3d/In 4d/K 3p with the according fits for the alkali-rich absorber set probed with 8 keV and the alkali-poor absorbers measured at 6 keV. The remaining shallow core level fits for e xcitation energies of Mg K_α and 2 keV are included in Appendix A.2.
The shallow core levels are simultaneously fitted with Voigt profiles [106] and linear backgrounds; the backgrounds have been subtracted in all figures (see also chapter 3.6). Shape and gwidth [106] are linked for each excitation energy and the doublet separation is fixed to 2.39 eV [107] for Cu 3p (panels a). The Se 3d data (panels c) are fitted using a doublet separation of 0.83 eV [108]. For the NaF/KF-PDT CIGSe sample two (three) species are needed for 8 keV (2 keV) for the alkali-rich NaF/KF-PDT and two species for 2 keV and 6 keV for alkali-poor NaF/KF-PDT, with the same doublet separation, shape and gwidth. The blue doublet, representing species Se_a, and the cyan doublet, representing species Se_b. For the 2 keV measurement (see [99] and Appendix A.2) an additional orange doublet (species Se_c) is most likely the result of surface oxidation of the sample as explained in section 4.1.2.1. The panels e) show the fits for Ga 3d, In 4d, and K 3p lines. In 4d has a doublet separation of 0.86 eV [109], Ga 3d of 0.46 eV [110], and K 3p of 0.25 eV [111]. Due to the Ga-depleted

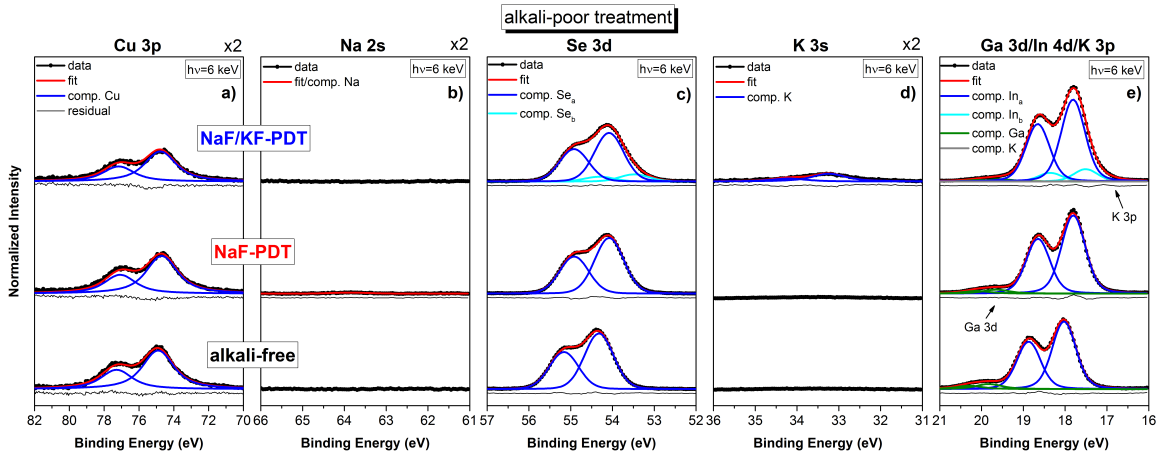

Figure 4.9: *Shallow core level photoemission data of the CIGSe absorber with an alkali-poor NaF-PDT and NaF/KF-PDT taken with an excitation energy of hν=8 keV. Cu 3p (a), Na 2s (b), Se 3d (c), K 3s (d), and Ga 3d/In 4d/ K 3p (e) are displayed with their respective doublet Voigt fits and residua. Vertical offset added. Adapted from [99].*

surface for the NaF/KF-PDT CIGSe sample and correspondingly low Ga 3d intensity, the Ga $3d_{5/2}$ position of NaF/KF-PDT CIGSe sample is fixed to the Ga $3d_{5/2}$ position of NaF-PDT CIGSe for the Mg K_α and 2 keV analysis. Also for the In 4d line of the NaF/KF-PDT CIGSe two species are necessary to get to a reasonable fit. Again, the blue doublet represents species In_a and the cyan doublet represents species In_b. For the 2 keV measurement (see [99] and Appendix A.2) an additional orange doublet (species In_c) is requiered for a reasonable fit and most likely the result of surface oxidation of the sample. The ratio between the In_a:In_b components is the same as found for Se 3d data and 3.81 (2 keV) and 2.28 (8 keV) for alkali-rich, as well as 0.39 (2 keV) and 0.15 (6 keV) for alkali-poor, respectively. K 3p is linked in area and position to the nearby K 3s signal, taking into account the respective cross-section ratio [84] for the area and an energy separation of K 3s (E_B(K)=34.70 eV [112]) and K $3p_{3/2}$ (E_B(K)=18.34 eV[111]) of 16.36 eV.

Figure 4.8a and Figure 4.9a show the Cu 3p lines, after correction by the In 4p background (see Appendix A.1), for the alkali-free, NaF-PDT, and NaF/KF-PDT absorbers for both absorber sample sets. Both NaF/KF-PDT samples show a Cu depletion with respect to the alkali-free and the NaF-PDT CIGSe, in agreement with Ref. [4, 80]. However, it is clearly seen that the alkali-rich treated NaF/KF-PDT CIGSe absorber shows significantly less copper for the more bulk sensitive 8 keV measurement as a result of different PDT parameters. The Se 3d lines suggest only one species for both alkali-free and NaF-PDT absorbers (see

4.8c and 4.9c). The NaF/KF-PDT CIGSe features a second species (Se_b) at low binding energy side, which we attribute to a K-In-Se type species. By implication, this attribution means that the high binding contribution (Se_a) represents the chalcopyrite structure (CIGSe), with a binding energy similar to that of the alkali-free and NaF-PDT CIGSe. The Se 3d fits for NaF/KF-PDT of the alkali-rich and alkali-poor absorber already indicate that the contribution of a K-In-Se type species (Se_b) in the alkali-poor absorbers is smaller than in the alkali-rich absorbers.
Similar effects are seen in the core level fits for In 4d. Once more the NaF/KF-PDT absorbers are depicted by two components with a K-In-Se type species (In_b) at lower binding energy side and a CIGSe-species (In_a) matching the energy positions for alkali-free and NaF-PDT CIGSe. The K-In-Se type species is again more pronounced for the alkali-rich treatment than for the alkali-poor NaF/KF-PDT treatment. Further potassium (K 3s (4.8d, 4.9d) and K 3p (4.8e, 4.9e)) is only apparent for the NaF/KF-PDT samples. Hence, a clear Ga contribution is only seen for the alkali-free and NaF-PDT CIGSe absorbers, however slightly more Ga is detected for the alkali-poor NaF/KF-PDT than for the respective alkali-rich sample.
As already mentioned potassium is only seen for the potassium treated samples, but a second K-species is detected at higher binding energy (see Figure 4.9d) for the alkali-poor NaF/KF-PDT. Possibly due to "unreacted" potassium, or K-In-Se/K-Se impurities [113].
Na 2s is shown in Figure 4.8b and 4.9b but will be neglected from further analysis. The amount of Na found for the alkali-rich NaF-PDT CIGSe is less than 10 % that of K observed for the alkali-rich NaF/KF-PDT CIGSe sample at 8 keV and even less for the alkali-poor CIGSe absorbers.
Note, due to a poorer resolution of the XPS Mg K_α source only one species for Se and In of the alkali-rich NaF/KF-PDT can be observed, however a K-In-Se type species and a CIGSe species at the absorber surface is also assumed in this case.

Using the photoemission data (Figure 4.8, Figure 4.9 and Appendix A.2) of the respective shallow core levels, the relative Cu, In, Ga, Se, and K to (Cu+In+Ga+Se+K) can be derived as a function of the employed excitation energy and thus IMFP, displayed in Figure 4.10 and 4.11 for the alkali-rich treated CIGSe absorber set and in Figure 4.12 and 4.13 for the alkali-poor absorbers. All photoemission signal intensities are related to the relative quantity of the element in question, weighted exponentially according to the IMFP and corrected by the respective photoionization cross-section for used excitation energy (see chapter 3.6.2). For this purpose, the obtained values would reflect the true composition (within the experimental uncertainty and calculated margins) if the samples had uniform composition throughout the investigated volume. However, for nonuniform materials, like CIGSe, the

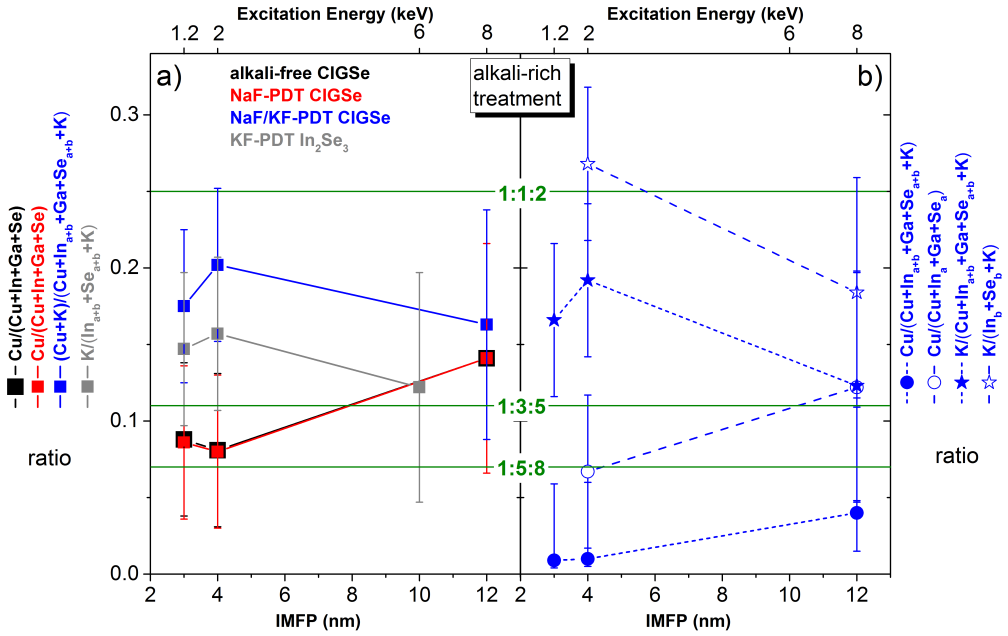

Figure 4.10: *The elemental ratios of (Cu+K), (In+Ga), and Se to the overall amount of ($Cu+In_{a+b}+Ga+Se_{a+b}+K$) of differently treated alkali-rich (CIGSe) absorbers taken with excitation energy of $h\nu$ =1253.56 eV (Mg K_α), 2 keV, 6 keV, and 8 keV resulting in IMFPs of 2.7, 4.0, 9.7, and 12.3 nm.[79] The composition of the alkali-free CIGSe (black) is compared to absorbers that underwent a NaF (red) post-deposition treatment (PDT), and a NaF/KF-PDT (blue). For reference the ratio of a KF-PDT In_2Se_3 (gray) sample is also shown. For the NaF/KF-PDT CIGSe sample the individual $Cu/(Cu+In_{a+b}+Ga+Se_{a+b}+K)$ and $K/(Cu+In_{a+b}+Ga+Se_{a+b}+K)$ ratios (short dashed lines) as well as the Cu, (In+Ga),and Se to ($Cu+In_a+Ga+Se_a$) and K, In, and Se to($K+In_b+Se_b$) ratios (long dashed lines, open symbols) representing a corresponding Cu-In-Ga-Se and K-In-Se composition are additionally presented. The most common CIGSe-related stoichiometries ([Cu+K]:[In+Ga]:[Se] = 1:1:2, 1:3:5, and 1:5:8) are depicted in green. A general error margin of $\pm$0.05 eV for Mg K_α and 2 keV, and $\pm$0.075 eV for 6 and 8 keV, is assumed. Adapted from [100].*

results will represent an integrated composition throughout the volume of interest under the further assumption that the main carbon and oxygen contributions arise from surface contamination/oxidation and are therefore not included in the calculated composition.
It should be noted, that there are many different nonuniform compositions that could explain the findings here. It is almost impossible to give an exact composition due to the assumption of a nonuniform composition, nanopatterned surfaces of the NaF/KF-PDT CIGSe absorbers, the uncertainty in determining the corresponding photoionization cross-sections, especially for 6 and 8 keV, and the distributions of different species for Se and In. Therefore, we give

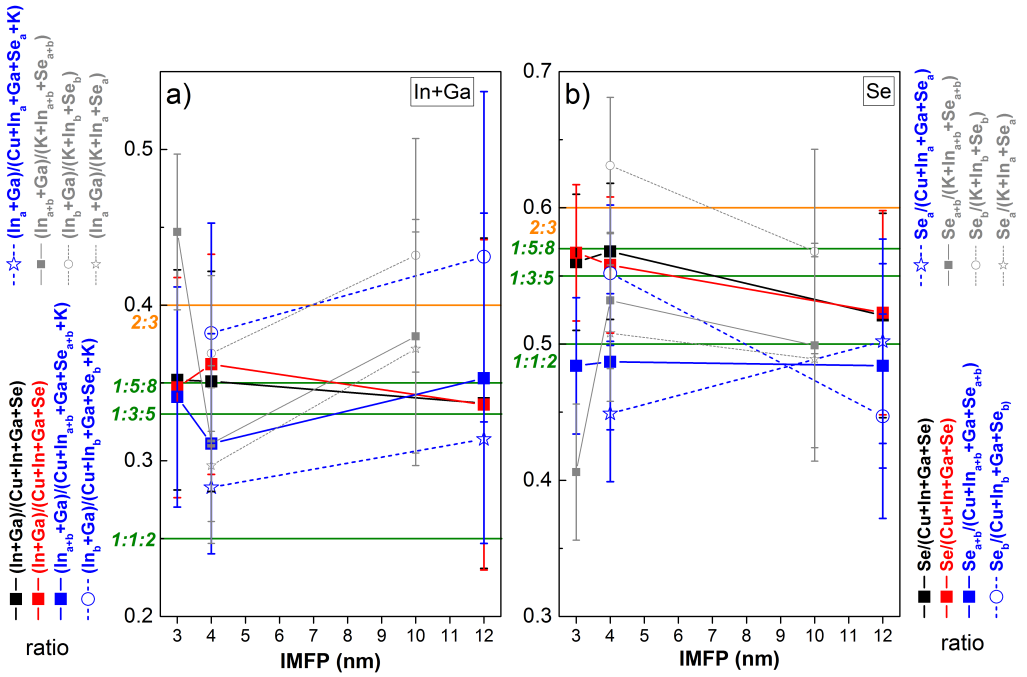

Figure 4.11: *(In+Ga)/(Cu+In+Ga+Se+K+Na), left, and Se/(Cu+In+Ga+Se+K+Na), right, ratios of differently treated alkali-rich Cu(In,Ga)Se_2 (CIGSe) absorbers, derived from photoemission data recorded with excitation energies of hν =1253.56 eV (Mg K_α), 2 keV, 6 keV, and 8 keV, resulting in IMFPs of 2.7, 4.0, 9.7, and 12.3 nm. The composition of the alkali-free CIGSe (black) is compared to absorbers that underwent a alkali-rich NaF-PDT (red) or a NaF/KF-PDT (blue), and to a KF-PDT In_2Se_3 reference (gray). For the NaF/KF-PDT CIGSe absorber, the relative (In+Ga)/(Cu+In_a+Ga+Se_a) and Se/(Cu+In_a+Ga+Se_a) ratios (dashed blue lines, open circular symbol) as well as the relative In/(K+In_b+Se_b) and Se/(K+In_b+Se_b) ratios (dashed blue lines, open star symbol) are shown. These ratios are also depicted for the KF-PDT In_2Se_3 reference, i.e., In/(In_a+Se_a) and Se/(In_a+Se_a) (dashed gray lines, open circles) and In/(K+In_b+Se_b) and Se/(K+In_b+Se_b) (dashed gray lines, open stars). The most common CIGSe-related compositions (1:1:2, 1:3:5, and 1:5:8) are depicted in green, as well as In:Se=2:3 for In_2Se_3 in orange. A general error margin of ±0.05 eV for Mg K_α and 2 keV, and ±0.075 eV for 6 and 8 keV, is assumed.*

a depth-dependent picture and behavior of the elements of interest, displayed in Figure 4.10, 4.11 and 4.12, 4.13 and discuss it qualitatively.

First, we start by interpreting the compositional results for the alkali-rich CIGSe absorbers displayed in 4.10 and 4.11 (see also Ref. [100]). The Cu, (In+Ga), and Se to (Cu+In_{a+b}+Ga+Se_{a+b}) profiles for the alkali-free and NaF-PDT CIGSe are almost identical. For these ab-

sorbers the surface is Cu-poor and In-rich in comparison to the nominal Cu:(In,Ga):Se=1:1:2 stoichiometry. Cu-poor surfaces on high-efficient chalcopyrite absorbers have been reported [30, 31, 114] and attributed to surface reconstruction [115] or the formation of ordered defect/vacancy surface compounds [31, 116]. These well-known compositions with a 1:3:5 and 1:5:8 structure are indicated in green in Figure 4.10, 4.11 and 4.12, 4.13. The more bulk-sensitive 8 keV measurement shows an increase in Cu content, whereas (In+Ga) and Se (see Figure 4.13a,b) stay almost constant. The content of In and Ga, and therefore the (In+Ga), as well as the Se content are consistent with Cu-deficient compositions like 1:3:5 and/or 1:5:8.

In contrast, the surface of the alkali-rich treated NaF/KF-PDT CIGSe is almost devoid of Cu in comparison to the alkali-free and NaF-PDT samples (see Figure 4.10b), as reported in [4, 80]. A significant and detectable Cu 3p signal for the alkali-rich NaF/KF-PDT is only found for the most bulk sensitive 8 keV measurements. For 2 keV a weak Cu 2p signal is already detected and therefore the amount of copper for Cu 3p for this sample was estimated (for more details see Appendix A.3) due to the low signal to noise ratio of the measured data. Within the experimental uncertainty the amount of copper derived for 8 keV is approaching the Cu content that is found at the surface of the alkali-free and NaF-PDT CIGSe. The overall content of In, Ga, and Se to (Cu+In_{a+b}+Ga+Se_{a+b}+K) also deviates from what is found for the alkali-free and NaF-PDT sample. For the alkali-rich treated NaF/KF-PDT sample a significant amount of K/(Cu+K+In_{a+b}Ga+Se_{a+b}) is found at the surface, indicated in Figure 4.10b (additionally see survey spectra 4.2, 4.3, 4.5, and [4, 80]). With increasing IMFP and thus increasing bulk sensitivity the K content decreases and therefore shows an opposite behavior to the Cu content for this sample. DFT calculations suggest that K may preferentially occupy Cu vacancies in a Cu-poor CIGSe material.[117] This model supports our suggestions that a K-In-Se type surface compound is formed and is in agreement with what we find for the electronic structure (detail discussion in 4.2 and [80, 113]). To verify this statement, by assuming that K occupies a certain amount of Cu vacancies, we indicate a (Cu+K) content in Figure 4.10a) and get a (Cu,K):(In,Ga):Se composition tending towards a stoichiometric 1:1:2 composition. This assumption is also in general agreement with what is observed for (In+Ga) and Se in Figure 4.11, but due to the large error bars a final conclusion cannot be made.

To further elucidate these findings of the NaF/KF-PDT CIGSe surface composition we use a KF-PDT In_2Se_3 reference sample. The overall K/(K+In_{a+b}+Se_{a+b}) content is represented in 4.10a and indicating either the formation of a $KInSe_2$-In_2Se_2 mixture or a K-deficient K:In:Se – type species. Recently, studies of $Cu_{1-x}K_xInSe_2$ alloys showed that impurity

phases like $K_2In_{12}Se_{19}$ and K_2Se are found for $KInSe_2$ films.[113] Although the KF-PDT In_2Se_3 deposition condition might have been different, the depicted K/(Cu+K+In_{a+b}+Ga+Se_{a+b}) profile of the alkali-rich NaF/KF-PDT CIGSe follows a similar trend.
Taking a closer look at the separated species for the NaF/KF-PDT sample the K/(K+In_b+Se_b), In/(K+In_b+Se_b), and Se/(K+In_b+Se_b) suggest within the error bars a 1:1:2 stoichiometry. For the CIGSe species the Cu/(Cu+In_a+Ga+Se_a) shows the same behavior as the alkali-free and NaF/KF-PDT sample and a stoichiometry between Cu:(In+Ga):Se=1:3:5 and 1:5:8. However, although the (In+Ga)/(Cu+In_a+Ga+Se_a) and Se/(Cu+In_a+Ga+Se_a) follows a similar trend to the potassium free absorbers they do not exactly match the stoichiometry. These findings suggest a K-In-Se/CIGSe bilayer structure.

The same interpretation and analysis is also done for the alkali-poor CIGSe absorber set displayed in Figure 4.12 and 4.13. As for the alkali-rich treated samples, the alkali-free and NaF-PDT CIGSe are quite similar in their (Cu+K) (Figure 4.12a), (In+Ga) (Figure 4.13a), and Se (Figure 4.13b) ratio. Both samples also show a Cu-deficient surface compared to the nominal Cu:(In+Ga):Se=1:1:2 stoichiometry for the bulk. For the more bulk-sensitive 6 keV measurement the Cu content increases. The alkali-free and NaF-PDT CIGSe sample show an increase in (In+Ga) ratio and a decrease in Se deeper beneath the surface. Within the error bars they can also be associated with a Cu:(In+Ga):Se=1:3:5 or 1:5:8 stoichiometry found for Cu-poor CIGSe surfaces.

As opposed to the alkali-rich NaF/KF-PDT CIGSe sample the effect of an additional KF treatment is less pronounced for the alkali-poor NaF/KF-PDT but still distinguishable. A marginally Cu-poorer surface is depicted for the NaF/KF-PDT sample, although already for 2 keV the amount of Cu is noticeable especially in comparison to the alkali-rich NaF/KF-PDT sample. The compositional changes for Cu and in particular for (In+Ga) and Se do not deviate a lot within the experimental uncertainties from the alkali-free and NaF-PDT CIGSe absorber. To illustrate the occupation of Cu vacancies with K [117], the (Cu+K)/(Cu+In_{a+b}+Ga+Se_{a+b}+K) is shown indicating (Cu+K) that fits to a 1:3:5 composition. The (In+Ga) and Se only fit to 1:3:5 within the bigger error margins. The K/(K+In_b+Se_b) profile (Figure 4.12b) indicates Se deficiency and cannot be associated with a simple K:In:Se=1:1:2 stoichiometry, but may be explained by formed $Cu_{1-x}K_xInSe_2$ alloys or incorporated impurities as for reported $KInSe_2$ films [113].
The difficulty in identifying the K-In-Se species and the CIGSe composition may arise with the nonuniformity of this sample, as well as the presence of a really thin covering layer,

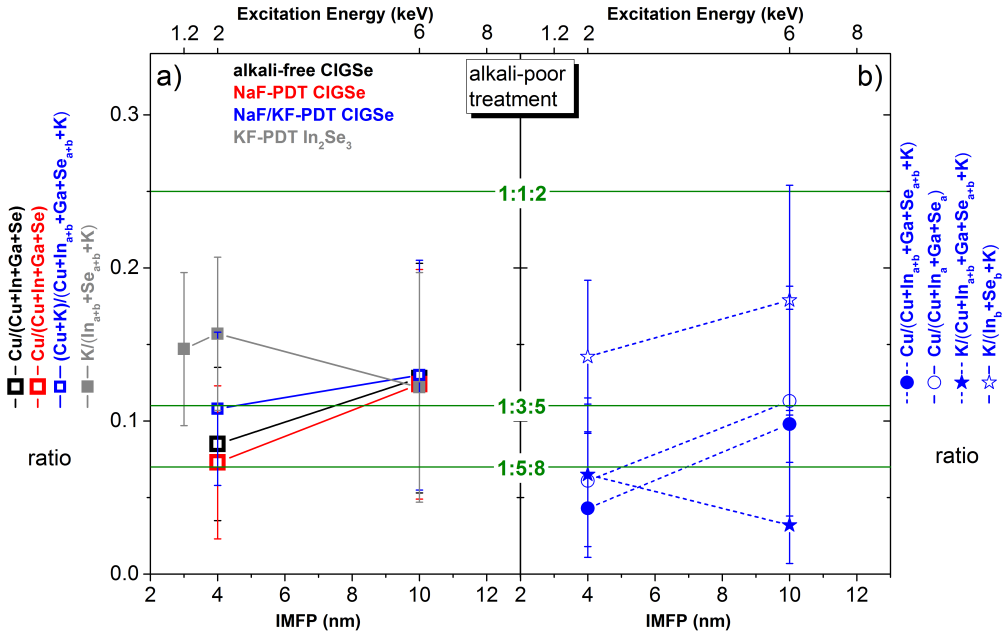

Figure 4.12: *The elemental ratios of (Cu+K) to the overall amount of ($Cu+In_{a+b}+Ga+Se_{a+b}+K$) of differently treated alkali-poor Cu(In,Ga)Se_2 (CIGSe) absorbers taken with excitation energy of hν =1253.56 eV (Mg K_α), 2 keV, and 6 keV resulting in IMFPs of 2.7, 4.0, and 9.7 nm.[79] The composition of the alkali-free CIGSe (black) is compared to absorbers that underwent a NaF (red) post-deposition treatment (PDT), and a NaF/KF-PDT (blue). For reference the ratio of a KF-PDT In_2Se_3 (gray) sample is also shown. For the NaF/KF-PDT CIGSe sample the individual Cu/($Cu+In_{a+b}+Ga+Se_{a+b}+K$) and K/($Cu+In_{a+b}+Ga+Se_{a+b}+K$) ratios (short dashed lines, half-filled symbol) as well as the Cu to ($Cu+In_a+Ga+Se_a$) and K to($K+In_b+Se_b$) ratios (long dashed lines, open symbols) representing a corresponding Cu-In-Ga-Se and K-In-Se composition are additionally presented. The most common CIGSe-related stoichiometries ([Cu+K]:[In+Ga]:[Se] = 1:1:2, 1:3:5, and 1:5:8) are depicted in green. A general error margin of ±0.05 eV for Mg K_α and 2 keV, and ±0.075 eV for 6 keV, is assumed.*

probably exhibiting a gradient-like structure than a bilayer, with an additional nanopatterned surface structure with a second potassium species. However trends are comparable to the alkali-rich NaF/KF-PDT CIGSe, only less distinct.

It can be speculated that the less intensive NaF/KF-PDT treatment for the alkali-poor treated sample resulting in a (Cu+K):(In+Ga):Se=1:3:5 surface structure, instead of a 1:1:2-like composition as for the alkali-rich NaF/KF-PDT CIGSe sample, may explain the decrease in V_{OC}, FF, and efficiency (see Table 2.1) compared to the alkali-rich treated NaF/KF-PDT.

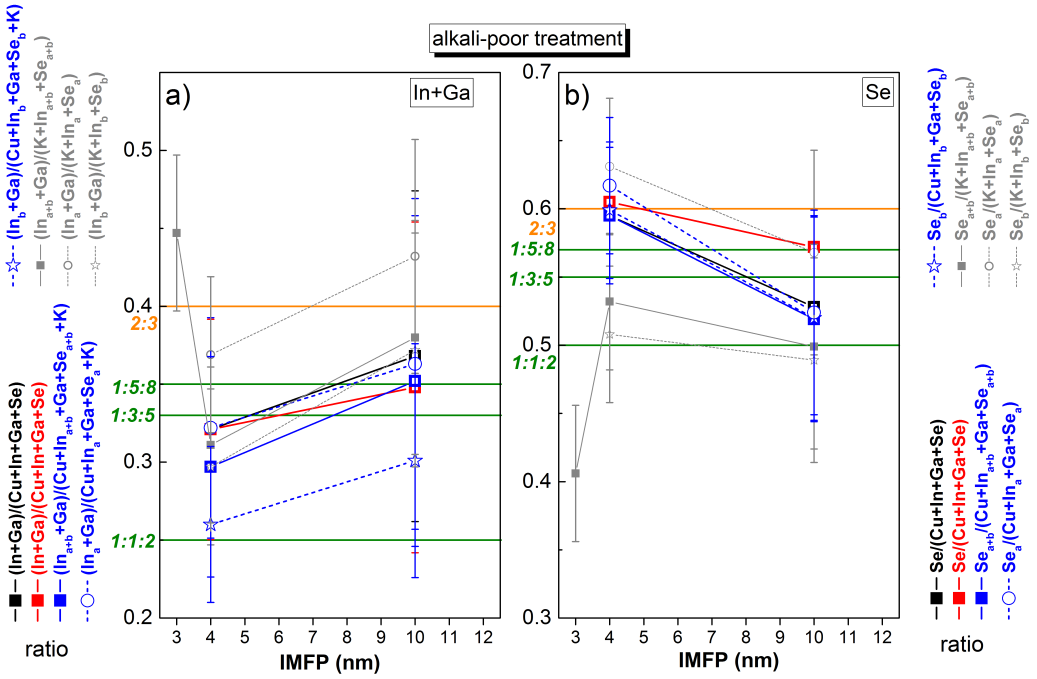

Figure 4.13: *(In+Ga)/(Cu+In+Ga+Se+K+Na), left, and Se/(Cu+In+Ga+Se+K+Na), right, ratios of differently treated alkali-poor Cu(In,Ga)Se_2 (CIGSe) absorbers, derived from photoemission data recorded with excitation energies of hν =1253.56 eV (Mg K_α), 2 keV, and 6 keV resulting in IMFPs of 2.7, 4.0, and 9.7 nm. The composition of the alkali-free CIGSe (black) is compared to absorbers that underwent a alkali-poor NaF-PDT (red) or a NaF/KF-PDT (blue), and to a KF-PDT In_2Se_3 reference (gray). For the NaF/KF-PDT CIGSe absorber, the relative (In+Ga)/(Cu+In_a+Ga+Se_a) and Se/(Cu+In_a+Ga+Se_a) ratios (dashed blue lines, open circular symbol) as well as the relative In/(K+In_b+Se_b) and Se/(K+In_b+Se_b) ratios (dashed blue lines, open star symbol) are shown. These ratios are also depicted for the KF-PDT In2Se3 reference, i.e., In/(In_a+Se_a) and Se/(In_a+Se_a) (dashed gray lines, open circles) and In/(K+In_b+Se_b) and Se/(K+In_b+Se_b) (dashed gray lines, open stars). The most common CIGSe-related compositions (1:1:2, 1:3:5, and 1:5:8) are depicted in green, as well as In:Se=2:3 for In_2Se_3 in orange. A general error margin of ±0.05 eV for Mg K_α and 2 keV, and ±0.075 eV for 6 keV, is assumed.*

To finalize the depth-dependent composition the ratios Ga:(In+Ga), (Ga+In):Cu, Se:Cu, Se:K, and (Ga+In):K are derived and summarized in Figure 4.14 for alkali-rich and alkali-poor samples.

For both sample sets (alkali-rich and alkali-poor) the alkali-free and NaF-PDT show the same trends in Ga:(In+Ga), (Ga+In):Cu, Se:Cu and support the previous findings of the elemental contents. This also suggests that the Zn contamination for the alkali-free CIGSe of

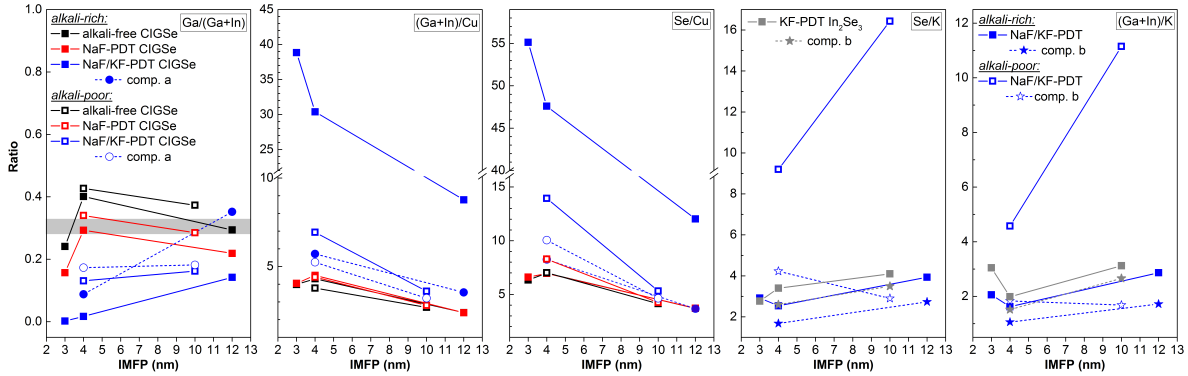

Figure 4.14: *The elemental ratios of Ga:(In+Ga), (Ga+In):Cu, Se:Cu, Se:K, and (Ga+In):K of differently treated CIGSe absorbers taken with excitation energy of hν =1253.56 eV (Mg K_α), 2 keV, 6 keV, and 8 keV resulting in IMFPs of maximum 2.7, 4.0, 9.7, and 12.3 nm.[79] The composition of the alkali-free CIGSe (black) is compared to absorbers that underwent a NaF (red) post-deposition treatment (PDT), and a NaF/KF-PDT (blue).*

the alkali-rich absorber series has no major influence on the chemical structure. However, it cannot be excluded that Zn has an impact, but it is impossible to distinguish it in our analysis; the Zn:Cu ratio is about 5%. Note, that it is suggested that Zn can occupy Cu vacancies.[118] The Ga:(In+Ga) aligns with the preferred average bulk ratio of 0.33-0.38 [4] for high-efficient solar cells. Due to the Cu-depleted surface the ratio for (Ga+In):Cu is still higher for the very surface, but it is tending to the desired ratio of 1.21-1.28 [4]. This behavior is also in agreement with the Se:Cu ratio for these samples, especially for the almost Cu devoid NaF/KF-PDT CIGSe of the alkali-rich sample series. Also the derived CIGSe compounds for both NaF/KF-PDT absorbers show similar ratios as the respective alkali-free and NaF-PDT CIGSe.

4.1.2.3 Modified Auger Parameter α' for Indium and Selenium

For a more direct examination of the impact of alkali treatments especially on the chemical speciation of the alkali-free, NaF-PDT, and NaF/KF-PDT CIGSe absorbers of the alkali-rich treated sample series, we use the In $M_4N_{45}N_{45}$ (Figure 4.15) and Se $L_3M_{45}M_{45}$ Auger Lines (Figure 4.16).

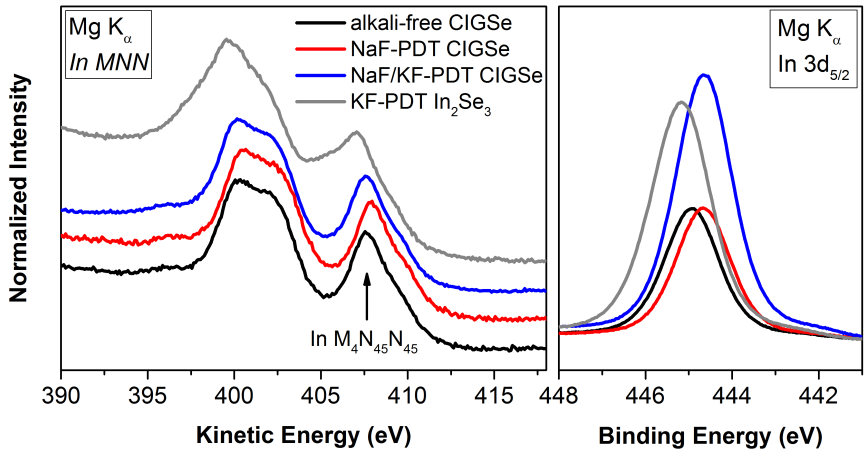

Figure 4.15: *In MNN Auger line (left panel) for different CIGSe absorbers together with the respective In $3d_{5/2}$ core level line (right panel).*

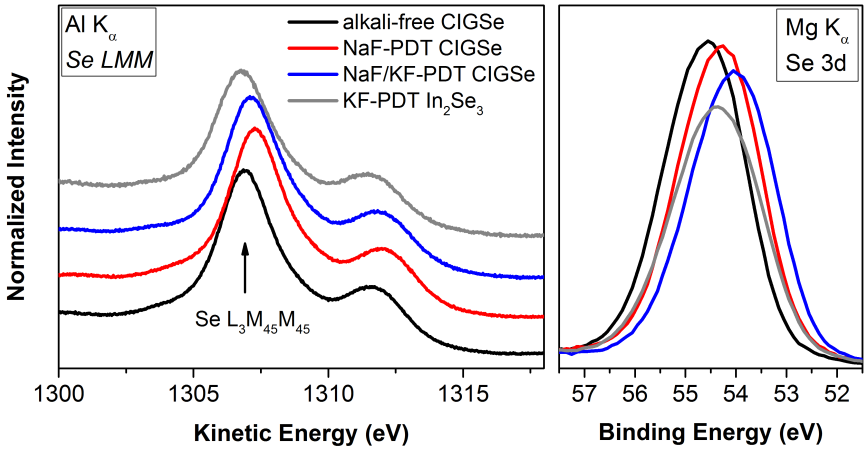

Figure 4.16: *Se LMM Auger line (left panel) for different CIGSe absorbers together with the respective Se 3d core level line (right panel).*

To be independent of variations in doping concentration, possible (surface) band bending, and/or sample charging, the modified Auger parameter α' of selenium $\alpha'(\mathrm{Se}) = E_B(\mathrm{Se\ 3d_{5/2}}) + E_K(\mathrm{Se\ LMM})$ and indium $\alpha'(\mathrm{In}) = E_B(\mathrm{In\ 3d_{5/2}}) + E_K(\mathrm{In\ MNN})$ is calculated (see also chapter 3.2).

Both Auger spectra show almost identical structures for alkali-free, NaF-PDT, and NaF/KF-PDT CIGSe, only slight shifts in kinetic energy can be observed. The same shifts are also obvious for the respective core level lines of In $3d_{5/2}$ and Se 3d.
A different shape is exhibit for the In MNN Auger line for the KF-PDT In_2Se_3 reference sample. Table 4.1 shows the derived values for In $3d_{5/2}$, Se $3d_{5/2}$, In $M_4N_{45}N_{45}$, and Se $L_3M_{45}M_{45}$ of the alkali-free, NaF-PDT, NaF/KF-PDT CIGSe, and the KF-PDT In_2Se_3 reference sample (data see Figure 4.15 and 4.16).

Indium MNN Auger kinetic energies for $CuIn_3Se_5$ are found at 407.40 eV [119] and at 408.40 eV for $CuInSe_2$ [104]. The respective core level lines for In $3d_{5/2}$ are in a range of E_B=444.10 eV - 444.80 eV [104, 120] for $CuInSe_2$. In_2Se_3 Auger kinetic energies are located between 408.00 - 408.30 eV [104, 121] and 444.80 - 445.10 eV In $3d_{5/2}$ binding energy [103, 121].
Metallic indium has In MNN Auger kinetic energies of 409.60 - 410.40 eV [121, 122] and In $3d_{5/2}$ binding energies of 443.15 - 444.60 eV [123, 124]. In-O can be found at binding energies around (444.7±0.7) eV and Auger kinetic energies of approximately 406.6 eV. Taking both ranges for Auger kinetic energy and core level binding energy into account the presence of metallic indium and an In-O compound can be excluded for Mg K_α measurements. Ranges taken from literature values for In_2Se_3 $CuInSe_2$, and $CuIn_3Se_5$ are also indicated as gray dashed boxes in Figure 4.17b
The same analysis of Auger kinetic and core level binding energy can be done for Se. $CuInSe_2$ has an E_K=1307.30 eV [125] and E_B=53.50 - 55.50 eV [126, 127] and elemental Se E_K=1306.70 - 1307.00 eV [128, 129] and E_B=54.64 - 55.50 eV [121, 130]. Se-O compounds are located at around E_B ∼59 eV which is higher than what we find for core level binding energies (see Table 4.1). These ranges for Se and $CuInSe_2$ are also indicated as gray dashed boxes in Figure 4.17a.

Table 4.1: *The peak position of the respective In and Se core level lines in binding energy (E_B) and the position of the main Auger line in kinetic energy (E_K) measured with Mg K_α and Al K_α. An error margin of ±0.10 eV is assumed.*

sample	E_B(In $3d_{5/2}$)	E_B(Se $3d_{5/2}$)	E_K(In $M_4N_{45}N_{45}$)	E_K(Se $L_3M_{45}M_{45}$)
alkali-free	444.93	54.25	407.60	1306.87
NaF-PDT	444.67	53.96	407.86	1307.27
NaF/KF-PDT	444.66	53.70	407.51	1307.16
KF-PDT In_2Se_3	445.18	54.17	407.01	1306.90

Using the values from Table 4.1 for the respective binding energy of the core levels and the kinetic energy of the Auger lines; α' for Se and In are shown in Figure 4.17. Here, elements with a similar chemical environment have the same modified Auger parameter and are located along diagonal lines within the Wagner-plot (see also chapter 3.2).

The derived modified Auger parameter α' of Se and In is almost identical for alkali-free and NaF-PDT CIGSe, indicating a chemically similar environment, which is in agreement with

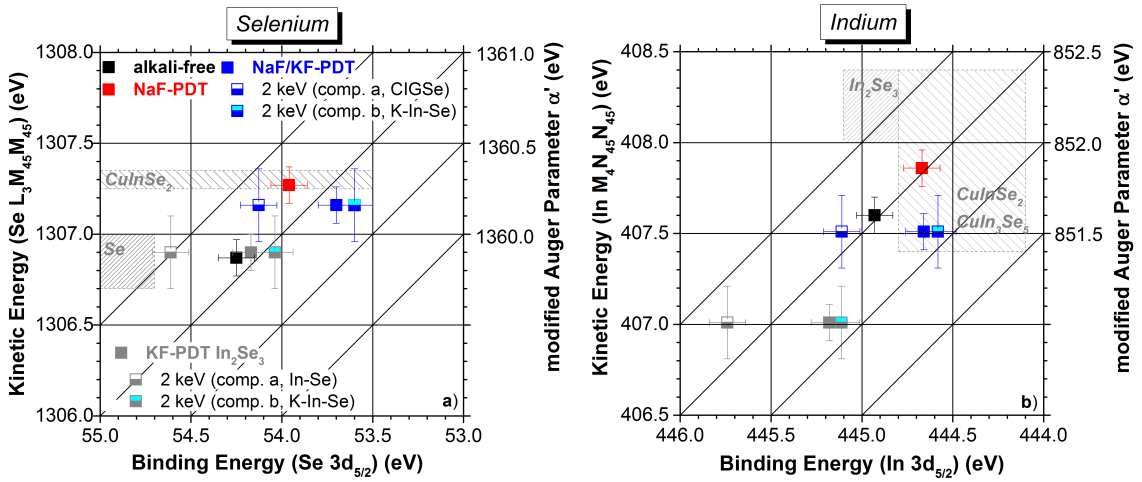

Figure 4.17: *The modified Auger parameters α'=E_B+E_K for selenium a) and indium b) as derived for the alkali-free, NaF-PDT, NaF/KF-PDT CIGSe samples of the alkali-rich absorbers as well as for the KF-PDT In_2Se_3 reference are displayed (filled symbols) in two Wagner-plots with the kinetic energy of the main Auger line vs the binding energy of the respective core level using lab-based Mg K_α and Al K_α. The diagonals represent lines of constant modified Auger parameter α'. The half-filled symbols show the two species (component a (CIGSe) and component b (K-In-Se)) of the NaF/KF-PDT and KF-PDT In_2Se_3 for 2 keV over the Auger kinetic energy derived by XPS. Adapted from [100]*

the previously proposed composition. The K-containing alkali-rich NaF/KF-PDT CIGSe and the KF-PDT In_2Se_3 reference sample deviate in α'(In) from the K-free CIGSe samples and indicate a similar chemical structure for these two, which correlates with the finding of the derived composition. This effect is rather small for Se and the modified Auger parameter α'(Se) suggest similar chemical environments for alkali-free, NaF-PDT CIGSe, and KF-PDT In_2Se_3. The NaF/KF-PDT sample is only slightly lower in the respective α'(Se) and therefore the chemical variation on Se is rather small, as expected for selenium containing samples.[121]

For deriving the modified Auger parameters only laboratory-based XPS data was used with an insufficient resolution to separate the two species, i.e., comp. a (for the underlying CIGSe or In-Se material) and comp. b (representing a K-In-Se type compound) found for NaF/KF-PDT and KF-PDT In_2Se_3. To illustrate the differences in binding energy the 2 keV measurements (similar IMFP to Mg K_α) for Se $3d_{5/2}$ and In $3d_{5/2}$ are used representing comp. a (CIGSe) and comp. b (K-In-Se) (half-open symbols) together with the respective Auger kinetic energy derived for Mg K_α and Al K_α.

Note, the approach using two different excitation energies and thus different energy scales to

gain the "modified Auger parameter" implies that the independence of (surface) band bending, variations in doping concentration, and sample charging are no longer guarantied.
Keeping this in mind, a carefully stated predication can be made, indicating the same chemical environment for α'(In) and α'(Se) for the K-In-Se type compound of NaF/KF-PDT CIGSe and KF-PDT In_2Se_3. The underlying substrate material (i.e., CIGSe for NaF/KF-PDT and In-Se type compound for KF-PDT In_2Se_3) moving to higher binding energies are in agreement with alkali-free, NaF-PDT CIGSe or an In_2Se_3 environment. The differences in α'(In) for the underlying In-Se material to literature values for In_2Se_3 is possibly due to differences in optoelectronic properties, e.g. differences in the position of the valence band maximum depending on the In_2Se_3 thickness.[131]

For CIGSe modified Auger parameters for selenium and indium can be sates as α'(Se)= (1361.20$\pm$0.24) eV and α'(In)=(852.56$\pm$0.24) eV, respectively, and α'(Se)=(1360.85$\pm$0.24) eV as well as α'(In)=(852.13$\pm$0.24) eV for the K-In-Se species.

4.1.2.4 Valence Band Spectra

The chemical changes and the impact of alkali treatments also impact the valence band region. The compositional depth-dependent changes will be discussed in the following.
The valence band spectra (Figure 4.18) show four distinct main peaks (labeled I-IV) which are most clearly seen for the higher resolved 2 keV, 6 keV, and 8 keV measurements. To simplify matters these features are described in terms of the atomic orbitals that make the largest contributions to the hybridized delocalized bands. Table 4.2 lists the attribution of these features based on reported band structures [132, 133] and following the attribution in Ref. [133]. Feature I is ascribed to anti-bonding hybridized Se p – Cu d states, feature II to non-bonding Se p states, III to bonding hybridized Se p – Cu d states, and feature IV to In s / Ga s derived states, respectively. Their respective orbital contribution helps explain the observed dependence of relative intensities on excitation energy in the following.

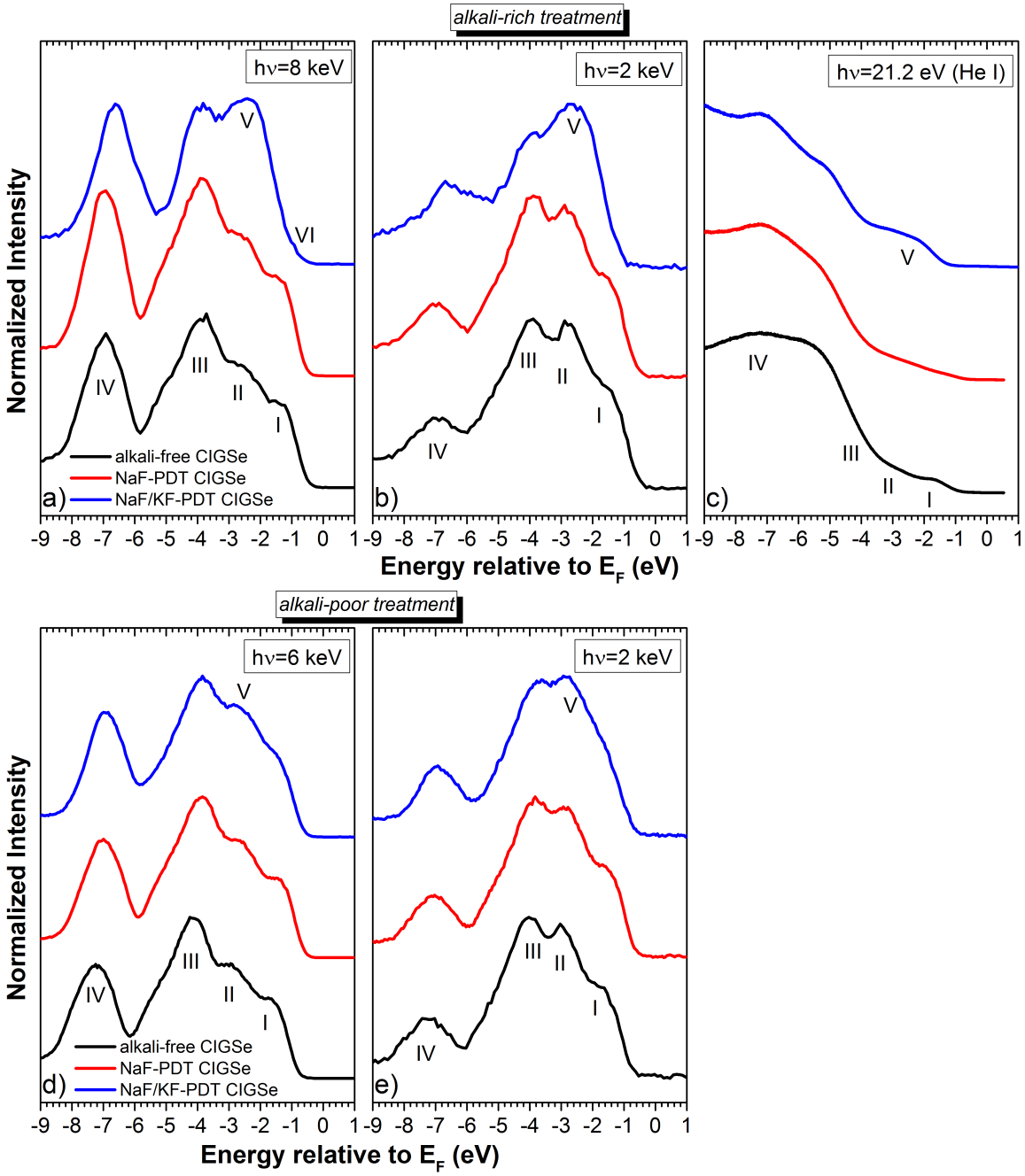

Figure 4.18: *HAXPES derived valence band spectra of the alkali-free (black), NaF-PDT (red), NaF/KF-PDT (blue) of alkali-rich (top) and alkali-poor (bottom) CIGSe absorbers recorded with different excitation energies of hν=8 keV (a), hν=6 keV (d) and hν=2 keV (b,e). Further respective UPS spectra (c, measured with He I [hν=21.22 eV]) are shown for the alkali-rich samples. I-VI indicate the different features in the valence band region. Adapted from [100].*

Table 4.2: *Explanation of the origin for features I-VI in Figure 4.18*

feature	explanation
I	anti-bonding hybridized *Se p – Cu d* states [133]
II	non-bonding *Se p* states [133]
III	bonding hybridized *Se p – Cu d* states [133]
IV	*In s / Ga s* derived states [133]
V	K s derived states
VI	VB onset of buried CIGSe material

For both absorber series (alkali-poor and alkali-rich) the alkali-free and NaF-PDT CIGSe are basically identical for excitation energies of 2 keV and 6/8 keV. In comparison to the alkali-free and NaF-PDT, the NaF/KF-PDT CIGSe shows a notable difference in shape of the valence band spectra around features II which is more pronounced for the alkali-rich treated NaF/KF-PDT. This variation can be associated with the different amount of potassium present at the sample surface of the NaF/KF-PDT CIGSe absorbers. This increase in intensity in the 2-4 eV region is therefore attributed to K s derived states.[80] Due to the diverse chemical environment of potassium in the CIGSe sample (see chapter 4.1.2.2 and 4.1.3.1), especially the second species for the alkali-poor NaF/KF-PDT, we cannot unambiguously describe this as an enhancement of feature II (non-bonding Se p states) and label it as a new feature V.
Further, it is expected that the Na 3s binding energy is approximately 1 eV higher than that of K 4s. [84, 86, 134] The higher intensity in feature III for the alkali-rich NaF-PDT CIGSe in the valence band HAXPES spectra primarily in comparison to the respective NaF/KF-PDT might be due to the differing Na concentration of the samples (see also 4.1.2.2). However, there is no further difference between the alkali-free and alkali-rich NaF-PDT CIGSe and no difference in the alkali-poor CIGSe absorbers. The observed shift in feature IV of the alkali-rich NaF/KF-PDT CIGSe absorbers is due to the strong Ga-depletion at the surface and therefore a change in the density of states ascribed to the In s / Ga s derived states in this region.
The depth-dependet composition (see chapter 4.1.2.2) shows a surface region mainly composed of K, In, and Se (K-In-Se/CIGSe bilayer). Therefore, we attribute the foot in the 8 keV valence band spectrum (feature VI) to the upper valence band of the underlying CIGSe material (i.e., equivalent to the VBM position of NaF-PDT CIGSe, see also Figure 4.24), accessible due to the higher information depth for 8 keV compared to the more surface sensitive 2 keV and UPS measurements.

To properly describe the valence band spectra in Figure 4.18 using different excitation energies resulting in pronounced spectral changes, we also need to consider changes in the chemical and electronic structure, differing background contributions and the energy-dependence of the relative photoionization cross-section. With increasing excitation energy primarily p- and d-derived states (features I-III) get less pronounced than s-derived states (IV), leading to a noticeably more pronounced contribution of IV in the NaF/KF-PDT spectra in Figure 4.18d [84, 86]. If only photoionization cross-section effects are considered (see also chapter 3.6.2) assuming that the composition stays constant within the probed region a similar but smaller intensity increase of IV would be expected with increasing excitation energy for both NaF/KF-PDT CIGSe absorbers. However, from section 4.1.2 and Ref. [4, 101, 135] it is know that the main distribution of potassium is at the surface and near-surface region. This explains the rather constant intensity for feature V in the HAXPES valence band spectra for the alkali-rich NaF/KF-PDT (Figure 4.24 a,b) and the decrease in intensity for 6 keV compared to 2 keV for the alkali-poor NaF/KF-PDT (Figure 4.18 d,e). Furthermore, for the alkali-poor NaF/KF-PDT CIGSe the lower amount of K at the sample surface results in a less pronounced leading edge of the Cu derived states compared to the respective alkali-free and NaF-PDT CIGSe absorber.

Summary

To shortly summarize the results of this section, we used depth-dependent lab- and synchrotron-based photoelectron spectroscopy to study the impact of different alkali treatments on the chemical surface and near-surface structure of CIGSe absorbers. We find that for both absorber sample sets the alkali-free and NaF-PDT CIGSe are similar, revealing a Cu-poor surface. Additionally the derived modified Auger parameter α'(Se) and α'(In) suggests the identical chemical environment for the alkali-free and alkali-rich NaF-PDT CIGSe. No significant difference between the alkali-poor and alkali-rich NaF-PDT and the respective alkali-free CIGSe is found. In contrast, the chemical structure of the alkali-rich NaF/KF-PDT indicates two different species in core level lines and modified Auger parameter. These can be associated with a K-containing (i.e., K-In-Se) compound and a K-free compound (i.e., Cu-In-Ga-Se) with the same Cu-poor structure of the alkali-free and NaF-PDT CIGSe. The observed decrease in K and increase in Cu for more bulk sensitive measurements, a similar composition for the Cu-In-Ga-Se compound to the alkali-free and NaF-PDT, and the two different species for In and Se are in agreement with the possible formation of a K-In-Se/Cu-In-Ga-Se bilayer structure. The same is found for the alkali-poor NaF/KF-PDT CIGSe with a thinner K-In-Se layer.

4.1.3 X-ray Absorption and Emission

This subchapter will focus on x-ray emission and absorption spectroscopy to directly probe the occupied and unoccupied local density of states to provide element-specific information. Using K $L_{2,3}$ XAS and Se $M_{4,5}$ XES the chemical environment specifically of potassium and selenium is examined in an attempt to verify the formation of a K-In-Se-type species.

4.1.3.1 K $L_{2,3}$ XAS

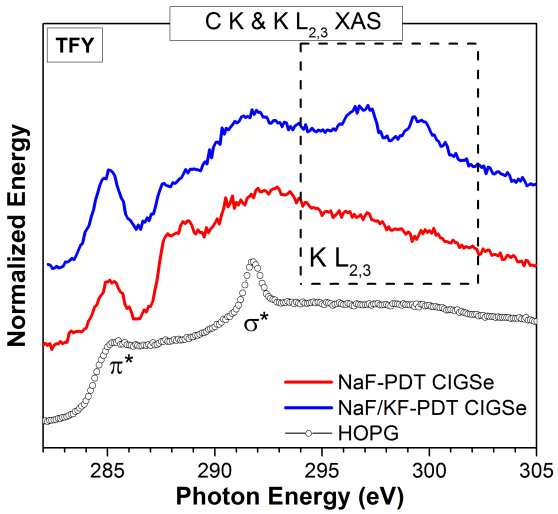

Figure 4.19: *The x-ray absorption spectra of C K and K $L_{2,3}$ edge of the alkali-rich NaF-PDT (red) and NaF/KF-PDT CIGSe (blue) absorbers. As a reference the HOPG (**h**ighly **o**riented **p**yrolytic **g**raphite) sample (black open dots) is shown. Measurements taken in total fluorescence yield (TFY) mode. Vertical offset added.*

The K LMM Auger line sits on top/next to the C KLL Auger line in XAES and thus it is impossible to extract a meaningful modified Auger parameter and consequently no Wagner plot can be drawn, as was done for Se and In in section 4.1.2.3. Hence, the K $L_{2,3}$ absorption edge was used to investigate the chemical environment of potassium.
We carried out C K / K $L_{2,3}$ XAS measurements displayed in Figure 4.19 to also account for the C K background. It can be clearly seen that the nearby C K-edge absorption signal significantly contributes to the background signal of the K $L_{2,3}$ edge. The HOPG (highly oriented pyrolytic graphite) reference spectra was used for energy calibration using the pronounced π^* and σ^* features at 285.4 and 291.7 eV [136] and C K background subtraction.

Comparing it to the alkali-rich NaF/KF-PDT CIGSe no K $L_{2,3}$ absorption edge is detected for the alkali-rich NaF-PDT CIGSe absorber.

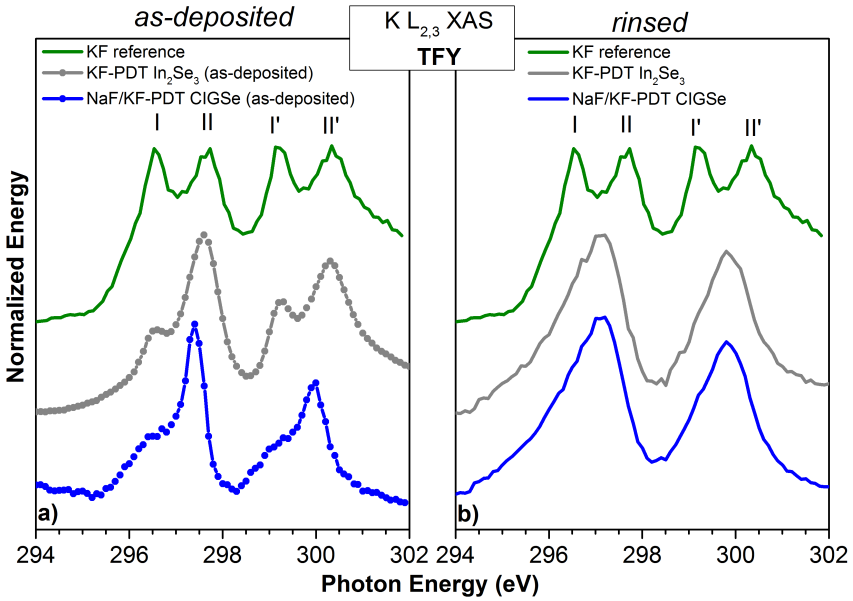

Figure 4.20: *Potassium $L_{2,3}$ x-ray absorption spectra, measured in total fluorescence yield (TFY) mode, of the alkali-rich NaF/KF-PDT CIGSe sample (blue), the KF-PDT In_2Se_3 reference (gray) (as-deposited in a) and rinsed with ammonia or water in b)), and a KF powder-reference (green). The spectra are corrected by the C K background of the HOPG. Vertical offset added. b) adapted from [100].*

Figure 4.20 displays the K $L_{2,3}$ absorption edge of the alkali-rich NaF/KF-PDT CIGSe and the KF-PDT In_2Se_3 as-deposited (i.e., including a NaF and/or KF capping layer) and after ammonia/water rinse together with a KF reference (not rinsed). Both as-deposited samples (see Figure 4.20a) have similar spectral features to the KF reference, with four sharp features, which is found for all potassium halides [137, 138]. The four-peak pattern can be split into two pairs (I, I' and II, II') arising from the splitting between L_2 and L_3 due to the spin orbit splitting of the 2p states. The additional splitting between I and II as well as I' and II' can be ascribed to crystal field effects. [137–139]

In contrast, the alkali-rich NaF/KF-PDT and KF-PDT In_2Se_3 that were subjected to an ammonia or water rinse to remove the remaining alkali fluoride capping layer and to simulate the first step during CdS bath deposition show two very broad features for the K $L_{2,3}$

XAS spectra without the distinct features (I, II, and I', II'). This indicates that the chemical environment of the washed samples is comparable, but significantly different from the as-deposited samples and the KF reference. This is in agreement with Ref. [102], and also with the absence of a fluorine signal in photoemission measurements (see chapter 4.1.2), indicating that little if any unreacted alkali remnants of the PDT are present after the rinsing procedure. Both spectra of the washed alkali-rich NaF/KF-PDT and KF-PDT In_2Se_3 are similar to what is found for K $L_{2,3}$ XAS of K/GaAs [140] and K/Si [141, 142] and therefore it cannot be unambiguously concluded which exact chemical surrounding potassium has for the NaF/KF-PDT and KF-PDT In_2Se_3 sample.
Comparing the as-deposited to their respective rinsed samples lead to the conclusion that the potassium which remains after the rinsing procedure is incorporated into the respective substrate material, or forms a new compound distinct from the KF. This finding is in agreement with the assumptions of Ref. [102] that "potassium remaining on the surface is not present as KF and rather forms a compound or binds at an adsorption site during KF PDT".
Further, the as-deposited KF-PDT In_2Se_3 cannot be represented by a weighted superposition of the KF reference and the washed KF-PDT In_2Se_3.

Note, the alkali-poor NaF/KF-PDT CIGSe absorber and the respective weak potassium signal made it impossible to detect a usable K $L_{2,3}$ XAS signal for this sample.

4.1.3.2 Se $M_{4,5}$ XES

An additional approach to verify the formation of a K-In-Se type species is using Se $M_{4,5}$ XES to directly probe impact of different PDTs on the local density of occupied valence states projected on the Se 3d core level. Here the hybridization of Se-derived valence band electronic states with those of alkali elements is examined and the local electronic structure of Se can be determined.

The Se $M_{4,5}$ XES spectra for alkali-rich treated CIGSe absorbers are displayed in Figure 4.21a together with the KF-PDT In_2Se_3 and an In_2Se_3 (powder) reference sample. Once again the alkali-free and the NaF-PDT CIGSe are identical, which is consistent with the findings for the modified Auger parameter α*(Se) and the compositional depth-profile. Hence, the local electronic structure of Se is the same for these samples. Comparing those with the respective alkali-poor treated samples, the NaF-PDT (alkali-poor) is almost equal to the alkali-rich NaF-PDT and the respective alkali-free CIGSe. However, the alkali-free of the

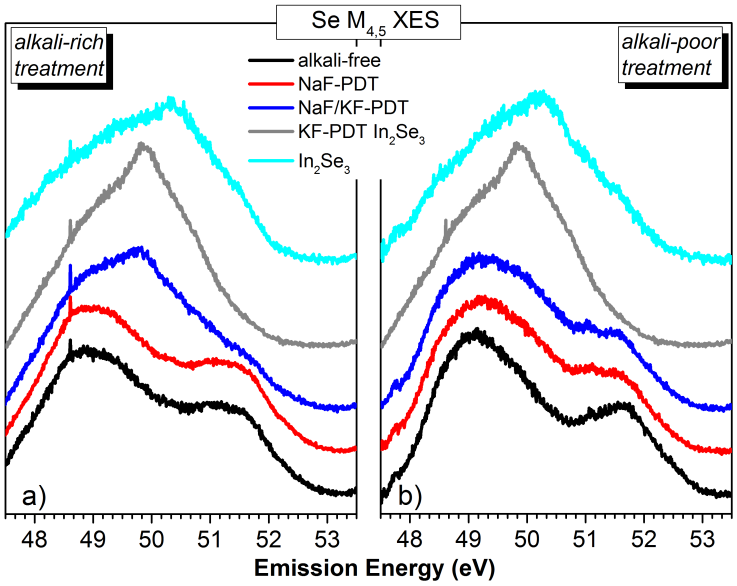

Figure 4.21: *Se $M_{4,5}$ XES spectra of different Cu(In,Ga)Se_2 absorbers subjected to an alkali-rich (a) and alkali-poor (b) treatment are compared to KF-PDT In_2Se_3 and In_2Se_3 (powder) reference samples. Vertical offset added. Panel a) adapted from [100]. Note, the In_2Se_3 was measured twice and used for internal energy calibration of the alkali-poor data, but the KF-PDT In_2Se_3 only once.*

alkali-poor series differs somewhat in shape from the alkali-poor NaF-PDT, the alkali-rich NaF-PDT, and the alkali-free CIGSe absorber by showing a more pronounced minimum between 50-51 eV emission energy with a more distinct and slightly shifted maximum to higher emission energy at around 52 eV. This could be due to the higher oxygen content observed in the near-sruface region (see also chapter 4.1.2.1). Nevertheless the overall shape is for both alkali-free and NaF-PDT CIGSe similar suggesting a comparable chemical environment for selenium.

In contrast the K-containing samples, in that case the alkali-rich NaF/KF-PDT CIGSe and the KF-PDT In_2Se_3, clearly deviate from the potassium free samples, by the presence of an additional emission feature around 50 eV. This feature is not seen in the spectra of the alkali-poor NaF-PDT CIGSe sample, which can be explained by the nominal amount of potassium present for this sample.

For further comparison the spectrum of an In_2Se_3 (powder) reference is also displayed, clearly deviating from all CIGSe samples and the KF-PDT In_2Se_3.

The element-specific density of occupied (PDOS) states from XES is complementary to valence band photoemission information (DOS), and so one can take advantage of known attributions of valence band features to analyze the emission spectra. For this reason an attribution of Se $M_{4,5}$ and the 8 keV photoemission valence band measurements (see also [80] and section 4.1.2.4) of the alkali-rich NaF-PDT and NaF/KF-PDT CIGSe is conducted due to the fact that the alkali-rich NaF-PDT in general represents the remaining CIGSe samples and the alkali-rich NaF/KF-PDT shows a clear impact by adding potassium.

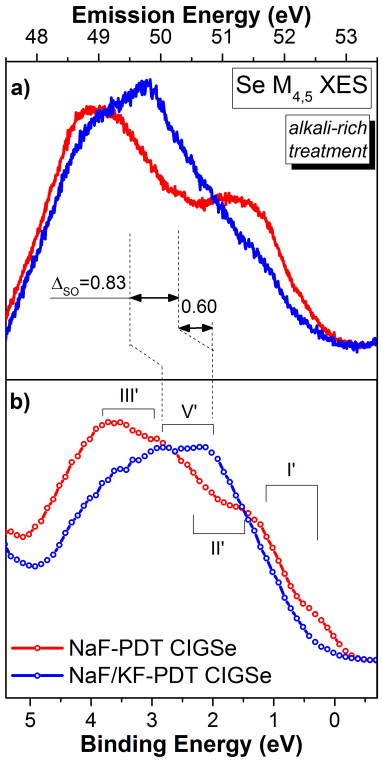

Figure 4.22: *Se $M_{4,5}$ emission of the NaF-PDT and NaF/KF-PDT CIGSe samples (a) compared to HAXPES data of the valence band (VB) region recorded with an excitation energy of 8 keV (b). Note, that the HAXPES data is a superposition of two VB spectra scaled according to the respective area ratio of d-lines and shifted according to the Se 3d doublet separation of 0.83 eV [108] and acts as an "artificial HAXPES-derived XES spectra." Adapted from [100].*

To directly compare the measured XES spectra with HAXPES valence band data an excitation energy of hν=8 keV is chosen. This reuslts in an IMFP of 12.3 nm therefore is in the same range as Se $M_{4,5}$ XES with an effective attenuation length of 12.7 nm [82] (for $CuInSe_2$

and $KInSe_2$) and least affected of surface contamination/oxidation. For further clarification, we use a superposition of two valence band spectra offset by the Se 3d doublet separation of 0.83 eV [108] and scaled with their respective multiplicity of (2j+1) to simulate the Se $M_{4,5}$ XES spectra (for more detail see Appendix A.4). To align the photoemission and x-ray emission data the Se 3d core level binding energy of Se_a at 8 keV for the NaF/KF-PDT CIGSe absorber was used.
Using this approach of comparing occupied valence states, spectral differences can be explained by the influence of different processes during measurements. Variation in intensity arise due to ionization cross-section for photoemission experiments and x-ray emission is influenced by dipole selection rules. Hence, we use the spectral regions to associated them with their particular electronic state. These are indicated (I'-III',V') in Figure 4.22b and follow the annotation of [80] and Figure 4.18 in chapter 4.1.2.4.

Feature I' is depict as a small shoulder on the low binding/high emission energy side. Due to its copper character and therefore low transition probability this feature is almost non-existing in the element specific Se $M_{4,5}$ XES and located at around 52.5 eV emission energy. The spectral region of feature II' can be ascribed to non-bonding Se p states [133] and feature III' to bonding hybridized Se p- Cu d-states [133]. The additional feature V' at $E_B \sim 3$ eV is only present for the alkali-rich NaF/KF-PDT CIGSe absorber and is attributed to K 4s derived states. [80] This feature can be assigned to the additional K-related peak in Se $M_{4,5}$ XES at approximately 50 eV emission energy and is the most significant difference to the K-free absorbers. It is shifted by 0.6 eV (indicated in Figure 4.22) downward in emission energy due to a shift in binding energy of comp. b (K-In-Se type species, see 4.1.2.2) to lower energies in comparison to comp. a (CIGSe species). The presence of this additional feature in K-containing samples indicates the hybridization of K and Se states and therefore proves the formation of K-Se bonds confirming the incorporation of K into the respective substrate material (i.e., CIGSe and/or In-Se) or forming a new compound. This finding is again in agreement with the assumptions of Ref. [102] of "the formation of a material containing K, In, and Se". Also it confirms the findings for $Cu_{1-x}K_xInSe_2$ alloys [113], and the suggestions for co-evaporated $KInSe_2$ on top of CIGSe [143].

The presence of this feature in the alkali-poor NaF/KF-PDT CIGSe in comparison to the respective NaF-PDT seems at first sight non-existing, see direct comparison in Figure 4.23. The shape of Se $M_{4,5}$ spectrum of the alkali-rich NaF/KF-PDT, however, indicates that it can

be represented by a spectral sum of the alkali-rich NaF-PDT and the KF-PDT In_2Se_3.

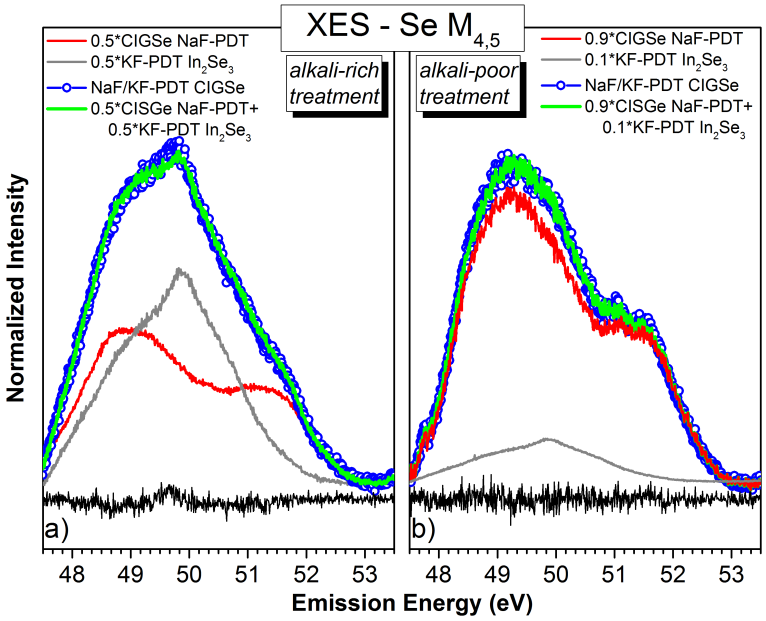

Figure 4.23: *The Se $M_{4,5}$ XES spectrum of the alkali-rich NaF/KF-PDT CIGSe absorber is represented by a spectral sum of [0.5 · alkali-rich NaF-PDT CIGSe + 0.5 · KF-PDT In_2Se_3] (dotted green) in a). The Se $M_{4,5}$ XES spectrum of the alkali-poor NaF/KF-PDT CIGSe absorber is represented by a spectral sum of [0.9 · alkali-poor NaF-PDT CIGSe + 0.1 · KF-PDT In_2Se_3] (dotted green) in b). The difference between data and sum (residual) is also shown. Panel a) adapted from [100].*

Figure 4.23a shows the weighted sum of alkali-rich (0.5 · NaF-PDT CIGSe + 0.5 · KF-PDT In_2Se_3) exactly representing the alkali-rich NaF/KF-PDT CIGSe. This is another indication and supporting the formation of a K-In-Se type species. The same approach can be done for the alkali-poor NaF/KF-PDT to examine the formation of possible K-Se bonds also in this case. Figure 4.23b) shows the spectral sum of (0.9 · NaF-PDT CIGSe + 0.1 · KF-PDT In_2Se_3) to model the Se $M_{4,5}$ spectrum of the alkali-poor NaF/KF-PDT CIGSe. It can be clearly seen that the impact of potassium and the hybridization of K and Se is less pronounced than for the alkali-rich NaF/KF-PDT sample. This can be due to the thinner (nanopatterned) surface layer. However, similar to the findings for the alkali-rich NaF/KF-PDT absorber we conclude that also in this case a K-In-Se type surface compound is formed. If we assume for both systems a perfectly smooth bilayer structure of K-In-Se/CIGSe we can roughly estimate a relative thickness for the K-containing layer using equation 3.8. The weighted sum together with an attenuation length of 12.7 nm for Se $M_{4,5}$ emission a layer

thickness of approximately 8.8 nm for the alkali-rich NaF/KF-PDT and 1.3 nm for the alkali-poor NaF/KF-PDT can be derived. This is in good agreement with the findings of the depth-dependent valence band measurements of the shallow core levels. Here we clearly detect a notable amount of the underlying CIGSe material for an excitation energy of hν=8 keV with an IMFP of maximum 12.3 nm.

Summary

To conclude this section, we could experimentally confirm with K $L_{2,3}$ XAS that, after rinsing with ammonia/water, no KF remnants are present and that NaF/KF-PDT and KF-PDT In_2Se_3 have K present in the same chemical environment, that significantly differs from KF. This suggest that K is incorporated into the CIGSe/In-Se substrate and/or forms a new fluorine free compound.

Using Se $M_{4,5}$ XES the local density of occupied states was examined showing the identical Se structure for alkali-free and alkali-rich NaF-PDT and similar to what is found for the respective alkali-poor CIGSe absorbers. The alkali-rich NaF/KF-PDT and the KF-PDT In_2Se_3 exhibit an additional feature ascribed to K 4s derived states indicating the formation of K-Se bonds. This feature is much smaller for alkali-poor NaF/KF-PDT, but it can also be identified by a superposition of properly weighted NaF-PDT and KF-PDT In_2Se_3 Se $M_{4,5}$ XES spectra. The corresponding chalcopyrite spectra and the KF-PDT In_2Se_3 reference sample also clearly deviate from an In_2Se_3 (powder) reference. This is another confirmation for the formation of a K-In-Se type species (rather than a simpler Cu- and Ga-depletion) which can be "tuned" by a different degree of alkali PDT.

4.2 Impact of Alkali Treatments on the Electronic Structure

This section focuses on the influence of different alkali treatments (i.e., NaF and/or KF) on the electronic structure of CIGSe absorbers in comparison to the respective alkali-free (i.e., untreated) CIGSe absorber. Especially, how the changes in the chemical structure based on the NaF- and NaF/KF-PDT and the formation of a K-In-Se-type surface species will influence the electronic structure will be revealed. Photoelectron spectroscopy with different excitation energies (He I (hν=21.22 eV), 2 keV, 6 keV, and 8 keV) was used resulting in a variation in inelastic mean free path (IMFP) from 0.6, 4.0, 9.7, to 12.3 nm [78, 79]. This allows to get a depth-dependent picture of the valence band (VB) structure and the position

of the valence band maximum (VBM). To directly determine the complementary conduction band minimum (CBM) inverse photoelectron spectroscopy (IPES) was used.

In chapter 4.1 on the chemical structure, we observed that both NaF/KF-PDT absorbers exhibit a Cu- and Ga-depleted surface region with a depletion extent depending on the respective treatment (i.e., alkali-poor or alkali-rich) in comparison to the respective alkali-free and NaF-PDT CIGSe absorbers. The difference in PDT also reflects on the amount of potassium found at the absorber surface forming a K-In-Se-type species. The chemical structures for both alkali-free and NaF-PDT CIGSe absorbers are similar.

The valence band photoemission of the alkali-rich and alkali-poor absorbers are displayed in Figure 4.24 with varying the excitation energy from 21.22 eV up to 8 keV. Excitation energies of 8 keV and 6 keV (Figure 4.24a) with an IMFP of <12 nm and <10 nm were used to probe the near-surface. Using excitation energies of 2 keV leads to an IMFP of <4 nm (Figure 4.24b and e). With an IMFP of 0.6 nm [78] the UPS spectra of the alkali-rich CIGSe absorbers (Figure 4.24c) (hν=21.22 eV, He I) are the most surface sensitive.

As already explained in section 4.1.2.4 to properly describe the valence band spectra in Figure 4.24 using different excitation energies resulting in pronounced spectral changes, we also need to consider changes in the chemical and electronic structure, differing background contributions and the energy-dependence of the relative photoionization cross-section. In addition, the different degree of surface contamination (for detailed explanation see chapter 4.1.2.1) may also affect the spectral shape, especially for the surface sensitive UPS measurements. This may be the reason for the less pronounced leading edge in the UPS (He I) valence band spectra of the alkali-rich NaF-PDT CIGSe in comparison to the alkali-free and NaF/KF-PDT CIGSe. This will be considered with an increased error margin of the determined VBM value.

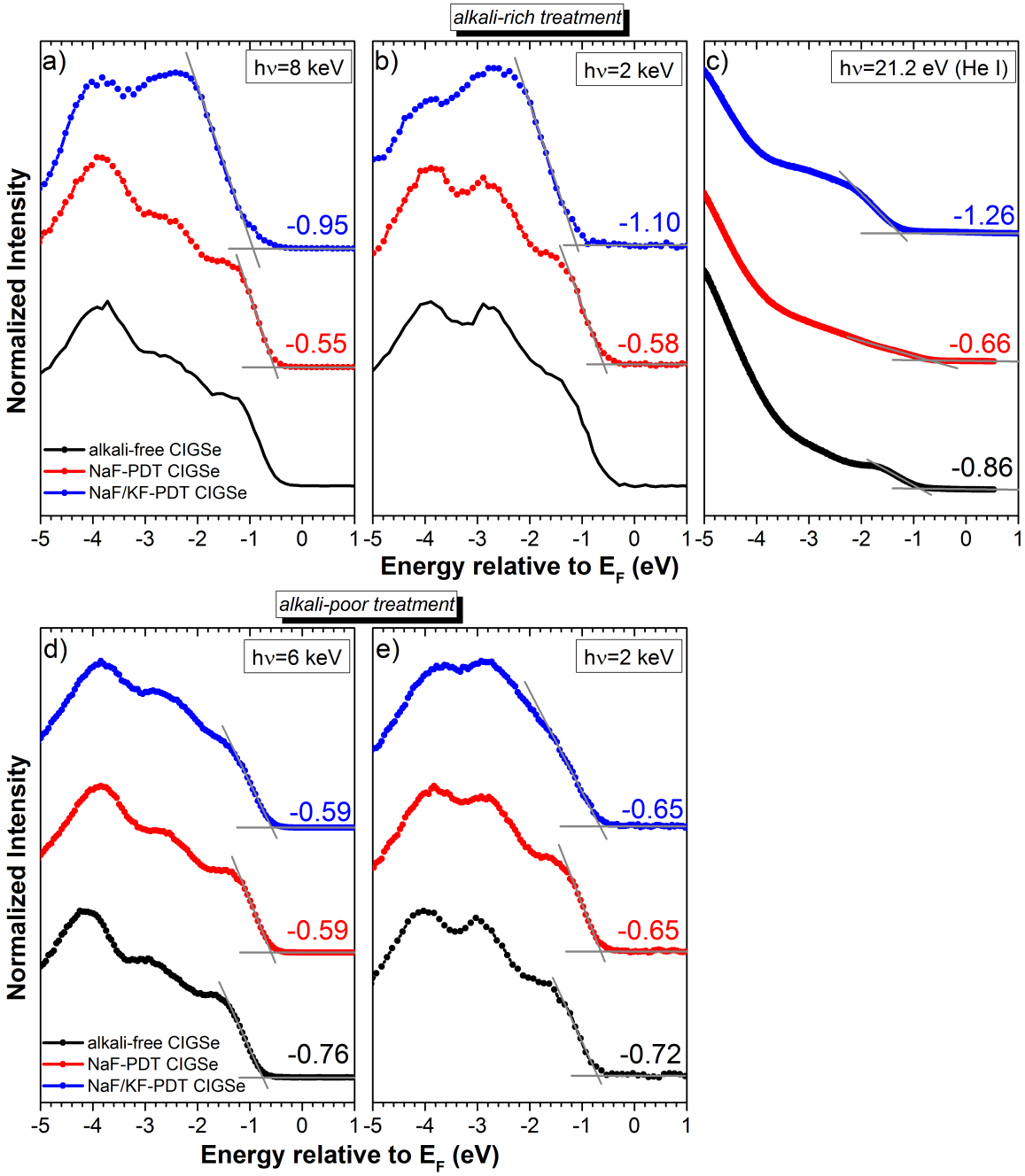

Figure 4.24: *HAXPES derived valence band spectra of the alkali-free (black), NaF-PDT (red), NaF/KF-PDT (blue) of alkali-rich (top) and alkali-poor (bottom) CIGSe absorbers recorded with different excitation energies of hν=8 keV (a), hν=6 keV (d) and hν=2 keV (b,e). UPS spectra (c) are measured with He I (hν=21.22 eV). Linear approximation of the leading edges is used to determine the position of the valence band maxima. Note, due to Zn contamination no VBM is derived for the alkali-free absorber of the alkali-rich series for 2 keV and 8 keV. Adapted from [80].*

To derive the respective values for the VBM for all valence band spectra in Figure 4.24, a linear extrapolation of the leading edge is used (see also chapter 3.6). For the alkali-free CIGSe absorbers of the alkali-rich treated samples the VBM value is -0.86 ($\pm$0.1) eV for the 21.22 eV excited spectra. Due to Zn contamination no VBM is derived for 2 keV and 8 keV. However, due to the almost exact spectral similarity (see Appendix A.5) it seems legitimate to employ the derived VBM values of the alkali-free sample from the alkali-poor series. Therefore, we depict the VBM value for the alkali-free CIGSe to be at -0.76 ($\pm$0.15) eV for 8 keV and -0.72 ($\pm$0.15) eV for 2 keV. For the alkali-rich NaF-PDT CIGSe VBM values are -0.55, -0.58 ($\pm$ 0.10) for 8 keV, 2 keV, and 21.22 eV, and -0.66 $+0.10/-0.15$) eV and for the alkali-rich NaF/KF-PDT, they are -0.95, -1.10, and -1.26 ($\pm$ 0.10) eV, respectively. The VBM values for the alkali-poor absorbers are -0.76, -0.72 ($\pm$0.1) eV for the alkali-free CIGSe, and -0.56, -0.65 ($\pm$0.1) eV for NaF-PDT and NaF/KF-PDT CIGSe for 6 keV and 2 keV, respectively. All is schematically displayed in Figure 4.26. In general, for all CIGSe absorbers the obtained values for the VBM shifts away from the Fermi level (E_F) with decreasing excitation energy.

The alkali-free CIGSe exhibits a small excitation energy-dependent downward shift of (-0.10 [$\pm$0.21] eV) towards the surface, and a similar shift of (-0.11 [$+0.14/-0.21$] eV) can be seen for the alkali-rich NaF-PDT CIGSe. The alkali-rich NaF/KF-PDT CIGSe reveals a larger shift of (-0.31 [$\pm$0.14] eV).
Such VBM shifts can be explained by a downward surface band bending or by a widened band gap at the surface. The depth-dependet composition (see chapter 4.1.2.2) shows a surface region mainly composed of K, In, and Se (K-In-Se/CIGSe bilayer), thus we attribute the observed VBM shift of the alkali-rich NaF/KF-PDT CIGSe sample mainly to a depth-dependent chemical and electronic structure change in the surface region. The smaller shift of (-0.10 [$\pm$0.21] eV) for the alkali-free and (-0.11 [$+0.14/-0.21$] eV) for the alkali-rich NaF-PDT CIGSe may be explained with possible structure changes. Here, reported shifts in the VBM spectra of in-situ grown $CuInSe_2$ and $CuIn_3Se_5$ are approximately 0.0 and -0.2 ($\pm$0.1) eV. [144] For the studied samples we also observe a minor depth-dependent change in composition (see chapter 4.1.2.2).
Note, such surface-related shifts cannot be stated for the alkali-poor absorbers due to the missing UPS measurements. However, one would except similar VBM values for the alkali-free and NaF-PDT CIGSe as found for the respective alkali-rich absorbers. For NaF/KF-PDT a surface VBM value is expected in the range of the alkali-rich NaF-PDT.

Comparing the derived UPS VBM values of the alkali-rich NaF/KF-PDT CIGSe sample to the respective alkali-free and NaF-PDT CIGSe results in shifts of (-0.40 [±0.14] eV) and (-0.60 [+0.14/−0.18] eV). This is also in agreement with a VBM shift of -0.3 to -0.4 eV between an untreated absorber (deposited on Mo-coated soda lime glass) and a KF UHV heat treated absorber (not a NaF/KF-PDT under the presence of Se) reported in a previous study by Pistor et al. [42].
The VBM shift closer to the Fermi level (E_F) for the NaF-PDT compared to the respective alkali-free sample is due to Na incorporation and the changes in doping concentration. It is known that Na makes the absorber material more p-type.[145]

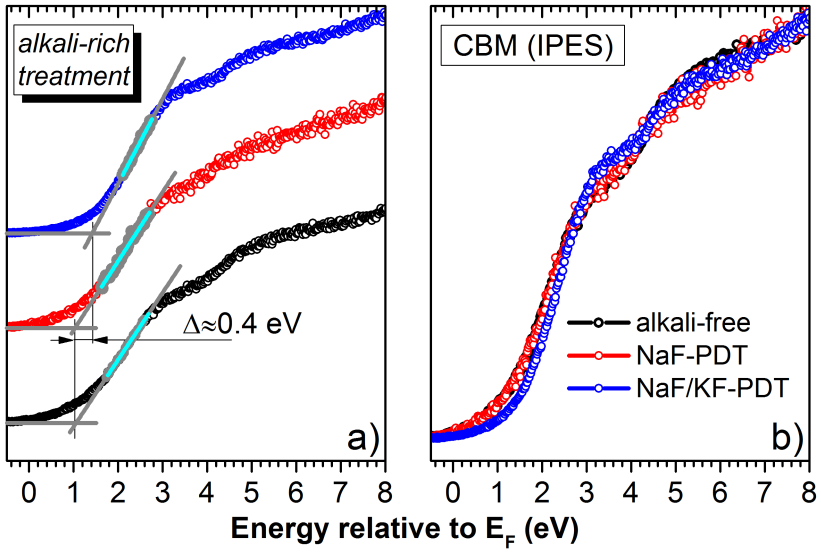

Figure 4.25: *(a) IPES spectra with linear approximation of the leading edges (highlighted in green and gray) are used to determine the CBM. (b) IPES spectra plotted over each other to highlight the shift of the NaF/KF-PDT CIGSe CBM. Adapted from [80].*

IPES is used to probe the unoccupied conduction band states of the alkali-rich CIGSe absorbers (Figure 4.25). All three curves are very similar. The curves for the alkali-free and NaF-PDT CIGSe absorber are basically identical when plotted on top of each other (Figure 4.25b) and reveal a noticeable change in spectral shape compared to the NaF/KF-PDT CIGSe. This affects the derived CBM value (Figure 4.25a) obtained from linear extrapolation of the leading edge. Due to the lower experimental resolution of the IPES setup (see also chapter 3.7.1) and the presence of a large tail an asymmetric error margin of (+0.10/−0.50 eV) is assigned reflecting the experimental uncertainty. For linear extrapolation the region with a clearly linear shape is used and highlighted in Figure 4.25a. The hereby derived CBM values are 1.03 (+0.10/−0.50) eV for the alkali-free and NaF-PDT

CIGSe and 1.42 (+0.10/−0.50) eV for the NaF/KF-PDT CIGSe, respectively. Considering the asymmetric error margin those values can be seen as upper bounds of the CBM. The relative shift between the NaF/KF-PDT and the alkali-free and NaF-PDT CIGSe of +0.40(±0.10) eV is less prone to experimental uncertainty.

The derived values for the VBM and the CBM by UPS/HAXPES and IPES are associated in Figure 4.26 as a function of the corresponding photoelectron IMFP. For both sample sets, i.e., alkali-rich and alkali-poor, a depth-dependent shift for the VBM values is observed.
The electronic surface band gap is derived using the VBM values of the 2 keV HAXPES measurements and the CBM determined from IPES due to similar IMFPs (see also chapter 3.6). For the alkali-free CIGSe the determined electronic surface band gap is 1.77 (+0.18/−0.52) eV and for the NaF-PDT CIGSe 1.61 (+0.14/−0.51) eV of the alkali-rich absorbers. Both values found for the alkali-rich absorbers are larger than the lowest band gap found for the bulk by quantum efficiency measurements of around 1.15 eV [4]. The computed band gap value [26] of approximately 1.22 eV considering the Ga-grading towards the surface with a maximum Ga:(Ga+In) surface composition of 0.36 [28, 146] (excluding Cu-deficiency effects), is still lower than the derived band gap from HAXPES/IPES measurements. Such band gap widening at the surface has been observed for high-efficiency chalcopyrite absorbers.[30, 114] This effect has been related to a decrease in p-d interband repulsion caused by a Cu-deficient surface composition [147] associated with phase formation [144] or reconstruction [148, 149]. Note, that the lower error margin of the electronic surface band gaps for the alkali-free and alkali-rich NaF-PDT CIGSe is in the range of the observed bulk band gaps. Nevertheless, similar surface band gaps are observed for other high-performing CIGSe absorbers.[26]
An electronic surface band gap of 2.52 (+0.14/−0.51) eV is derived for the alkali-rich NaF/KF-PDT. It is considerablly larger than the corresponding values for the alkali-free and NaF-PDT CIGSe and bulk band gap of about 1.22 eV, that includes the Ga-gradient [4, 28, 102].
Note, no near-surface electronic band gaps can be determined for the alkali-poor series because of missing IPES measurements. However, for the alkali-free and the respective alkali-poor NaF-PDT similar band gap values as determined for the alkali-rich absorbers are expected. It can be speculated that the CBM value for the alkali-poor NaF/KF-PDT might more likely be in the range of the alkali-rich NaF-PDT CIGSe instead of the alkali-rich NaF/KF-PDT CIGSe. This speculation is based on the findings found for the chemical structure of the alkali-poor sample set compared to the alkali-rich samples (see also chapter 4.1).

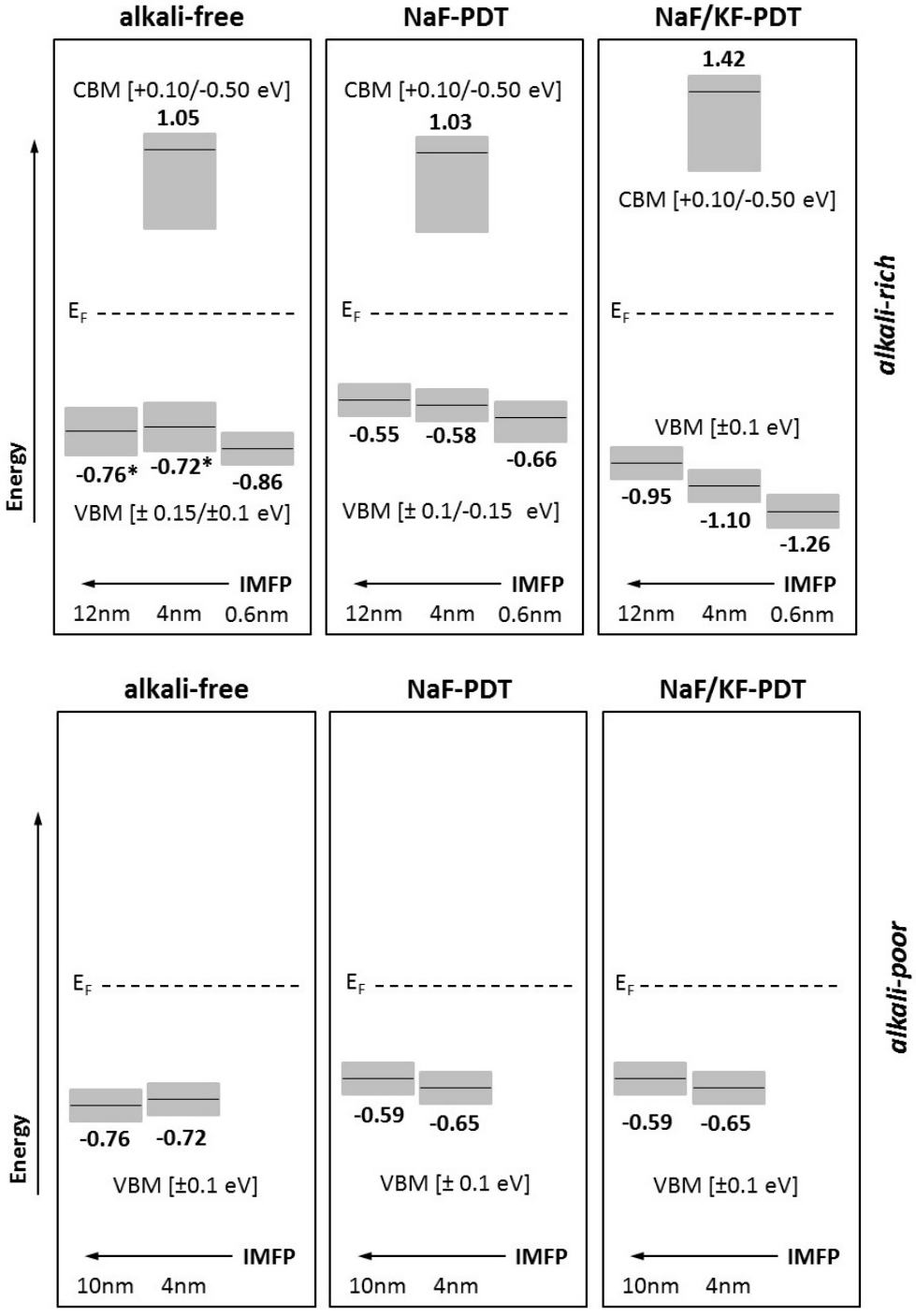

Figure 4.26: *Schematic of the energy band positions for alkali-free, NaF-PDT, and NaF/KF-PDT CIGSe for alkali-rich (top) and alkali-poor (bottom) thin film solar cell absorbers with respect to the Fermi level E_F, determined using direct and inverse photoemission measurements having different IMFP. The gray boxes indicate the experimental uncertainty. The $(*)$ indicates the adapted VBM values due to Zn-contamination for the alkali-free CIGSe absorber. Adapted from [80].*

As already described in chapter 4.1.2.2 and for example [100, 102] the surface of the alkali-rich NaF/KF-PDT is mainly composed of K, In, and Se forming a K-In-Se/CIGSe bilayer structure. Therefore, the near surface region is more appropriately compared to the electronic structure of compounds such as In_2Se_3 and $KInSe_2$. For In_2Se_3 a pronounced thickness dependence of the band gap has been observed, with band gap values exceeding 2.5 eV for 2.6 μm.[131] For $KInSe_2$ band gap values of 2.7 eV [150, 151] are reported. Both values are in good agreement with the surface band gap determined for the alkali-rich NaF/KF-PDT CIGSe absorber.

Together with the findings of chapter 4.1.2, the electronic surface and near-surface structure indicated in Figure 4.26 shows significant valence and conduction band offsets. The photogenerated charge carriers (i.e., electrons and holes) are collected at the front and back contact, respectively, of the solar cell device and mostly generated in the absorber bulk. Therefore electrons have to pass through the interface between bulk and surface region to reach the front contact where such a valence band offset (VBO) would disable hole transport or possibly accelerate them to the back contact. Additionally in general a positive conduction band offset (CBO) would block electron transport across the interface. However, previous work suggest the positive effect of CB discontinuities at the buffer/absorber interface with positive CBO (i.e., spike-like, see also chapter 3.6) of +0.3 [152, 153] and 0.4 eV [154] without negatively influencing the efficiency.

Also buffer deposition may change the electronic structure of the bulk/surface interface of the CIGSe absorber.[155, 156] Maybe VBOs and CBOs as seen for the alkali-rich NaF/KF-PDT with a significant band gap widening towards the surface can have a positive impact on device performance by acting as a chemical passivation layer. This is known from silicon-heterojunction solar cells [157] and in agreement with a reduced interface recombination rate observed for similar NaF/KF-PDT CIGSe absorbers. [158]
Furthermore the NaF/KF-PDT CIGSe absorbers show a certain degree of nanopatterning at the absorber surface as seen in chapter 4.1.1 and in Ref. [101] that may impact the electronic structure. As the VBM (CBM) are dominated by the material possessing the occupied (unoccupied) density of states in the region of E_F, the presence of a band gap widened K-In-Se (i.e., Cu- and Ga-depleted) surface region blocking holes and electrons would not be negated in case of a non-continuous surface layer on top of the CIGSe material as seen for the studied NaF/KF-PDT CIGSe absorbers. Especially for the alkali-rich NaF/KF-PDT CIGSe the extend of nanopatterning with domain size and surface region thickness needs to be considered

in further discussing the findings. The layer thickness of this nanopatterned region, which may act as a passivation layer, and the distinct patterning in domain size resulting in geometrical features as in Ref. [101] can act as point openings in the surface layer. Such "point contacts" may even explain the beneficial effect of the alkali-rich NaF/KF-PDT treatment on the open circuit voltage and fill factor (see also Table 2.1 in chapter 2.1.2) of corresponding CIGSe devices which is in agreement with simulation results in Ref. [101]. In the case of a thin surface region and/or only loosely distributed domains (i.e., the nanopatterning is [almost] nonexistent as reported in Ref. [159]), then the downward shift of the VBM that is reported to be more pronounced for alkali-rich NaF/KF-PDT CIGSe (compared to alkali-rich NaF-PDT CIGSe) [80] could explain the improved performance by an increased charge selectivity more efficiently repelling holes from the emitter/absorber contact. These considerations are certainly only relevant considering that the extent of surface nanopatterning itself does not have an impact on the properties of the surface layer as seen in chapter 4.1.

Summary

In summary, we have used direct and inverse photoemission to study the electronic structure (i.e., the position of VBM and CBM) of high-efficient CIGSe thin film solar cell absorbers subjected to different alkali post-deposition treatments (i.e., alkali-rich and alkali-poor). For the alkali-rich treated CIGSe absorbers we find VBM values of -0.76, -0.72 ($\pm$0.15) eV, and 0.86 ($\pm$0.10) eV for the alkali-free CIGSe and -0.55, -0.58 ($\pm$0.10) eV, and -0.66 ($+0.10/-0.15$) eV for NaF-PDT CIGSe with increasing surface sensitivity. For the respective alkali-poor absorbers we observe VBM values of -0.76, -0.72 ($\pm$0.10) eV for alkali-free CIGSe and -0.59, -0.65 ($\pm$0.10) eV for NaF-PDT and NaF/KF-PDT CIGSe. A large and more gradual change in the VBM of the alkali-rich NaF/KF-PDT CIGSe sample is observed with bulk values of -0.95, -1.10, and -1.26 ($\pm$0.10) eV for the surface. Together with the CBM provided with IPES measurements the near-surface electronic band gap value is obtained. For the alkali-rich NaF-PDT CIGSe a band gap of (1.61 [$+0.14/-0.51$] eV) at the surface is observed which is larger than the observed bulk value of 1.15 eV. The shift in VBM for the NaF-PDT sample compared to the alkali-free sample is due to Na incorporation resulting in a more p-type material. A significant band gap widening at the surface of (2.25 [$+0.14/-0.51$] eV) for the alkali-rich NaF/KF-PDT CIGSe is attributed to the formation of a heavily Cu- and Ga-depleted near-surface region which is mainly composed of K, In, and Se. This value is therefore compared to band gap values for In_2Se_3 and $KInSe_2$ compounds. The alkali-rich NaF/KF-PDT induced band gap widening at the CIGSe surface forming a beneficial passivation layer between emitter and absorber might be the reason for the ob-

served performance leap of respective solar cell devices and the difference in performance between the alkali-poor and alkali-rich NaF/KF-PDT CIGSe.[80]

5

Characterization of Compound and Interface Formation of Mixed-halide Perovskite Absorbers

This chapter focuses on the characterization of organo-metal mixed halide perovskites, specifically $CH_3NH_3PbI_{(3-x)}Cl_x$. In the last few years organo-metal mixed halide perovskite solar cells have shown their huge potential, already reaching power conversion efficiencies comparable to polycrystalline chalcopyrite and even silicon solar cells. However, the fundamental properties regarding the material composition, electronic structures, and role of chlorine are not yet understood.
In the first part, the compound formation, which was monitored during in-situ annealing and the presence of chlorine will be discussed. Second, the chemical and electronic properties of the interface between perovskite and the most common electron transport materials mesoporous and compact TiO_2 is explored. SEM and EDX are used to explain the topography and to map the elemental distribution, complementing the spectroscopy analysis.

5.1 Compound Formation (in-situ annealing)

This section focuses on the study of compound formation during in-situ annealing from precursor solution to the final perovskite absorber layer. To study the crystallization behavior we monitored the process during in-situ annealing using photoelectron spectroscopy with an excitation energy of hν=2 keV.

5.1.1 Sample Preparation and Handling

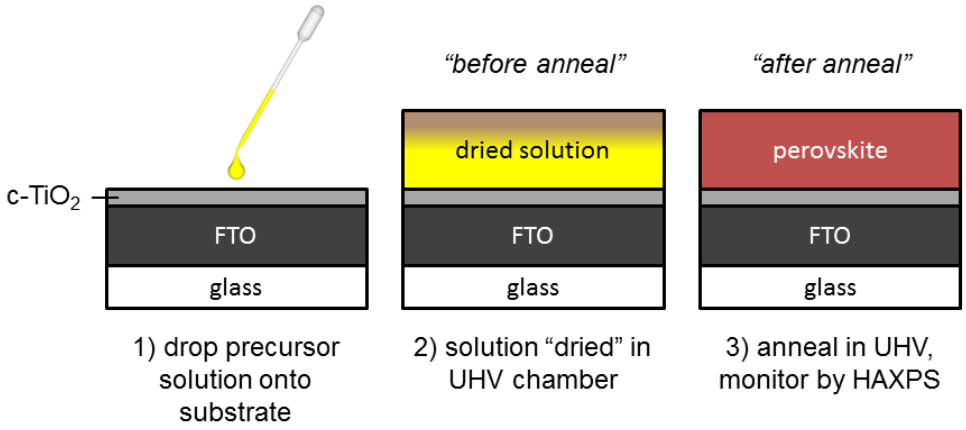

Figure 5.1: *Schematics of the sample preparation. The precursor solution is drop-casted onto compact TiO_2 (c-TiO_2) on FTO/glass. The solution was dried in the UHV-chamber followed by in-situ annealing monitoring perovskite formation with HAXPES.*

For this experiment the sample has been prepared according to the following procedure:
As substrate material a compact TiO_2 sample was used prepared for us by the Department of Chemistry at Uppsala University according to [160]. Briefly, the TiO_2 film was prepared on a pre-cleaned FTO/glass substrate by spray pyrolysis in air using 0.2 mol/l Ti-isopropoxide and 2 mol/l acetylaceton in isopropanol on a hot plate at 500°C. The resulting TiO_2 film is about 100 nm thick. The substrate was heated to 150°C for 10 min. prior to perovskite deposition to remove possible water residues from handling and storage of the substrate in air.
The precursor solution was prepared according to Ref. [9, 13]. The CH_3NH_3I (MAI) was prepared in-house as described in chapter 2.2.2.2. For this experiment, we dissolved about

0.81 g MAI with 0.47 g commercially available $PbCl_2$ in 4 ml DMF and stirred it for 4-5 h.

Figure 5.1 displays the samples studied in this experiment. In a first step the solution was drop-casted onto the c-TiO_2 substrate mounted on the respective sample holder before immediate (less than 3 min, i.e., time after drop-casting) introduction in the UHV-system of the HiKE endstation at the KMC-1 beamline at BESSY II. The chamber was pumped down reaching a pressure of $3 \cdot 10^{-8}$ mbar in approximately an hour. The sample color changed from the yellow solution to a brownish film in the drying process.
Prior to in-situ annealing the sample was measured as introduced at room temperature (RT) for about 4h. In a next step the sample was slowly in-situ annealed from RT to approximately 150°C while monitoring chosen core levels and the shallow core levels of the extended valence band. During annealing the sample color changed to brown. After in-situ annealing the sample (brown colored) was measured in more detail again.

5.1.2 Results

This section compares in detail the compound formation of perovskite during annealing and elucidates the results before and after annealing the sample.

As already explained, measurements were done before and after the annealing step. The survey spectra recorded with an excitation energy of hν=2 keV are shown in Figure 5.2. The maximal IMPF reached for shallow core levels is approximetly 3.5 nm [79] assuming the material to be represented by a $PbCl_2$. Both survey spectra show the most prominent perovskite related core level and Auger lines for lead and iodine and additionally Ti lines from the substrate. Further, for both spectra C 1s and O 1s can be detected which can be assigned to carbon in the $CH_3NH_3PbI_{(3-x)}Cl_x$ framework and oxygen from the TiO_2 substrates as well as surface contamination due to short sample handling in air.
Moreover, for the measurements taken before the annealing step, in addition to Pb, I, and N, chlorine is present. This already indicates that the composition of the sample property changed during annealing.

Figure 5.3 shows the Ti 2p, N 1s, Cl 2p, and Pb 4f core levels and the VBM taken with a photon energy of hν=2 keV before and after annealing. Figure 5.3a shows the Ti 2p core level revealing no shift in binding energy position before and after annealing. However, the

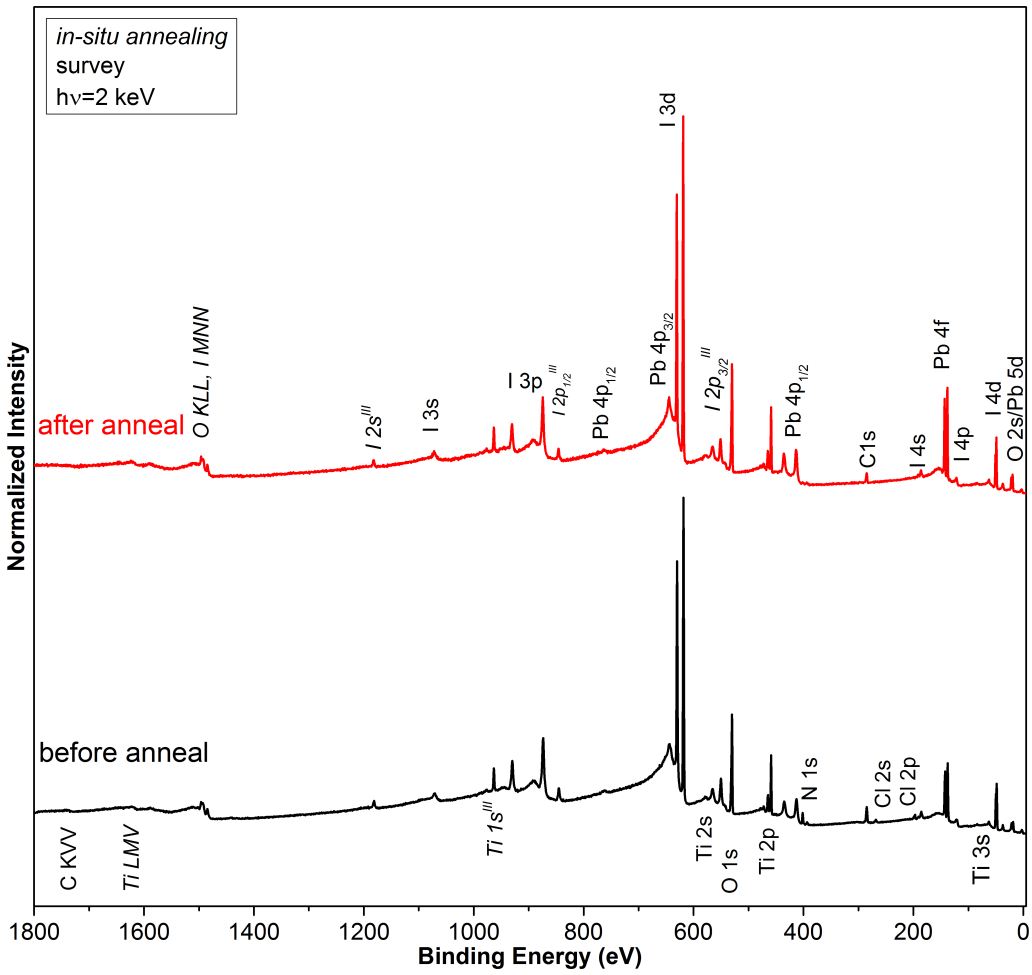

Figure 5.2: *Survey spectra of the $CH_3NH_3PbI_{(3-x)}Cl_x$ sample before (black) and after (red) in-situ annealing measured with an excitation energy of hν=2 keV. The core level and Auger lines are labeled. Vertical offset added for clarity.*

signal intensity for the sample after annealing is slightly higher, indicating structural and/or morphological changes due to the annealing step. This is in agreement with previous findings confirming holes in the final perovskite layer.[13] So it is likely that the drop-casted precursor film is also not fully covering the entire c-TiO_2 substrate.

Figure 5.3b shows the N 1s line with a decrease in signal intensity after annealing. This decrease can be explained with nitrogen leaving the sample in form of gaseous N_2 and in the form of $CH_3NH_3^+$ or CH_3NH_3Cl.[54, 161]

The Cl 2p core level line is displayed in Figure 5.3c showing a significant difference between the drop-casted solution on c-TiO_2 before annealing and the perovskite sample after

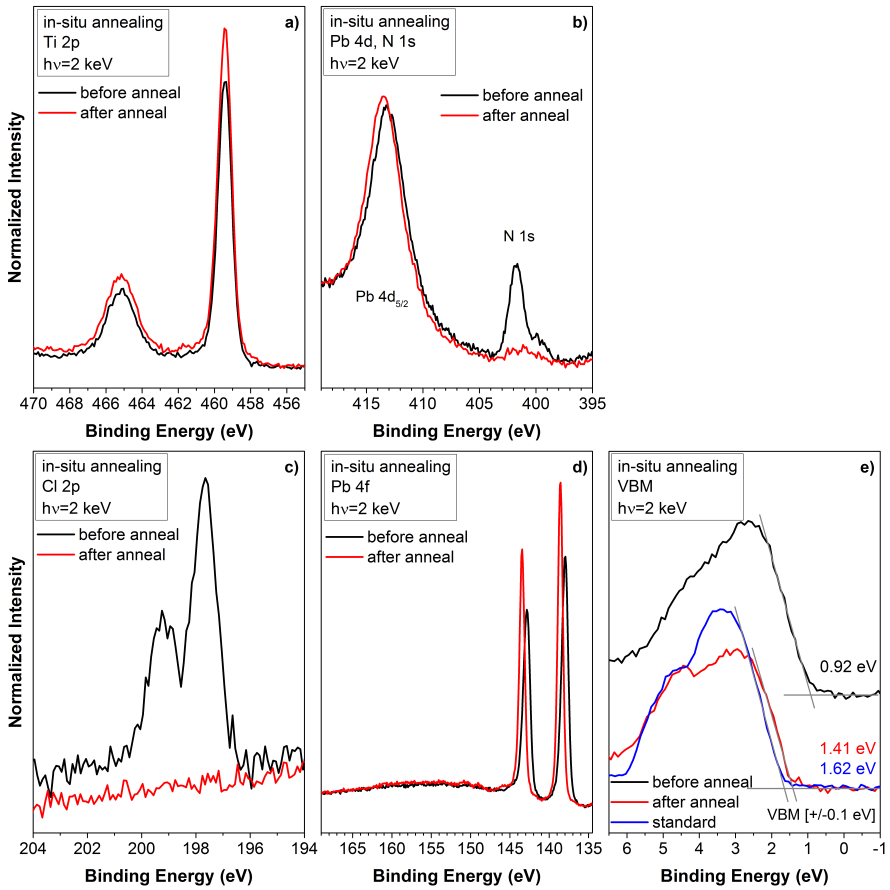

Figure 5.3: *Ti 2p (a), N 1s (b), Cl 2p (c), and Pb 4f (d) core level lines and the valence band maximum (e) of the $CH_3NH_3PbI_{(3-x)}Cl_x$ sample before (red) and after (black) anneal. Panel (e) also includes the VBM measurement (blue) of a standard 300 nm $CH_3NH_3PbI_{(3-x)}Cl_x$ film on compact TiO_2 as a reference (see section 5.2.1). Linear extrapolation of the leading edge (see also chapter 3.6) is used to derive the VBM positions.*

annealing. Prior to the in-situ heating a strong Cl 2p signal can be detected; during heating the sample the Cl 2p signal in the surface region (IMFP max. 3.3 nm) has decreased to a level below the detection limit, i.e., the estimated concentration ratio of Cl:I is less than 0.024.[162].

Further, notable changes in the Pb 4f core level occur (see Figure 5.3d). After annealing the sample to form the perovskite layer, a shift of 0.5 eV to higher binding energies is observed. The same shift can be seen for the VBM position (Figure 5.3e). The initially deposited precursor solution has a VBM value of (0.92 [$\pm$0.10] eV) and the final perovskite structure after the annealing step a VBM position of (1.41 [$\pm$0.10] eV). For comparison in panel (e)

includes the VBM spectra of a standard 300 nm $CH_3NH_3PbI_{(3-x)}Cl_x$ on c-TiO_2 (detailed sample explanation in chapter 5.2.1 and 5.2.2) with a VBM value of (1.64 [±0.10] eV). The 0.2 eV difference may be explained due to differences in Cl:I ratio, different doping, layer thickness, and/or substrate interactions. From previous studies it is known that the VBM is mainly composed by I 5p states [55, 163, 164] which might be the explanation for the shift to lower binding energies for the annealed sample. In comparison to the standard sample prepared at University of Oxford, as explained in chapter 2.2.2.2, the sample used for in-situ annealing was prepared in-house with a different precursor solution although the molar ratio of 3:1 for MAI:$PbCl_2$ was kept the same. Further, temperature differences, composition, and different preparation environment also can have a huge impact.

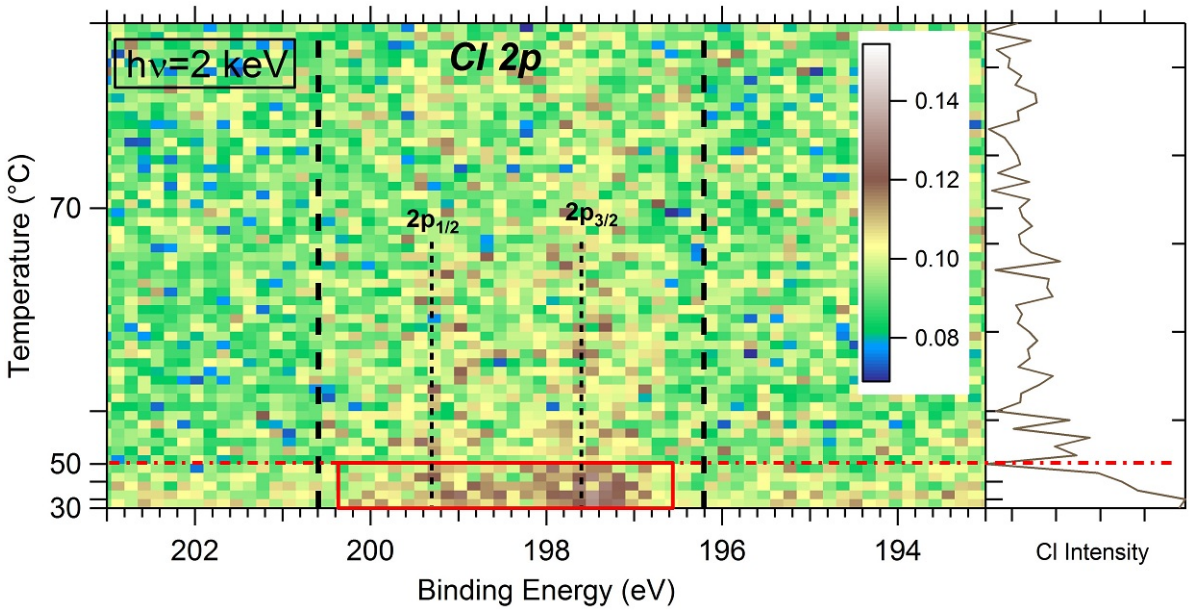

Figure 5.4: *The Cl 2p region as a function of temperature measured with an excitation energy of hν=2 keV (left panel). The Cl 2p region is indicated with dashed black lines. The red box shows the region with detectable Cl 2p signal. The right panel shows the integrated Cl intensity over temperature. The data is normalized to the background.*

Figure 5.4 shows the Cl 2p signal monitored during in-situ annealing with an excitation energy of 2 keV indicating that the decrease in Cl intensity in the surface region occurs at relatively low temperatures. Above 50°C the Cl signal has already fallen below the detection limit (see also right panel in Figure 5.4). For clarity a red box marks the region of detectable Cl signal intensity.
Such decrease in Cl signal during annealing is in agreement with literature [54, 161, 165]

suggesting that Cl evaporates in the form of methylammonium chloride (MACl) according to the most common formation reaction [54, 166]:

$$PbCl_2 + 3CH_3NH_3I \longrightarrow CH_3NH_3PbI_3 + 2CH_3NH_3Cl$$

It is also possible that Cl desorbs from the film as gaseous Cl_2 that is pumped away under UHV conditions during the annealing. Both mechanisms can also occur in inert atmosphere and in air. The extent of Cl depletion not only depends on the annealing time and temperature, but also on the formation and desorption of MACl and Cl_2 and the diffusion through the perovskite layer.
Further, during the annealing step Cl can diffuse deeper into the bulk towards the MAPb-$I_{(3-x)}Cl_x$ / TiO_2 interface.[167] This is in agreement with HAXPES and FY-XAS measurements we performed, some of which show Cl depletion in the surface and near-surface region, but a detectable Cl content located deeper in the bulk towards the TiO_2 interface.[162] The ratio of Cl:I (using Cl $2p_{3/2}$ and I 4s) in the present film before annealing is about 0.56 and therefore close to the concentration ratio of the initial solution of 0.66. For the film after annealing and a Cl signal below the detection limit, we estimated the concentration ratio of Cl:I to be less than 0.024.[162]
These earlier findings, and the drop in Cl concentration below the detection limit in Figure 5.4 support some previously published statements. Yu et al. propose "that the function of Cl (or more precisely, Cl^-) is to facilitate the release of excess $CH_3NH_3^+$ at relatively low annealing temperature."[54] Also Chae et al. find a Cl-rich phase below 60°C and a Cl-poor phase with further annealing and increase in temperature.[165] This is in agreement with our findings shown in Figure 5.4, in particular for the Cl intensity in the right panel.

From literature it is known that the investigated perovskite systems undergo a structural phase transition with temperature due to the molecular motion of the methylammonium cations.[47] We additionally monitored the Pb 4f core level during in-situ annealing (see Figure 5.5) to investigate possible compound formation processes.
Figure 5.5a again compares the Pb 4f core level in a smaller binding energy window before and after annealing taken with an excitation energy of $h\nu$=2 keV. The shift of 0.5 eV to higher binding energies for the formed perovskite layer after annealing can be clearly seen. The standard 300 nm $CH_3NH_3PbI_{(3-x)}Cl_x$ layer on compact TiO_2 included as a reference depicts almost the same Pb 4f core level binding energies as the film after annealing. The small binding energy difference can possibly be explained with the two different precursor solutions and also the different annealing environment. The same shift is also present for

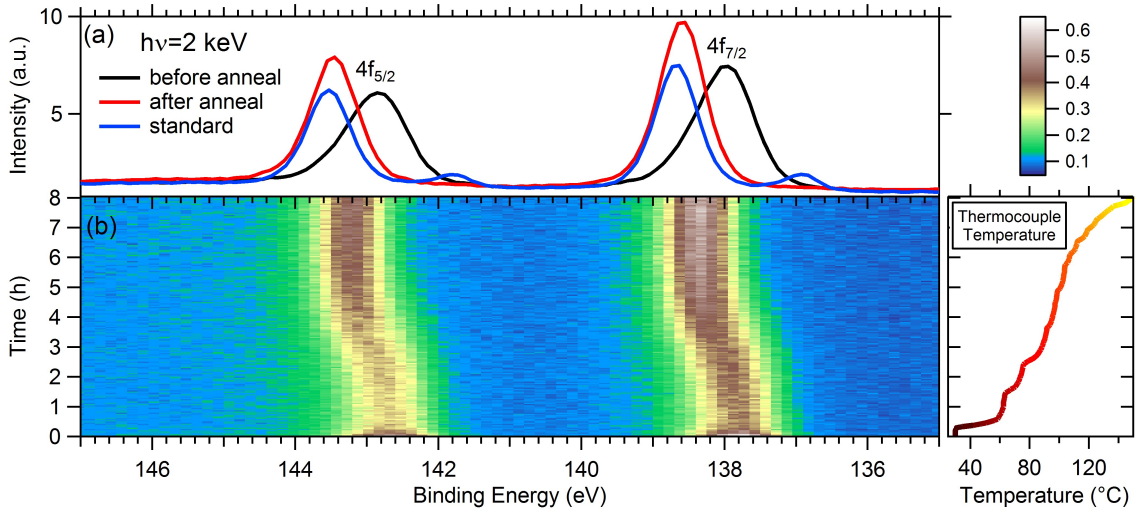

Figure 5.5: *a) displays the Pb 4f spectra before (black) and after (red) annealing together with a standard 300 nm $CH_3NH_3PbI_{(3-x)}Cl_x$ film on compact TiO_2 (blue) as reference. b) Pb 4f region as a function of time and temperature measured with an excitation energy of hν=2 keV. The data is normalized to the background.*

the position of the VBM (see Figures 5.3e and 5.6). Additionally for the standard perovskite sample metallic Pb is present. However, it obviously deviates from the film prior to heating. Figure 5.5b reveals the monitored Pb 4f core level evolution over annealing time and temperature. A notable shift in the Pb 4f peak position between 80-100°C is identified at the transition temperature for the compound formation to the final perovskite structure. This transition temperature of about 80°C has also been reported for similar $CH_3NH_3PbI_{(3-x)}Cl_x$ by other groups using x-ray scattering.[166, 168] The same shift over annealing time and temperature can be also seen on the shallow core levels in Figure 5.6. The perovskite related I 4d and Pb 5d lines show also a shift to higher binding energies at the transition temperature whereas the Ti 3p line from the substrate stays constant. The nitrogen signal monitored during annealing is too weak to make an exact statement due to the photoionization cross-section, although we can detected N 1s before and after annealing (see also Figure 5.3b). These shifts in perovskite-related material lines, but not in the Ti line, are attributed to compound formation from precursor solution to the final perovskite layer.

Further, with the shift in binding energy a narrowing of the peaks is seen. With increasing temperature and a binding energy shift to higher energies the width of the Pb 4f peaks gets

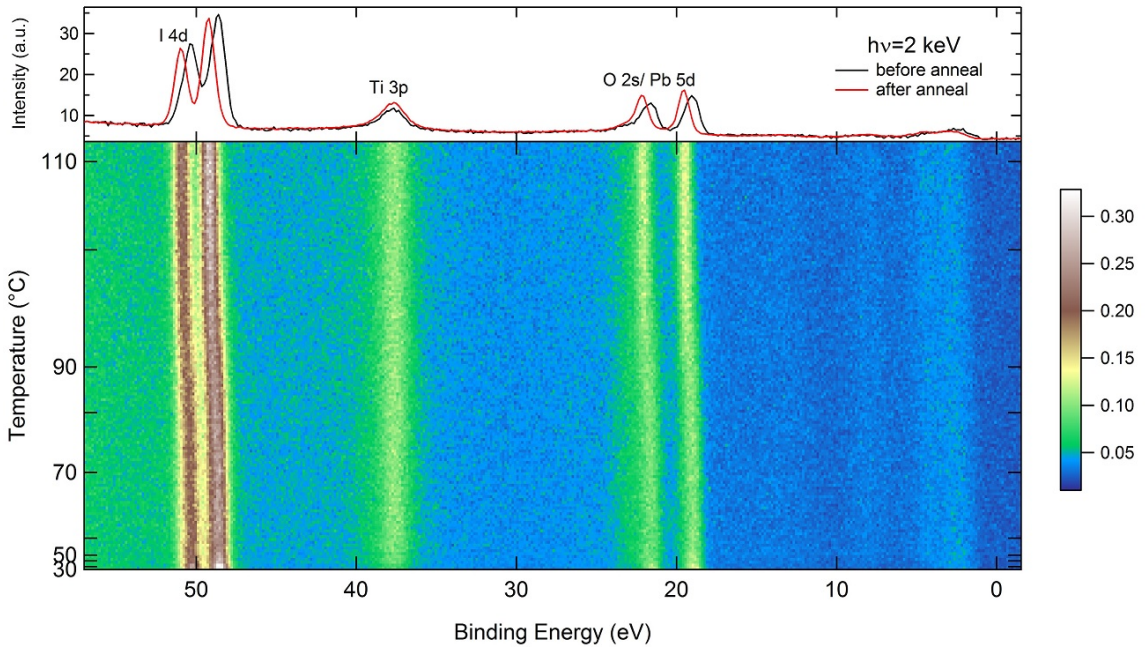

Figure 5.6: *The top panel displays the shallow core level region before (black) and after (red) annealing. The bottom panel shows the I 4d, Ti 3p,O 2s/Pb 5d, and the valence band maximum as a function of temperature measured with an excitation energy of hν=2 keV. The data is normalized to the background.*

significantly smaller. Identical observations are found for I 4d core levels.
The broad peak in the beginning of the annealing step can be attributed to more than one lead species. Most likely a mixture of $PbCl_2$, PbI_2, an intermediate phase of $(CH_3NH_3)_{x-y}PbI_{2+x}Cl_y$ [54], $CH_3NH_3PbI_{(3-x)}Cl_x$, $CH_3NH_3PbI_3$, and Pb^0 is present. After annealing only one species seems to be present in the surface region in the form of $CH_3NH_3PbI_3$.

Summary

To summarize this section, we have monitored the compound formation during in-situ annealing of a drop-casted layer of precursor solution on c-TiO_2. Spectra were taken before, during, and after annealing, revealing a shift in the Pb 4f peak position during its transition temperature between 80-100°C. This is in agreement with the formation of the perovskite layer and can be confirmed with a standard 300 nm perovskite layer on c-TiO_2. Further the Cl 2p signal decreases drastically at the onset of annealing and is depleted in the surface region after temperatures of 50°C.

5.2 $CH_3NH_3PbI_{(3-x)}Cl_x$ / TiO_2 Interface

5.2.1 Chemical Structure

5.2.1.1 HAXPES Measurements

We use hard x-ray photoelectron spectroscopy (HAXPES) measurements with an excitation energy of hν=2 keV to study the chemical and electronic properties of the $CH_3NH_3PbI_{(3-x)}Cl_x$ / TiO_2 interface. For this purpose the two most common electron transport materials (ETM), compact TiO_2 (c-TiO_2) and mesoporous TiO_2 (mp-TiO_2), are used as substrates and covered with different nominal layer thicknesses (10, 30, 60, and 300 nm) of $CH_3NH_3PbI_{(3-x)}Cl_x$. The exact procedure of the sample preparation can be found in chapter 2.2.2.

To gain first insight on the investigated samples, survey spectra taken at hν=2 keV with an IMFP of <3.5 nm are used (Figure 5.7 and 5.8). Both ETM substrates show the Auger and core level lines associated with the TiO_2 material. Additionally, carbon related peaks are detected due to surface contamination associated with sample fabrication and transport in air.
With increasing $CH_3NH_3PbI_{(3-x)}Cl_x$ layer thickness the perovskite related peaks, mainly iodine and lead, increase in intensity while the substrate related peak intensity (Ti and O) decreases (see also Figure 5.9). Even for the thickest perovskite layer of 300 nm oxygen is found and of course carbon. This is most likely a combination of carbon from the MAI-framework and carbon from surface contamination. The oxygen lines might be composed of TiO_2 related substrate contributions due to not closed absorber layers [13] and surface contamination. The samples have been briefly (< 2min) exposed to air before introduction in the UHV system. A N 1s signal for the all absorber layers is also detected. Especially for thinner layer the signal intensity is weaker due to the 10 times lower photoionization cross-section compared to Pb $4d_{5/2}$.

Further it can clearly be seen that the nominal thicknesses of 10-300 nm estimated from the precursor solution (for more detail see chapter 2.2.2.2) results in differences in actual layer thickness on the two substrate materials. This can be determined by comparing the attenuation of Ti substrate signal with the increase of perovskite material peaks like iodine and lead.

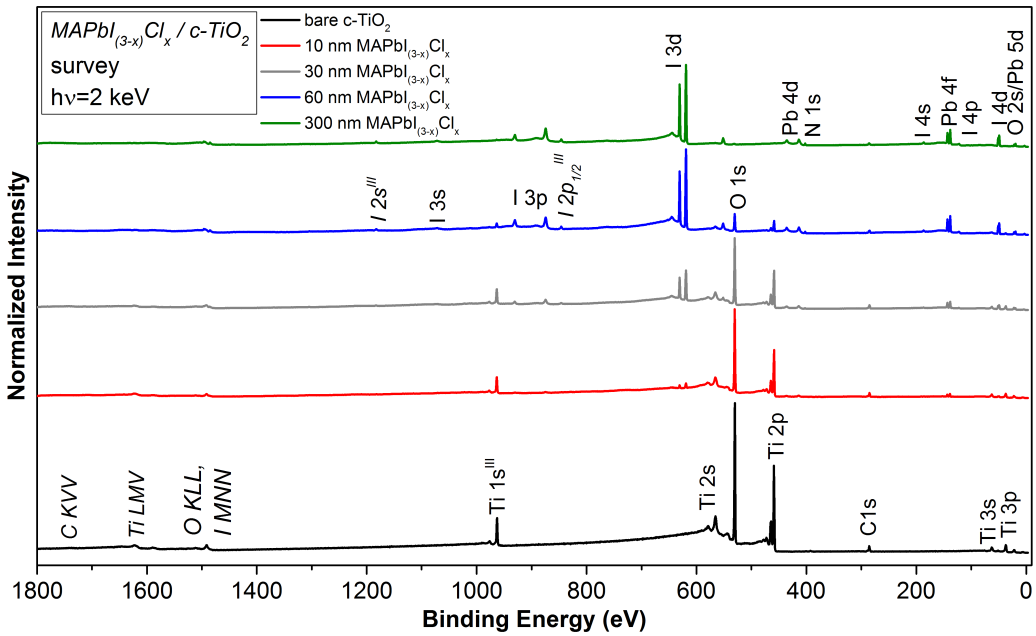

Figure 5.7: *Survey spectra of bare compact TiO_2 (c-TiO_2) as substrate material (black) and of nominal 10 nm (red), 30 nm (gray), 60 nm (blue), and 300 nm (green) $CH_3NH_3PbI_{(3-x)}Cl_x$ on top of c-TiO_2 measured with an excitation energy of hν=2 keV. The core level and Auger lines are marked. Vertical offset added for clarity.*

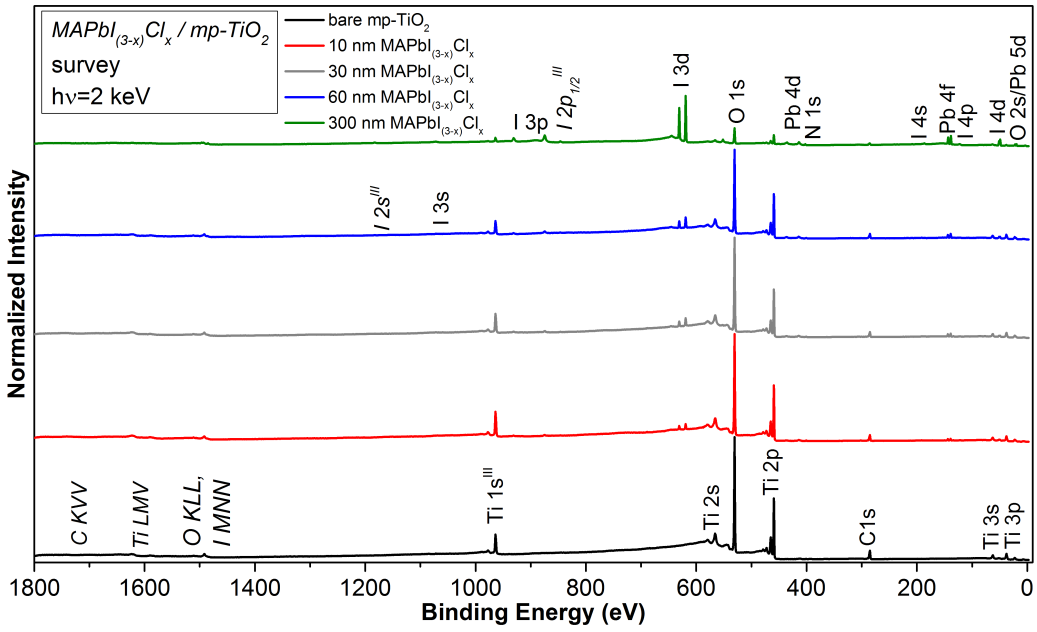

Figure 5.8: *Survey spectra of bare mesoporous TiO_2 (mp-TiO_2) as substrate material (black) and of nominal 10 nm (red), 30 nm (gray), 60 nm (blue), and 300 nm (green) $CH_3NH_3PbI_{(3-x)}Cl_x$ on top of mp-TiO_2 measured with an excitation energy of hν=2 keV. The core level and Auger lines are marked. Vertical offset added for clarity.*

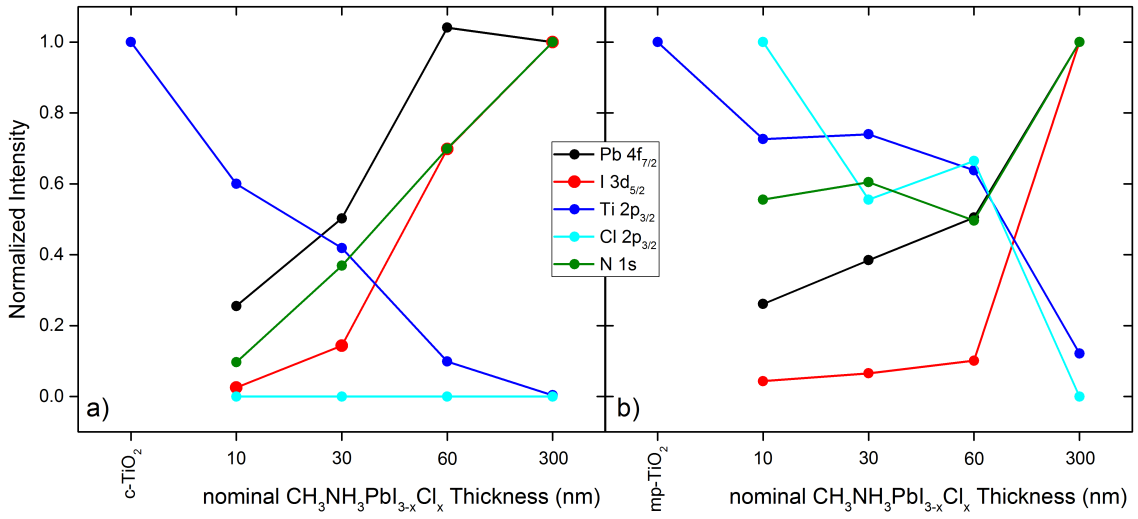

Figure 5.9: *Pb $4f_{7/2}$, I $3d_{5/2}$, Ti $2p_{3/2}$, Cl $2p_{3/2}$, and N 1s intensities, normalized to "one" for the highest intensity for each core level for $CH_3NH_3PbI_{(3-x)}Cl_x$ on compact TiO_2 (a) and on mesoporous TiO_2 (b) with nominal thicknesses of 10, 30, 60, and 300 nm.*

The attenuation of the substrate signal and the increase in perovskite related signal is less pronounced for the thickness-series on mp-TiO_2. A significantly thicker layer and/or better coverage is gained on top of the planar c-TiO_2 than for the mp-TiO_2. The difference can most likely be explained by the diffusion of the precursor solution into the pores of the mesoporous scaffold, i.e., the surface area of the mp-TiO_2 is therefore much lager.
Additionally, no notable Cl-signals are detected in the surface region within the survey spectra. However, detail scans (see Figures 5.9 and 5.12) reveal minor Cl contributions for the thinner layers of the mesoscopic structure due to the better signal-to-noise ratio and a smaller step size.

To get more specific insight into the chemical structure of the $MAPbI_{(3-x)}Cl_x$ / TiO_2 interface we use the Pb 4f core level lines shown in Figure 5.10 and 5.11.
Both panels (a) show the complete Pb 4f core level line spectra, including the spin orbit split 4f lines and the complex satellite features stretched over a range of 20-30 eV to higher binding energy. These satellite features arise because of electron (kinetic) energy losses due to the transition between the valence and conduction band in Pb(II) halides.[169, 170]

The Pb 4f core levels are simultaneously fitted with Voigt profiles [106] and linear backgrounds; the backgrounds have been subtracted in all figures. Shape and gwidth [106], i.e.,

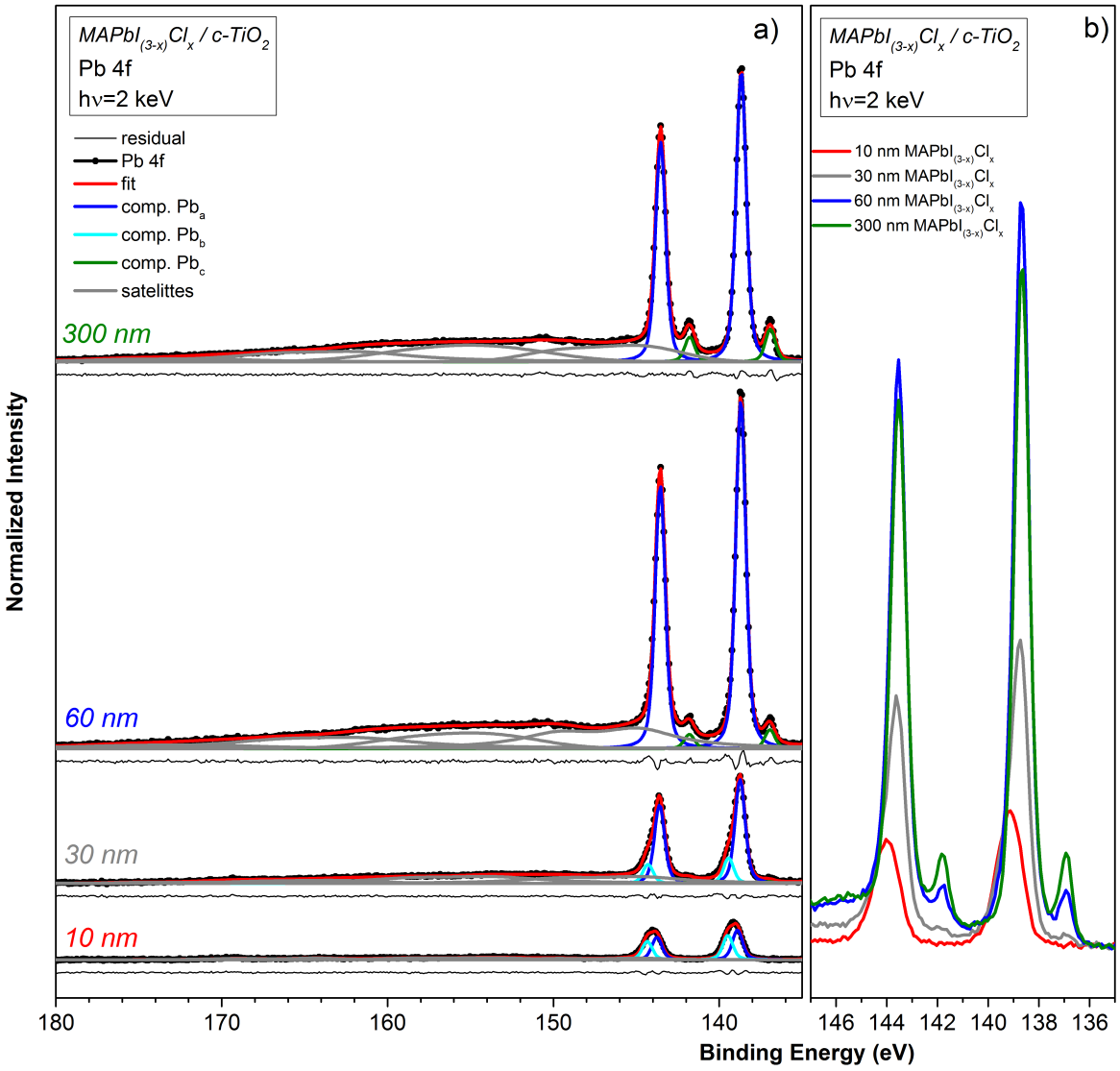

Figure 5.10: *Photoemission data of the thickness series of $CH_3NH_3PbI_{(3-x)}Cl_x$ on compact TiO_2 taken with an excitation energy of hν=2 keV of the extended Pb 4f. a) Pb 4f core level lines with the complex satellite features are displayed with their respective doublet Voigt fits. Vertical offset added. Panel b) shows the main Pb 4f core level line region.*

the FWHM of Gaussian and Lorentzian, are linked for the core level lines and the doublet separation is fixed to 4.9 eV [171]. The satellite features have their significant intensity overlap with the main peaks in the Pb 4f spectra, and so they need to be considered when quantifying the various Pb species. Further, the satellite signal is contributing to the Pb halide signal. The satellite region is fitted for each spectrum with four doublets using Voigt

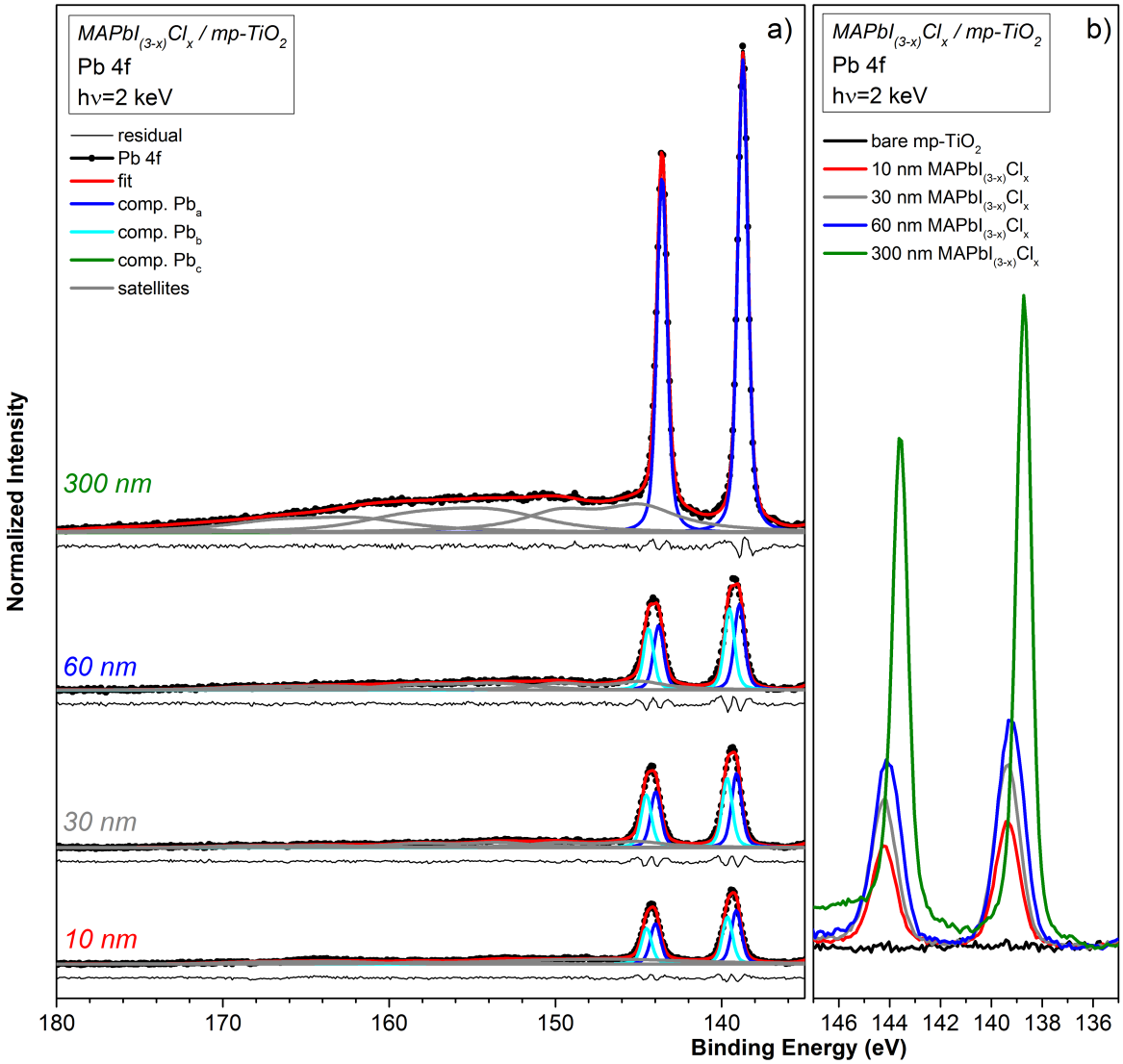

Figure 5.11: *Photoemission data of the thickness series of $CH_3NH_3PbI_{(3-x)}Cl_x$ on mesoporous TiO_2 taken with an excitation energy of hν=2 keV of the extended Pb 4f. a) Pb 4f core level lines with the complex satellite features are displayed with their respective doublet Voigt fits. Vertical offset added. Panel b) shows the main Pb 4f core level line region.*

profiles [106] and a fixed doublet separation of 4.9 eV as for the main Pb 4f core level. Lorentzian and Gaussian (shape and gwidth [106]), is only linked within each doublet.

For the thinner perovskite layers, two species for the main Pb 4f lines are needed to achieve a satisfactory fit.
For the 30, 60, and 300 nm $CH_3NH_3PbI_{(3-x)}Cl_x$ layer on c-TiO_2 and 300 nm on mp-TiO_2 an additional species at lower binding energy is needed also using Voigt profiles with the respective Pb 4f doublet separation of coupled shape and gwidth [106], i.e., Lorentzian and Gaussian widths. Further the center is linked to the main Pb 4f core level line with an energy separation of 1.7 eV.
The blue doublet (Pb_a) is ascribed to the perovskite absorber [55, 172], the cyan doublet (Pb_b) is most likely the result of a Pb-Ti-(I) type species [173–175], and the green doublet (Pb_c) is attributed to metallic lead (Pb^0) [176–178]. Such Pb-Ti-(I) type species have also been observed in X-PEEM studies by our group within the I line.[179] Further, Pb remnants are determined after rinsing of the perovskite layer on the c-TiO_2 substrate material with DMF, shifted to higher binding energies compared to the original perovskite peak, suggesting the formation of Pb-Ti bonds (see Appendix A.6).

Table 5.1: *Pb 4f peak position in binding energy of the different species measured with $h\nu$= 2 keV. An error margin of ±0.10 eV is assumed.*

sample	Pb_a	Pb_b	Pb_c	Pb_c:Pb_a ratio	Pb_b:Pb_a ratio
300 nm perovskite / c-TiO_2	138.67	-	136.92	0.11	-
60 nm perovskite / c-TiO_2	138.70	-	136.94	0.05	-
30 nm perovskite / c-TiO_2	138.74	139.44	136.99	0.02	0.24
10 nm perovskite / c-TiO_2	138.90	139.48	-	-	0.82
300 nm perovskite / mp-TiO_2	138.73	-	-	-	-
60 nm perovskite / mp-TiO_2	138.94	139.54	-	-	0.95
30 nm perovskite / mp-TiO_2	139.11	139.67	-	-	0.94
10 nm perovskite / mp-TiO_2	139.12	139.66	-	-	0.88

Two species for the main Pb 4f are seen in the spectra of the 10 nm and 30 nm absorber material on c-TiO_2 and mp-TiO_2 as well as for 60 nm perovskite on mp-TiO_2. Species Pb_a (blue doublet) representing the perovskite material significantly increases compared to species Pb_b for increasing layer thickness on c-TiO_2, in contrast to the layers on mp-TiO_2. For these $CH_3NH_3PbI_{(3-x)}Cl_x$ layers species Pb_b, which is assumed to be a Pb-Ti-(I) type species, is notably present for the first three layers and vanished for the thick 300 nm layer. Note, that within our study it is not possible to specifically derive the composition of this species. Literature shows the presence of $PbTiO_3$ [173–175] for simliar binding energies. PbO and PbO_2 are at approximately 137.7 eV [121] binding energy and therefore at lower

E_B than the main perovskite species. This would be in agreement with our findings of a more pronounced Pb_b species for the mesoscopic structure due to the increase in surface area, which means an increase in interface area.

An enhanced metallic lead Pb^0 (species Pb_c) formation is observed for the perovskite layers on c-TiO_2 compared to mp-TiO_2. However, there is no indication that the chosen substrate material has caused the formation of metallic lead due to different Ti states or hydrogen compounds. For mp-TiO_2 and for c-TiO_2 the O 1s and Ti 2p core level lines have the identical shape and so does the respective O KLL Auger line (see Appendix A.7). In the surface region we quantitatively determine a Pb^0 fraction to the spectral contribution of the main Pb 4f signal (Pb_a) of 0.02 for 30 nm, 0.05 for 60 nm, and 0.11 for 300 nm (see also Table 5.1) . In our previous studies on c-TiO_2 we found an enhanced Pb^0 signal for more bulk-sensitive measurements and a reduction for post-annealed samples.[170] Moreover, for the 60 nm sample used for the previous study the Pb^0:Pb ratio for excitation energies of 2 keV was half of what we find here for the 60 nm $CH_3NH_3PbI_{(3-x)}Cl_x$ on c-TiO_2. Although we find an increase in the fraction of metallic Pb, an increase with increasing bulk-sensitivity cannot be excluded for these samples. Further, it cannot entirely be excluded that no PbO/PbO_2 is present, nevertheless, all spectra are fitted reasonably well without including a species representing those oxides. Only a minor Pb^0 is found for the 300 nm perovskite layer on mp-TiO_2.

Figure 5.10b and 5.11b display the main Pb 4f contributions without the satellite features. Both show a thickness dependent shift of the main Pb 4f lines to lower binding energy with increasing layer thickness (see also Table 5.1). This shift correlates with an increase of species Pb_a ascribed to the perovskite species and a decrease of the Pb_b component. This is also accompanied by a narrowing of the peaks for thicker perovskite layers. This shift can be due to chemical differences, i.e., different species, and possible interface induced band bending towards the $CH_3NH_3PbI_{(3-x)}Cl_x$ / TiO_2 interface.

Simlar spectral changes to what is observed in Pb 4f are also to some extent observed for Cl 2p and I 4s, displayed in Figure 5.12. A thickness dependent increase in I 4s intensity is observed for both series. Additionally a shift to lower binding energies is observed for increasing layer thicknesses similar to the Pb shift. Detectable Cl 2p signals are only determined for the 10-60 nm $MAPbI_{(3-x)}Cl_x$ on mp-TiO_2. Here the Cl:I ratio is determined to be 1.57 for 10 nm, 0.54 for 30 nm, and 0.45 for 60 nm perovskite layer thickness using the Cl $2p_{3/2}$ and I 4s line; it decreases with increasing layer thickness (respective fits are

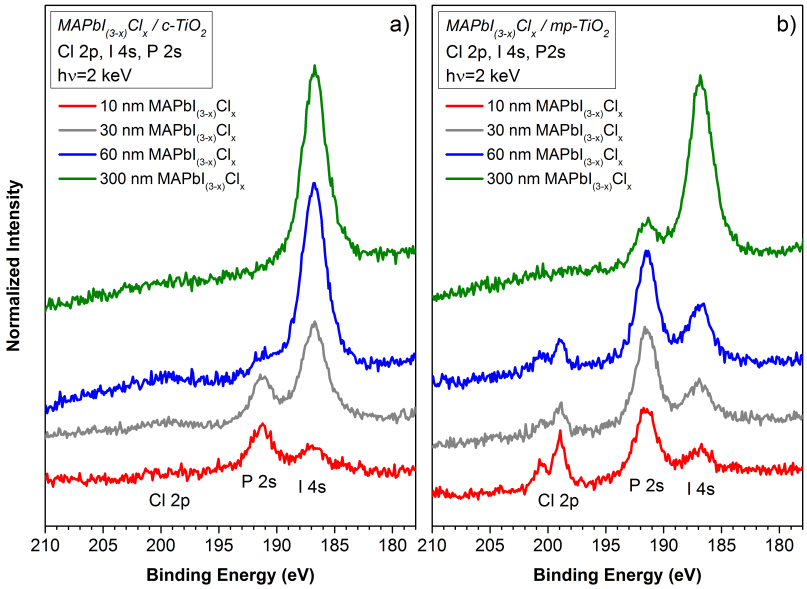

Figure 5.12: *Photoemission data of Cl 2p, P 2s, and I 4s of the thickness-series of $CH_3NH_3PbI_{(3-x)}Cl_x$ on compact (panel a) and mesoporous TiO_2 (panel b) taken with an excitation energy of hν=2 keV. Vertical offset added.*

Table 5.2: Cl:I and P:I ratio using the Cl $2p_{3/2}$, I 4s, and P 2s core level measured with hν= 2 keV.

sample	Cl:I	P:I
300 nm perovskite / c-TiO_2	-	-
60 nm perovskite / c-TiO_2	-	0.06
30 nm perovskite / c-TiO_2	-	0.39
10 nm perovskite / c-TiO_2	-	1.71
300 nm perovskite / mp-TiO_2	-	0.18
60 nm perovskite / mp-TiO_2	0.45	1.73
30 nm perovskite / mp-TiO_2	0.54	2.18
10 nm perovskite / mp-TiO_2	1.57	2.59

in Appendix A.8). This could be again an indication that some of the chlorine is diffusing towards the perovskite/TiO_2 interface.[162, 167] For the mesoscopic structure the respective thicknesses are significantly lower than what was estimated for the solution resulting in the respective layer thickness for the planar structure. It is also possible that chlorine might be trapped in the mp-TiO_2. However, the difference in Cl:I trends between the two TiO_2 types may explain the empirical preference that the mesoscopic structure is almost exclusively used

for triiodide perovskites ($CH_3NH_3PbI_3$) and not for the mixed halide $CH_3NH_3PbI_{(3-x)}Cl_x$.

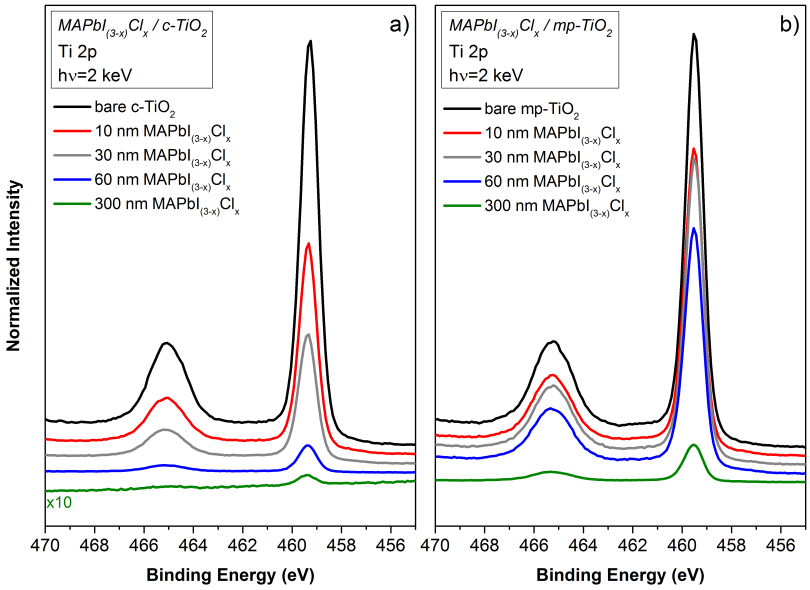

Figure 5.13: *Ti 2p spectra of the thickness-series of $CH_3NH_3PbI_{(3-x)}Cl_x$ on compact (panel a) mesoporous TiO_2 (panel b) taken with an excitation energy of hν=2 keV. The green spectrum for 300 nm $MAPbI_{(3-x)}Cl_x$ on c-TiO_2 is magnified by a factor of 10.*

For all thin layers a significant amount of phosphorous (P 2s) is detected; the P:I ratio is listed in Table 5.2. The origin of P is not clear yet. However, some amount can be associated with remnants from the precursor solution; the HI used for preparing the MAI is stabilized with H_3PO_2. The precursor solution itself was not further stabilized with phosphoric acid. Further, we found that rinsing the perovskite layer of the TiO_2 substrate with DMF results also in enhanced phosphor remnants or P is accumulated at the interface (see Appendix A.6). As explained in section 2.2.2.2 to achieve thinner layer thicknesses the original precursor solution is diluted with DMF. Especially for the mesoscopic structure a distinct amount of phosphorus is present even for the thickest layer, whereas for the planar structure no P is present for the standard thickness of 300 nm. However, no P is found on the bare TiO_2 substrate materials.

Figure 5.13 reveals the attenuating Ti 2p signal for perovskite layers on c-TiO_2 and mp-TiO_2. For all investigated layers, even the standard 300 nm $CH_3NH_3PbI_{(3-x)}Cl_x$ on c-TiO_2, a Ti signal is present, confirming holes in the layer.[13] Such holes even for the standard sample

thickness can act as point openings/pin holes having detrimental effects on the charge carrier recombination. In comparison to the material perovskite related peaks no shift can be identified for the Ti 2p signal.

Table 5.3: *The nominal and "effective" layer thicknesses for perovskite on compact and mesoporous TiO_2*

	c-TiO_2				mp-TiO_2			
nominal (nm)	300	60	30	10	300	60	30	10
effective (nm)	16.3	6.7	2.5	1.5	6.1	1.3	0.9	0.9

The intensity of the Ti $2p_{3/2}$ line can be used to calculate an "effective" layer thickness using equation 3.8 and the respective IMFP of 2.9 nm. The derived layer thickness are shown in Table 5.3 for the nominal perovskite layers of 300, 60, 30, and 10 nm on c-TiO_2 and mp-TiO_2.
Note: For calculating such "effective" layer thicknesses a closed cover layer is assumed which is not the case for any of the studied samples.

5.2.1.2 SEM and EDX Measurements

To correlate the findings of chemical properties at the perovskite / TiO_2 interface with the morphology we performed SEM and EDX measurements on the 60 nm and 300 nm samples.

Figure 5.14a shows the SEM image of a chosen sample area of the nominal 60 nm perovskite on c-TiO_2. Panels (b-f) show the EDX maps of the chosen emission signal.
The SEM image clearly shows a layer coverage of the c-TiO_2 substrate forming islands and is in agreement with literature.[13, 180] The uncovered parts show the compact TiO_2 substrate material.

This also reflects in the respective EDX maps of the same sample spot and is also in agreement with the HAXPES measurements performed. The oxygen signal is anticorrelated to that of Pb and I. The titanium signal is too noisy to conclude something.
Further, for this sample spot detectable chlorine signals are determined (see Figure 5.14c light blue spots). The Cl spots are more to the edge of the particular perovskite island and maybe even underneath the Pb. This is in good agreement with our findings using HAXPES

and FY-XAS measurements, that the Cl is found to be located towards the perovskite / TiO_2 interface.[162]

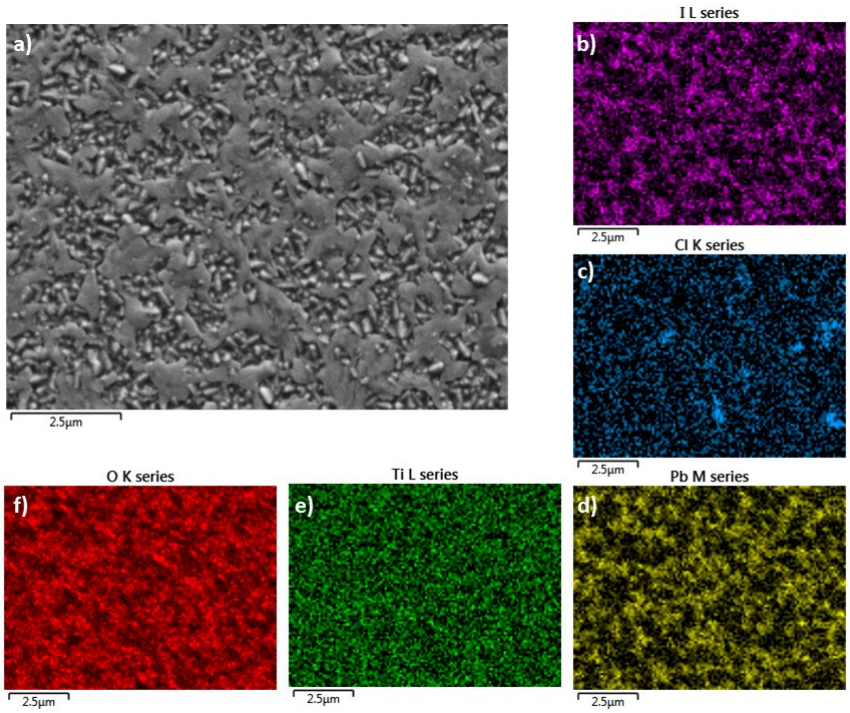

Figure 5.14: *a) SEM image of a 60 nm $CH_3NH_3PbI_{(3-x)}Cl_x$ on compact TiO_2 sample and corresponding EDX maps (b-f) of the same sample spot.*

Figures 5.15 and 5.16 show the SEM images and EDX maps of the 300 nm perovskite on compact and mesoporous TiO_2. For both samples the SEM images again reveal not closed perovskite layers on TiO_2 forming islands. Especially for the layer on c-TiO_2 the particular grain size is significantly increased compared to the 60 nm layer and also to the 300 nm layer on mp-TiO_2. Small grains and islands scattered on the mesoporous substrate are found, leaving most parts of the substrate uncovered.
Note, that for the 300 nm perovskite on c-TiO_2 sample the Ti 2p signal measured with HAX-PES (see also Figure 5.13a) was insignificantly small. This is likely due to the measurement position that is in gracing incidence.

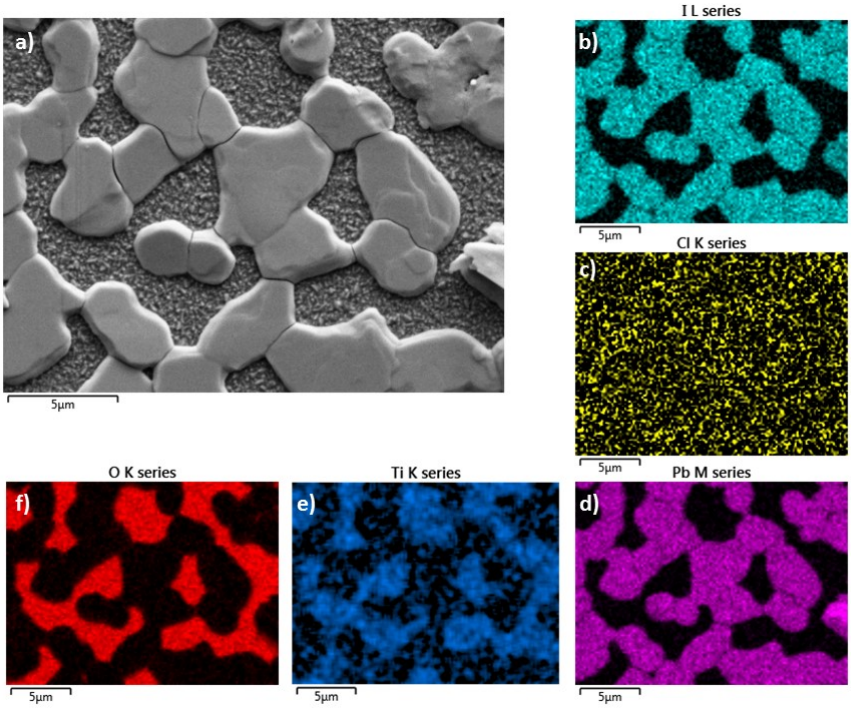

Figure 5.15: *a) SEM image of a 300 nm $CH_3NH_3PbI_{(3-x)}Cl_x$ on compact TiO_2 sample and corresponding EDX maps (b-f) of the same sample spot.*

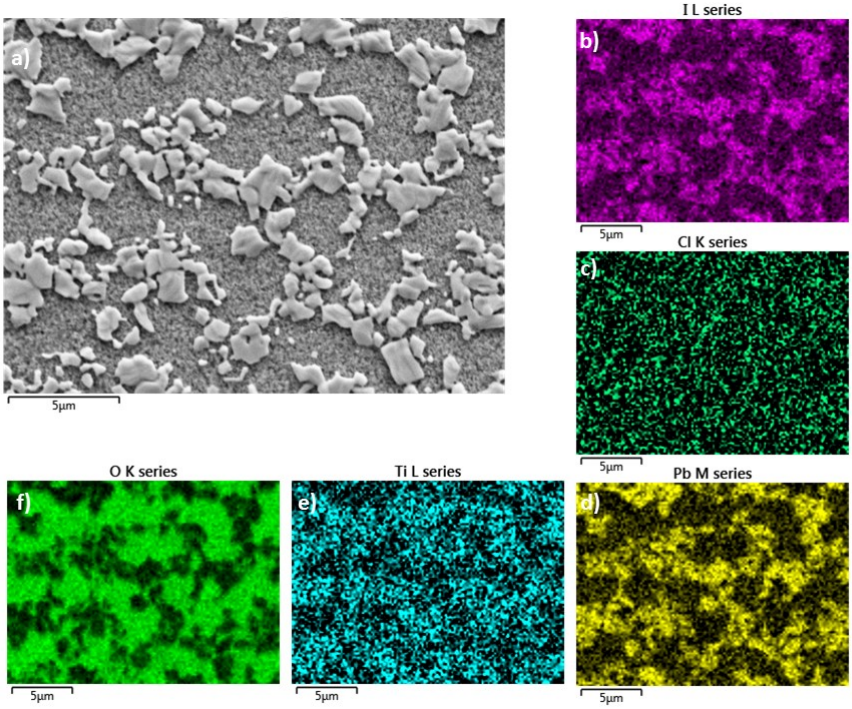

Figure 5.16: a) SEM image of a 300 nm $CH_3NH_3PbI_{(3-x)}Cl_x$ on mesoporous TiO_2 sample and corresponding EDX maps (b-f) of the same sample spot.

In both cases the Pb and I signal is again anti-correlated to the Ti and O signal, in agreement with a not complete coverage of the substrate material. However, no Cl signals are detected for nominal thicknesses of 300 nm.
For the 60 nm layer on mp-TiO_2 the layer was to thin too detect any usable signal.

Summary
To conclude this section, we have used hν=2 keV HAXPES measurement to study the chemical structure of $CH_3NH_3PbI_{(3-x)}Cl_x$ and the TiO_2 interface using the most common compact and mesoporous substrate materials. For each absorber layer a perovskite material related species is found. However, for thinner perovskite covering layers, especially on top of mp-TiO_2, a second species is forming indicating the formation of Pb-Ti-(I) bonds. Further, for the thicker $MAPbI_{(3-x)}Cl_x$ layers on c-TiO_2 metallic Pb is present. All absorber samples show an island formation on top of the substrate material not completely covering the material. This is more pronounced for the mesoscopic structure. For both structures, planar and mesoscopic, thickness induced core level shifts are determined, indicating chemical changes and/or band bending.

5.2.2 Electronic Structure

This section elucidates the electronic structure of the perovskite / TiO_2 interface on the two different ETM materials, namely compact and mesoporous TiO_2. Especially the changes due to substrate material and layer thickness can be determined and are related to changes in the chemical structure. Therefore, we have used photoelectron spectroscopy with an excitation energy of hν=2 keV with an IMFP of approximately 3.5 nm to monitor the interface formation and in particular study the changes of the valence band structure and the position of the valence band maximum (VBM).

In chapter 5.2.1 the chemical interface formation revealed an attenuation of the substrate signal and an increase in perovskite related signals with layer thickness; this was less pronounced for the mesoscopic structure. Even for the thickest layers, holes due to island formation are present. For the layers on compact TiO_2 no chlorine is found in the surface region. Moreover, a shift in binding energy, especially for Pb 4f, is found for increasing thickness and an enhanced formation of Pb^0 for the planar structure.

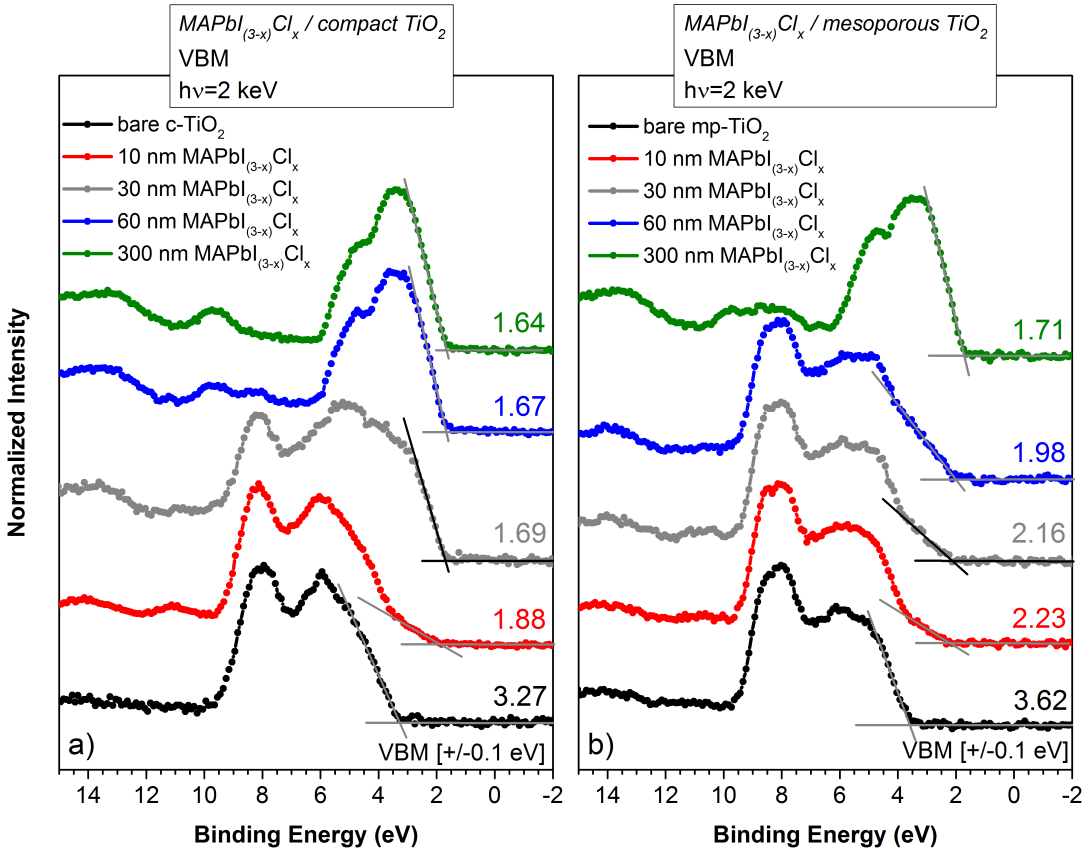

Figure 5.17: *HAXPES derived valence band spectra of the planar (a) and mesoscopic structure (b) recorded with an excitation energy of hν=2 keV for the bare compact and mesoporous TiO_2 substrate (black) and $MAPbI_{(3-x)}Cl_x$ layer thicknesses of 10 nm (red), 30 nm (gray), 60 nm (blue), and 300 nm (green). Linear approximation of the leading edges is used to determine the position of the valence band maxima.*

Figure 5.17 displays the valence band photoemission of the $CH_3NH_3PbI_{(3-x)}Cl_x$ thickness series of the planar and mesoscopic structure measured with an excitation energy of hν=2 keV. Instead of using UPS with better photoionization cross-section for determination of the valence band maxima, synchrotron-based HAXPES is used with the advantage of no satellites and less, if any, beamdamage. UV radiation, which is used for UPS leads to the degradation of the perovskite material. With an IMFP of about 3.5 nm for 2 keV instead of <1 nm for UPS, HAXPES is preferably more representative for the DOS of the perovskite material in the bulk instead of UPS representing the immediate surface. Further, the 2 keV measurements are less influenced by surface contamination.

The chemical changes previously described (section 5.2.1) also influence the valence band region and the contribution to the valence band maximum by showing distinct differences, especially for the planar structure.
The bare TiO_2 substrates both show two pronounced features between 5-9 eV mainly dominated by O 2p states.[181] The difference in spectral shape for compact and mesoporous TiO_2 is most likely caused by the differences in total density of states (TDOS) for the valence band region as is also the case for anatase and rutile TiO_2.[181] With increasing layer thickness the perovskite related contributions in the region 2-6 eV increase. They can be mainly assigned to I 5p orbitals due to the higher energy level than Pb 6s and can be associated with Pb-I-Pb bonds.[55, 182] The feature arising at 10 eV has I 5p an Pb 6s character.[55] The contribution at approximately 14 eV is associated with I 4s states.
The organic $CH_3NH_3^+$ framework also contributes to the VBM, however, these states are not experimentally detectable with HAXPES in comparison to the I and Pb states due to the lower photoionization cross-section for these materials. The cross-section for iodine-derived valence states is about 500 times higher than carbon-related and $\times 100$ higher than nitrogen-related states, respectively, Pb-derived valence states are 100 and 20 times higher. X-ray emission measurements of the N K edge show the organic contribution to the electronic structure of $CH_3NH_3PbI_{(3-x)}Cl_x$, but is not included within the studies here.
The conduction band (CB) for TiO_2 is mainly derived from Ti p-states [181], and the CB of the perovskite material from Pb p-states.[55, 182]

For both absorber series, the contributions from the TiO_2 substrate material attenuates with layer thickness, however only for the 300 nm $MAPbI_{(3-x)}Cl_x$ on c-TiO_2 no obvious detectable features from the substrate are present, in agreement with the findings for the chemical structure in chapter 5.2.1. For all other samples a notable fraction of O 2p states from the TiO_2 is present, especially for the samples in the mesoscopic structure. Here, even for a nominal thickness of 60 nm the main contribution to the VBM originates from the substrate material; only for the 300 nm MAPI on mp-TiO_2 the VBM is dominated by I 5p states from the perovskite layer.
For the planar structure a nominal thickness of 30 nm is enough to show the predominate character of the perovskite states in the valence band.

To derive the respective values of the VBM from the valence band spectra of the planar structure (Figure 5.17a) and the mesoscopic structure (Figure 5.17b) linear extrapolation of the leading edge is used. For the planar structure the VBM value of the bare c-TiO_2 is 3.27 ($\pm$0.1) eV and 1.88, 1.69, 1.67, and 1.64 ($\pm$0.1) eV for 10, 30, 60, and 300 nm MAPb-

$I_{(3-x)}Cl_x$ on c-TiO_2, respectively. For the mesoscopic structure the derived VBM values are 3.59 (±0.1) eV for bare mp-TiO_2 and 2.23, 2.16, 2.00, and 1.71 (±0.1) eV for 10, 30, 60, and 300 nm $MAPbI_{(3-x)}Cl_x$ on mp-TiO_2, respectively. In general, for both structure types the VBM shifts towards the Fermi level (E_F) with increasing layer thickness due to the predominate character of the perovskite states in the valence band. The VBM values are listed in Table 5.4 and are schematically drawn in Figure 5.18.

Table 5.4: *Values for the valence band maximum (VBM) determined from Figure 5.17 together with the derived valence band offsets (VBO) considering interface induced band bending (IIBB), according to equation 3.10 and 3.12, using ΔIIBB. The respective IIBB value are determined using the Ti $2p_{3/2}$ and Pb $4f_{7/2}$ lines for $IIBB_1$ and Ti $2p_{3/2}$ and I $3d_{5/2}$ lines for $IIBB_2$. ΔIIBB is the average of $IIBB_1$ and $IIBB_2$. The error margin for the VBM is (±0.1 eV), (±0.26 eV) for VBO, and (±0.19 eV) for IIBB.*

sample	VBM	VBO	$IIBB_1$	$IIBB_2$	ΔIIBB
bare c-TiO_2	3.27	-	-	-	-
10 nm perovskite / c-TiO_2	1.88	1.53	-0.17	-0.04	-0.10
30 nm perovskite / c-TiO_2	1.69	1.66	0.01	0.05	0.03
60 nm perovskite / c-TiO_2	1.67	1.69	0.05	0.07	0.06
300 nm perovskite / c-TiO_2	1.64	-	-	-	-
bare mp-TiO_2	3.62	-	-	-	-
10 nm perovskite / mp-TiO_2	2.23	1.59	-0.37	-0.22	-0.30
30 nm perovskite / mp-TiO_2	2.16	1.59	-0.37	-0.26	-0.32
60 nm perovskite / mp-TiO_2	1.98	1.74	-0.18	-0.16	-0.17
300 nm perovskite / mp-TiO_2	1.71	-	-	-	-

Such VBM values are mostly in agreement with what is found in literature for the substrate and the standard layer thickness of 300 nm.
For anatase TiO_2 optical band gap values are found at 3.4 eV [183, 184] and 3.2 eV [181]. Schulz et al. determine a VBM value of 3.2 eV and a CBM value of 0.1 eV for the surface region for dense TiO_2 using a combination of UPS and IPES.[56]
In general, band gap values for rutile TiO_2 are stated to be smaller than for anatase. Band gap values of about 3.0 eV are reported [181, 184, 185] and an electronic band gap of 3.2 eV is derived by Lindblad et al. [55]. These values are all smaller than the 3.6 eV for the mesoporous TiO_2 used in our studies even considering the error margin of (±0.1) eV. However, it is suggested that differences in fabrication of TiO_2 layers can highly influence the valence band properties that are dominated by O 2p.[181]

Similar comparisons can be done for the standard 300 nm perovskite layers. VBM values of 1.3 eV [56] for $CH_3NH_3PbI_{(3-x)}Cl_x$ on dense TiO_2 and 1.62 eV [176] for $CH_3NH_3PbI_{(3-x)}Cl_x$ on mp-TiO_2 are determined using photoelectron spectroscopy. The same is done for pure triiodide films of $CH_3NH_3PbI_3$ and VBM values are 1.4 eV [56] and 1.72 eV [186] on dense/compact TiO_2 and about 1.5 eV [55] on mp-TiO_2. The VBM values derived in our study are at the upper bound of what is found in literature. However, the conditions of sample fabrication are even more crucial for the absorber layer and can therefore significantly alter the electronic structure. Schulz et al. derived a CBM value of 0.4 eV for $CH_3NH_3PbI_{(3-x)}Cl_x$ and 0.3 eV for $CH_3NH_3PbI_3$ using IPES leading in both cases to an electronic band gap of 1.7 eV for the perovskite absorber layer.[56]

The derived VBM values listed in Table 5.4 and schematically shown in Figure 5.18 can be used to determine the valence band offset (VBO) between the substrate material and the thickest perovskite layer. Taking the core level shifts for the perovskite layers into account (see also chapter 5.2.1), indicating possible band bending, the VBO can be calculated according to equation 3.12 taking the interface induced band bending (IIBB) [90] into account (equation 3.10). An average IIBB (ΔIIBB) was calculated using the Pb 4f and I 3d core level for the cover layer and Ti 2p core levels for the substrate for all nominal layer thickness in each structure. Note, that for calculating IIBB values closed covering layers are assumed, which is not found for the perovskite layers in this study (see also chapter 5.2.1). Figure 5.19 shows the interface band structure using the calculated average IIBB for the perovskite layers. Further, the derived VBO values considering IIBB are about 1.6 eV and with increasing layer thickness the peak positions tends towards the "bulk" value of the thick layers.
Note: Since small regions without interface contact will have different band bending, assymetric broadening of the peaks could be expected. If we assume holes that are significantly smaller than the size of the depletion region, we can neglect their effect and account for the structural inhomogeneity with a small increase in the error margin.

Further a thickness dependent picture of the valence band position in the planar and mesoscopic structure with respect to E_F can be drawn (Figure 5.18).
For the 30, 60, and 300 nm layer on c-TiO_2 the VBM values stay basically constant and only for the thinnest 10 nm layer shifts away from the Fermi level towards the VBM value of the TiO_2 substrate layer, suggesting band bending towards the TiO_2. This might indicate a more homogeneous layer formation on top of c-TiO_2. This could also indicate that the interface is "completely" formed after a thickness of 10 nm of $MAPbI_{(3-x)}Cl_x$ on c-TiO_2.

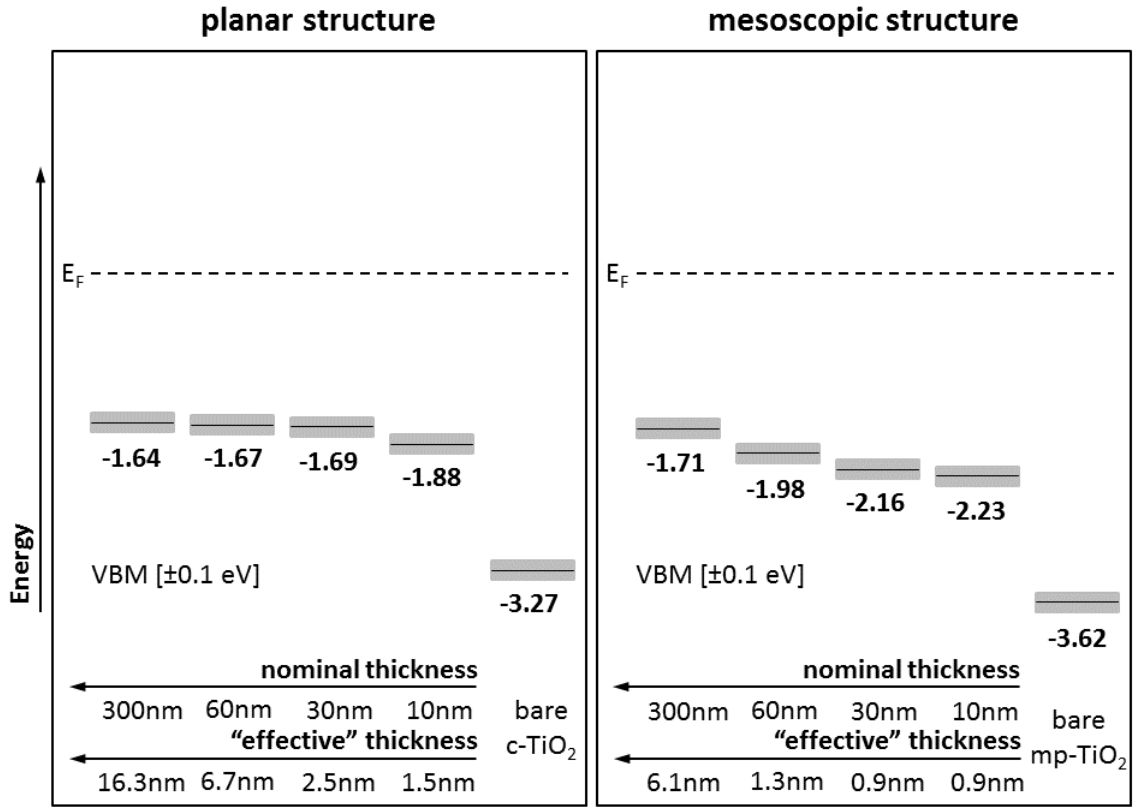

Figure 5.18: *Schematic of the valence band positions for the planar (left) and mesoscopic structure (right) with respect to the Fermi level E_F, determined using hν=2 keV photoemission measurements having different nominal and "effekitve" $CH_3NH_3PbI_{(3-x)}Cl_x$ layer thicknesses. The "effective" layer thickness was calculated using the Ti $2p_{3/2}$ line and equation 3.8 under the assumption of closed layers. The gray boxes indicate the experimental uncertainty.*

It is also suggested that metallic Pb leads to Fermi level pinning due to the shallow donor levels.[176] For the layers in the planar structure Pb^0 is present in all samples, except the 10 nm one, which is consistent with the findings for the VBM values. In our previous study on similar samples a Fermi edge due to the presence ob Pb^0 was measured with an excitation energy of hν=6 keV.[170] In this study it was observed that, to reduce the amount of metallic lead a short post-annealing process in air helps improving the solar cell performance.[170] An enhanced formation of metallic Pb can be detrimental by introducing shunt paths and/or forming sub-band gap states.[55, 170, 187] For the Pb^0 containing samples in this study no detectable Fermi edge is present, which might be due to a not sufficient signal-to-noise ratio

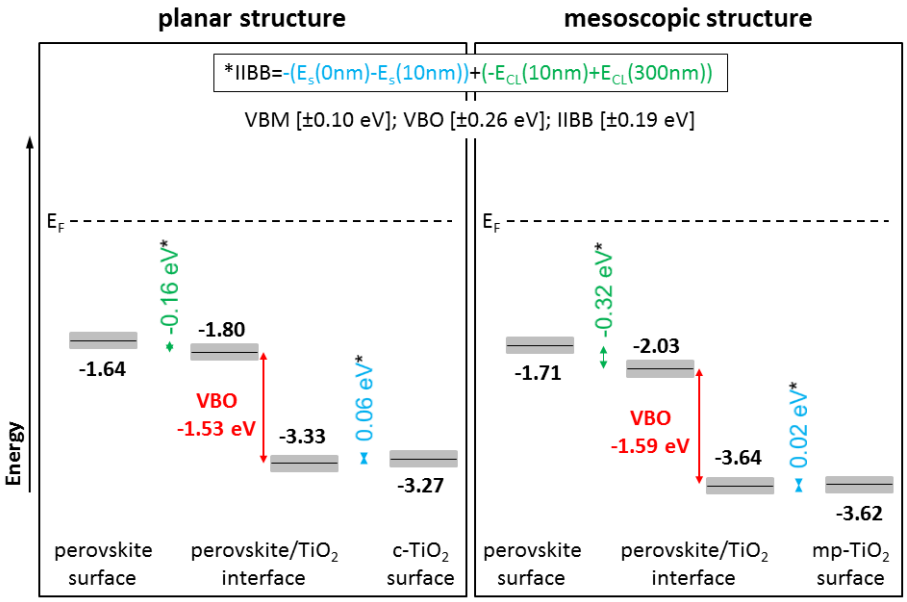

Figure 5.19: *Schematic of the valence band positions for the planar (left) and mesoscopic structure (right) with respect to the Fermi level E_F, determined using hν=2 keV photoemission measurements having different $CH_3NH_3PbI_{(3-x)}Cl_x$ layer thicknesses using the average IIBB values. The gray boxes indicate the experimental uncertainty.*

for these measurements. Although the amount of Pb^0 for the 60 nm sample is twice from what we observed for the samples used within Ref. [170] no clear Fermi edge was measured at hν=2 keV within that study as well.

Comparing the VBM energy levels for the planar structure with electronic band gap values found in literature, E_g=1.7 eV [56] for $CH_3NH_3PbI_{(3-x)}Cl_x$ and 3.3 eV for dense TiO_2 this would lead to CBM values of 0.06 eV for the 300 nm $MAPbI_{(3-x)}Cl_x$ layer and 0.03 eV for the c-TiO_2. In both cases the CBM would be close to the Fermi level. Schulz et al. determine a VBM value of about 1 eV and a CBM value of approximately 2.3 eV for the hole transport layer using spiro-MeOTAD on $CH_3NH_3PbI_{(3-x)}Cl_x$.[56] Applying these values to our findings, we would get a VBO of 0.64 eV at the interface of spiro-MeOTAD / perovskite and a CBO of 2.24 eV. This would suggest a large spike between the hole transport layer and the perovskite material and a flat-band behavior of the perovskite / TiO_2 interface. The important band alignment for these perovskite solar cell is the interface between spiro-MeOTAD / $CH_3NH_3PbI_{(3-x)}Cl_x$. In this case the VBM of the HTM is closer to E_F than the perovskite material, consequently no hole extraction barrier is present.[56] However, the large VBO value of about 0.6 eV limits the built-in field.[56] Further it leads to thermoionic losses of

the holes [188] leading to a reduction in V_{OC}.[56]

In the case of the mesoscopic structure the VBM values gradually shift away from the Fermi level towards the TiO_2 VBM value. This might most likely be a mixture of band bending towards the TiO_2 interface and chemical changes (see chapter 5.2.1) or a more gradual change of the electronic structure at the interface due to a 3-D interface. Especially for the 10, 30, and 60 nm layer on mp-TiO_2 two Pb species are found and also a significant amount of Cl. Comparing the valence band positions for the mesoscopic structure to the band gap values determined by Schulz et al. [56], in all cases the Fermi level would overlap with the conduction band. This has detrimental effects on the performance of the solar cell due to a missing junction because of a non-existing conduction band in that case. This might be another indication on why the chlorine-based mixed halide perovskites ($CH_3NH_3PbI_{(3-x)}Cl_x$) are mostly used within the planar structure.
For both structure types the perovskite material shows an n-type behavior.

Summary
To conclude this section we have used photoelectron spectroscopy with an excitation energy of hν=2 keV to characterize the electronic structure of various perovskite layers in the planar and mesoscopic structure. For both structure types the VBM shifts towards the Fermi level E_F with increasing layer thickness. For the mesoscopic structure the VBM is significantly influenced by valence states of the TiO_2 substrate due to chemical changes and/or interface induced band bending. For the planar structure the VBM stays almost constant and shows downward band bending towards the TiO_2 substrate for the thinnest layer. This is also the case for $CH_3NH_3PbI_{(3-x)}Cl_x$ on mp-TiO_2.

6

Conclusion and Outlook

For chalcopyrite-based thin film solar cell absorbers (Cu(In,Ga)Se_2) the impact of different alkali treatments (alkali-rich and alkali-poor) on the chemical surface and near-surface structure was studied using depth-dependent laboratory- and synchrotron-based photoelectron spectroscopy. A Cu-poor surface is revealed for the alkali-free and NaF-PDT CIGSe absorber of both series. The same chemical environment for indium and selenium is revealed, deriving the modified Auger parameter α'(In) and α'(Se). Altogether no significant differences are present for the alkali-rich and alkali-poor NaF-PDT CIGSe and the respective alkali-free CIGSe absorber. In contrast, a further Cu and Ga-depletion for the alkali-poor NaF/KF-PDT compared the respective alkali-free and NaF-PDT sample is observed and the chemical surface and near-surface structure of the alkali-rich NaF/KF-PDT CIGSe absorber reveals a Cu- and Ga-devoid surface region. Additionally, the topography of the NaF/KF-PDT samples show a nanopatterned structure with more distinct features for the alkali-rich sample. Further, two different species for both NaF/KF-PDT absorbers as evident from core level lines and the modified Auger parameter are present. These species can be assigned to a K-containing (i.e., K-In-Se) compound and a K-free (i.e., Cu-In-Ga-Se) compound with the same Cu-poor structure as that of the alkali-free and NaF-PDT CIGSe. A decrease in K and an increase in Cu is observed for more bulk sensitive measurements. The derived

composition for the Cu-In-Ga-Se compound is similar to what is found for the alkali-free and NaF-PDT sample. The same is found for the In and Se species of the modified Auger parameter. The findings for the chemical structure support the formation of a K-In-Se/Cu-In-Ga-Se bilayer structure, with a more pronounced K-In-Se for the alkali-rich NaF/KF-PDT CIGSe sample.

Using K $L_{2,3}$ we experimentally confirm that, after rinsing with ammonia/water, no KF remnants are present for NaF/KF-PDT and KF-PDT In_2Se_3, which is also in agreement with the findings using photoelectron spectroscopy. The chemical environment for the samples after rinsing is the same but clearly differs from the KF (powder) reference, suggesting that K is incorporated into the CIGSe/In-Se substrate and/or forms a new fluorine-free compound.

The local Se density of occupied states for the CIGSe sample was examined using Se $M_{4,5}$ XES revealing the identical Se structure for alkali-free and alkali-rich NaF-PDT and similar to what is found for the respective alkali-poor CIGSe absorbers. The alkali-rich NaF/KF-PDT and the KF-PDT In_2Se_3 exhibit an additional feature ascribed to K 4s derived states indicating the formation of Se-K bonds. This feature is much smaller for alkali-poor NaF/KF-PDT, but it can also be identified by a superposition of properly weighted NaF-PDT and KF-PDT In_2Se_3 Se $M_{4,5}$ XES spectra. The corresponding chalcopyrite spectra and the KF-PDT In_2Se_3 reference sample also clearly deviate from an In_2Se_3 (powder) reference. This is another confirmation for the formation of a K-In-Se type species (rather than a simpler Cu- and Ga-depletion) which can be "tuned" by a different degree of alkali PDT. Using the properly weighted sums together with the derived attenuation length for Se $M_{4,5}$ XES an approximated "effective" thickness of 8.8 nm for the alkali-rich NaF/KF-PDT and 1.3 nm for the alkali-poor NaF/KF-PDT sample can be derived for the K-In-Se top layer.

The electronic structure (i.e., the position of VBM and CBM) and the impact of the different alkali post-deposition treatments (i.e., alkali-rich and alkali-poor) were studied using direct and inverse photoemission. For the alkali-rich treated CIGSe absorbers we find VBM values of -0.76, -0.72 ($\pm$0.15) eV, and 0.86 ($\pm$0.10) eV for the alkali-free CIGSe and -0.55, -0.58 ($\pm$0.10) eV, and -0.66 ($+0.10/-0.15$) eV for NaF-PDT CIGSe with increasing surface sensitivity. For the respective alkali-poor absorbers we observe VBM values of -0.76, -0.72 ($\pm$0.10) eV for alkali-free CIGSe and -0.59, -0.65 ($\pm$0.10) eV for NaF-PDT and NaF/KF-PDT CIGSe. Both NaF-PDT samples show a shift in VBM position towards the Fermi level due to Na incorporation leading to a more p-type material. The VBM of the alkali-rich

NaF/KF-PDT CIGSe sample observed a large and more gradual change towards the surface with VBM position of -0.95, -1.10, and -1.26 ($\pm$0.10) eV. Together with the CBM provided by IPES measurements the near-surface electronic band gap value is obtained. A band gap of 1.61 [$+0.14/-0.51$] eV at the surface is observed for the alkali-rich NaF-PDT sample which is larger than the observed bulk value of 1.15 eV. However, it is similar to what is observed for other high-performing CIGSe absorbers at the surface. The alkali-rich NaF/KF-PDT CIGSe observes a significant band gap widening at the surface of 2.25 [$+0.14/-0.51$] eV. This can be attributed to the formation of a K-In-Se surface compound and near-surface region due to the heavy Cu- and Ga-depletion. This value is therefore compared to band gap values for In_2Se_3 and $KInSe_2$ compounds having similar band gap values. The alkali-rich NaF/KF-PDT induced band gap widening at the CIGSe surface my act as a beneficial passivation layer between emitter and absorber. This might be the reason for the observed performance leap of respective solar cell devices and the difference in performance between the alkali-poor and alkali-rich NaF/KF-PDT CIGSe.[80]

To enhance these findings on the impact of alkali treatments on Cu(In,Ga)Se_2 thin film solar cells, one would in a next step try to study the absorber/buffer interface. Especially the influence of the formation of the CdS in a chemical bath on the identified K-In-Se surface species needs to be explored with respect to the chemical and electronic structure. The best approach is to subject the alkali-free, NaF-PDT, and NaF/KF-PDT CIGSe to different CdS bath-deposition times resulting in different CdS layer thicknesses. With depth-dependent laboratory- and synchrotron- based photoelectron spectroscopy chemical differences and maybe the formation of different species due to different alkali treatment could be revealed. Se $M_{4,5}$ XES could be used to study possible CdSe formation and variations based on the alkali treatments. Direct and inverse photoemission can be applied to study the electronic structure and obtain a more complete picture of the energy levels. Especially the band gap widening of the NaF/KF-PDT sample with respect to the CdS layer needs to be considered and how it may impact the energy level alignment. These findings can then be used to determine the band alignment between absorber and buffer.
In addition, one could also use different alkali materials, i.e., CsF, RbF, or even LiF, for the post-deposition treatments of the CIGSe absorbers and study the impact on the chemical and electronic surface and near-surface structure. Even replacing the CdS layer with a non-toxic layer, e.g. ZnO, is another approach for further research studies.

For characterizing the compound and interface formation of organo-metal mixed halide perovskites, specifically $CH_3NH_3PbI_{(3-x)}Cl_x$, HAXPES, SEM, and EDX are used.
The compound formation was monitored during in-situ annealing of a drop-casted layer of precursor solution on c-TiO_2. Using synchrotron photoelectron spectroscopy measurements before, during, and after annealing reveals shifts in the perovskite core levels during its transition temperature between 80-100°C. This is in agreement with the formation of the perovskite layer and can be confirmed with a standard 300 nm perovskite layer on c-TiO_2. Further the Cl 2p signal decreases drastically at the onset of annealing and is depleted in the surface region after temperatures of 50°C.

The chemical structure of $CH_3NH_3PbI_{(3-x)}Cl_x$ and its interface to the TiO_2 using compact and mesoporous TiO_2 substrate materials is revealed using hν=2 keV HAXPES measurements. For each absorber layer a perovskite material related species is found increasing with increasing layer thickness, whereas the substrate related core levels are attenuating. However, for thinner perovskite covering layers, especially on top of mp-TiO_2, a second species is forming indicating the formation of Pb-Ti-(I) bonds. Further, for the thicker $MAPbI_{(3-x)}Cl_x$ layers on c-TiO_2 metallic Pb is present. All absorber samples show an island formation on top of the substrate material not completely covering the material which is in agreement with the morphology studied with SEM. This is more pronounced for the mesoscopic structure. For both structures, planar and mesoscopic, thickness induced core level shifts are determined, indicating chemical changes and/or band bending.

The electronic structure of various perovskite layers in the planar and mesoscopic structure is also studied using hν=2 keV HAXPES measurement. For both structure types the VBM shifts towards the Fermi level E_F with increasing layer thickness. For the mesoscopic structure the VBM is significantly influenced by valence states of the TiO_2 substrate due to chemical changes and/or interface induced band bending due to thinner layers. For the planar structure the VBM stays almost constant and shows bend bending towards the TiO_2 substrate for the thinnest layer.

In a next step one would investigate the perovskite/hole transport material interface and the changes in chemical and electronic structure using laboratory and synchrotron-based photoelectron spectroscopy. In the end a complete picture of the energy level alignment could be given to further help understanding the exact working principle for these type of solar cells. Especially the replacement of the Pb as a toxic material with a less toxic one, e.g. Cs, is of

interest for these material systems leading to new chemical and electronic properties. One of the major and crucial points for perovskite-based solar cell structures is the device stability. Up until now these material systems are lacking in stability by showing a fast degradation, especially in humid environment. An increase in long-term stability would be of significance.

A

Appendix

A.1 Cu Background Subtraction

Figures A.1 to A.3 represent the background subtraction approach employing a properly shifted and scaled KF-PDT In_2Se_3 reference spectrum to account for the broad In 4p background (between 80 and 60 eV) that overlaps with the Cu 3p signal. For the proper energy shift and scaling factor the spectra were aligned such that the In 4d line overlap was maximized. Note that the low binding energy In 4d state may have a band-like character, rather than being a pure core level, and so its relative intensity could conceivable be influenced by the chemical environment. However, given that the formal oxidation state of the In will not be affected by the presence/absence of Cu or Ga in the structure, we expect that this would be at most a minor effect. The reference sample was always measured with the same set-up and excitation energy except for 8 keV. Here, the reference was measured with 6 keV at a different endstation but with the same experimental geometry. To account for the different changes of the photoionization cross-sections (see also chapter 3.6.2) of In 4p and In 4d when excited with 6 or 8 keV, the shifted and scaled 6 keV KF-PDT In_2Se_3 spectrum, after maximizing the In 4d overlap, was multiplied with the respective cross-section ratio of 1.35

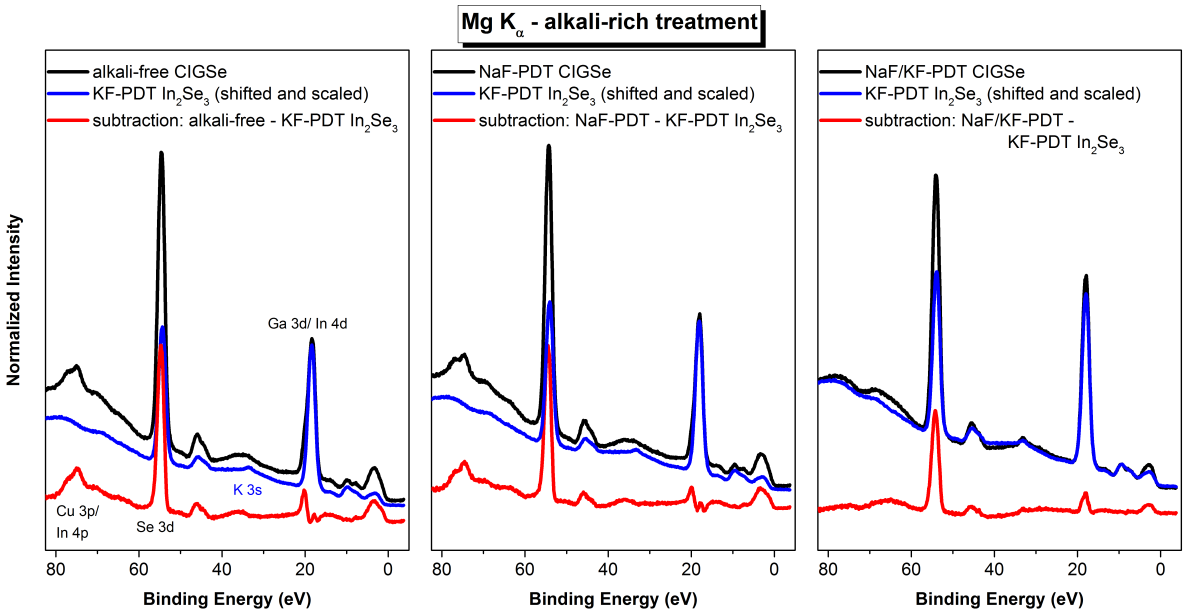

Figure A.1: *The In 4p background correction approach of the Cu 3p line using the KF-PDT In_2Se_3 reference for the differently treated alkali-rich absorbers (alkali-free [left], NaF-PDT [center], and NaF/KF-PDT [right]), measured with an excitation energy of 1253.56 eV (Mg K_α). The as-measured spectra are shown in black, individually shifted and scaled KF-PDT In_2Se_3 spectra in blue, and the red spectra correspond to the difference of the two.*

before using it to correct for the In 4p background. This results in a "negative" overshoot in the range of the In 4d line in the difference spectrum (see Figure A.3); the smaller overshoots in the other difference spectra can be explained by slight variations of the core level binding energies and/or composition profiles. The incomplete subtraction of the Se 3d lines is related to the composition differences (i.e., the In/Se ratio) between the K-In-Se reference and the absorbers. For the alkali-free and NaF-PDT CIGSe, the Ga 3d signal at around 20 eV is still present after subtraction.

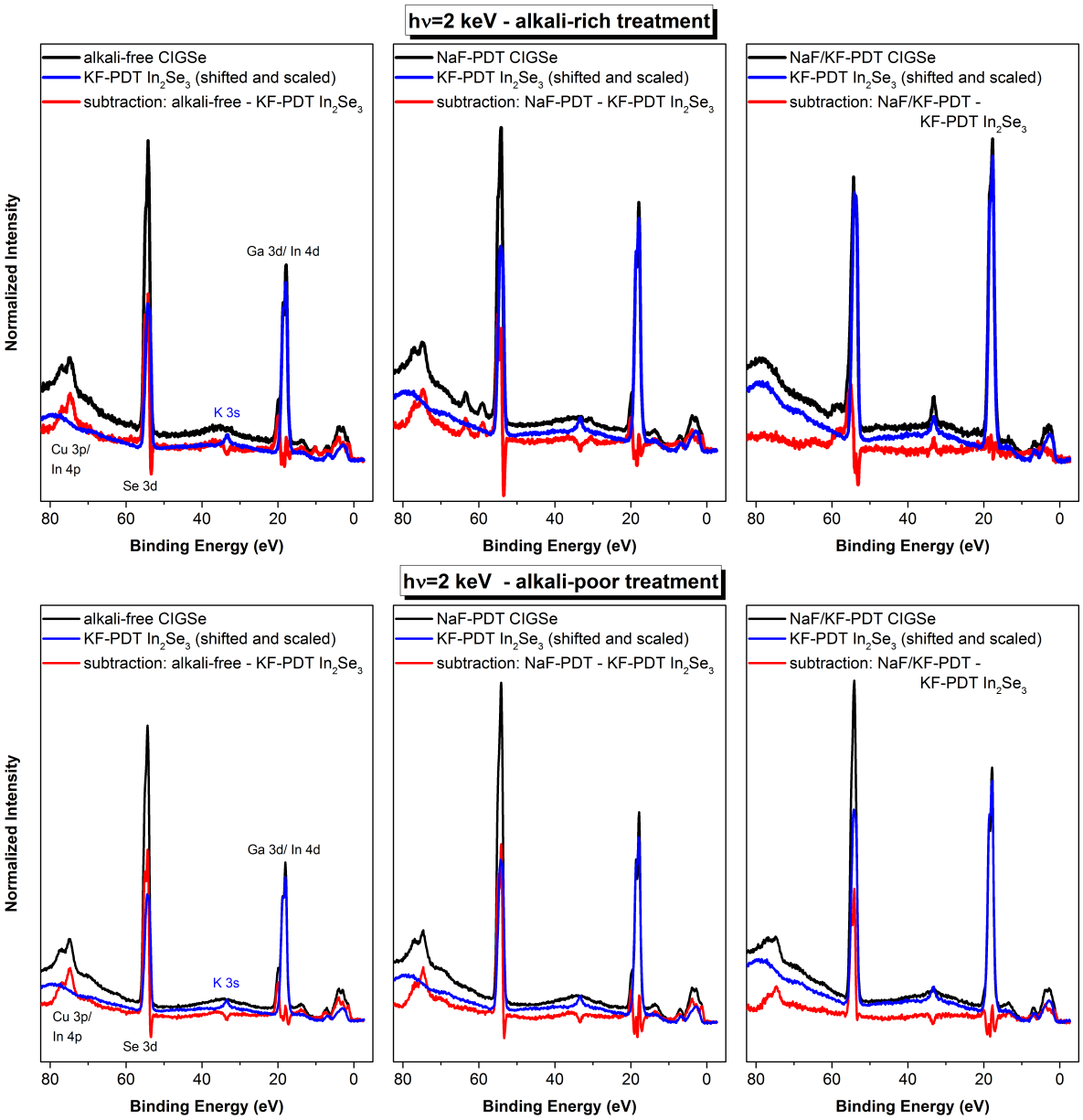

Figure A.2: *The In 4p background correction approach of the Cu 3p line using the KF-PDT In_2Se_3 reference for the differently treated alkali-rich [top] and alkali-poor [bottom] absorbers (alkali-free [left], NaF-PDT [center], and NaF/KF-PDT [right]), measured with an excitation energy of hν=2 keV. The as-measured spectra are shown in black, individually shifted and scaled KF-PDT In_2Se_3 spectra in blue, and the red spectra correspond to the difference of the two.*

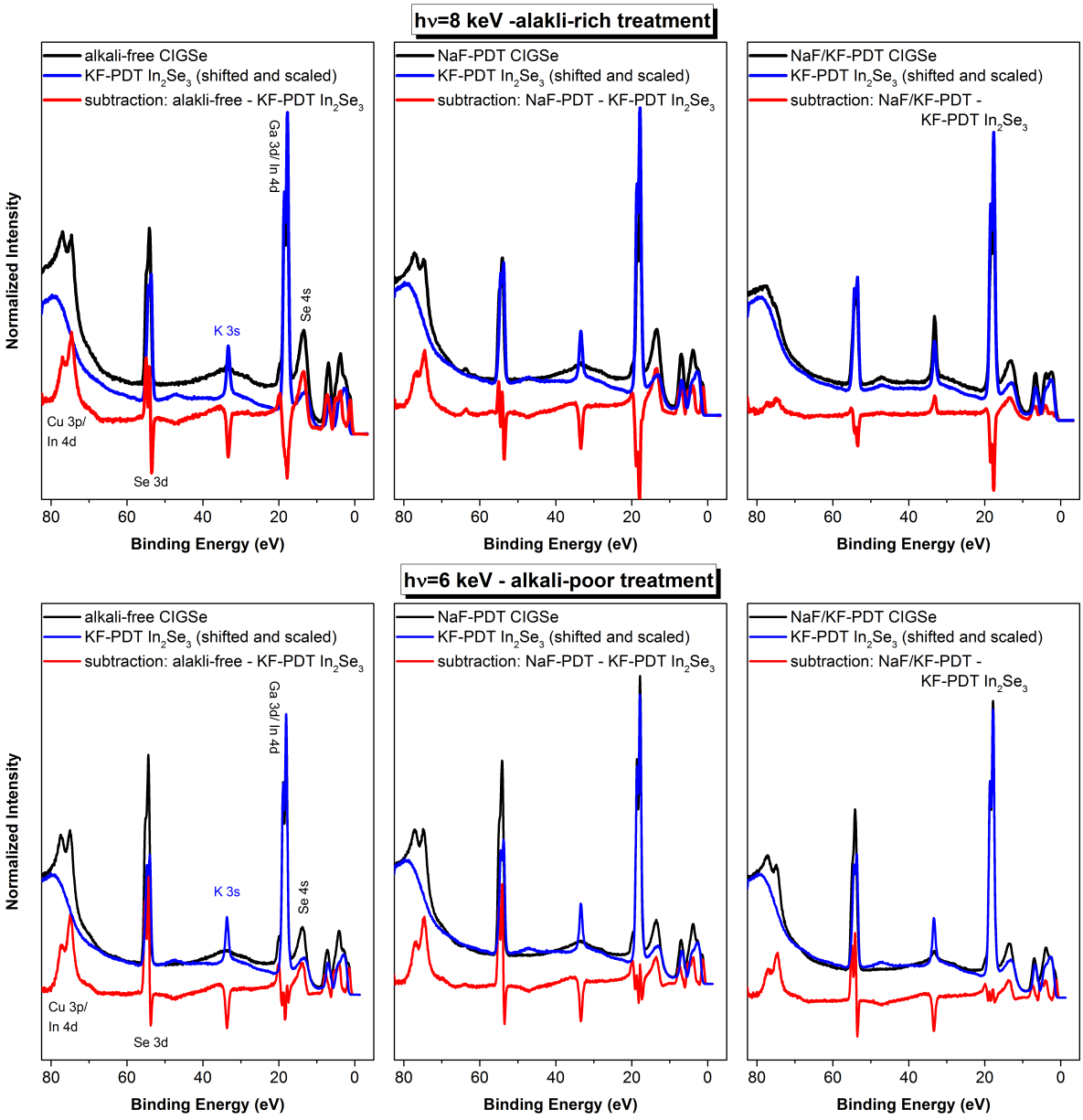

Figure A.3: *The In 4p background correction approach of the Cu 3p line using the KF-PDT In_2Se_3 reference for the differently treated alkali-rich [top] and alkali-poor [bottom] absorbers (alkali-free [left], NaF-PDT [center], and NaF/KF-PDT [right]), measured with excitation energy of hν=8 keV [top] and hν=6 keV [bottom]. The as-measured spectra are shown in black, individually shifted and scaled KF-PDT In_2Se_3 spectra in blue, and the red spectra correspond to the difference of the two.*

A.2 Extended Valence Band Fits

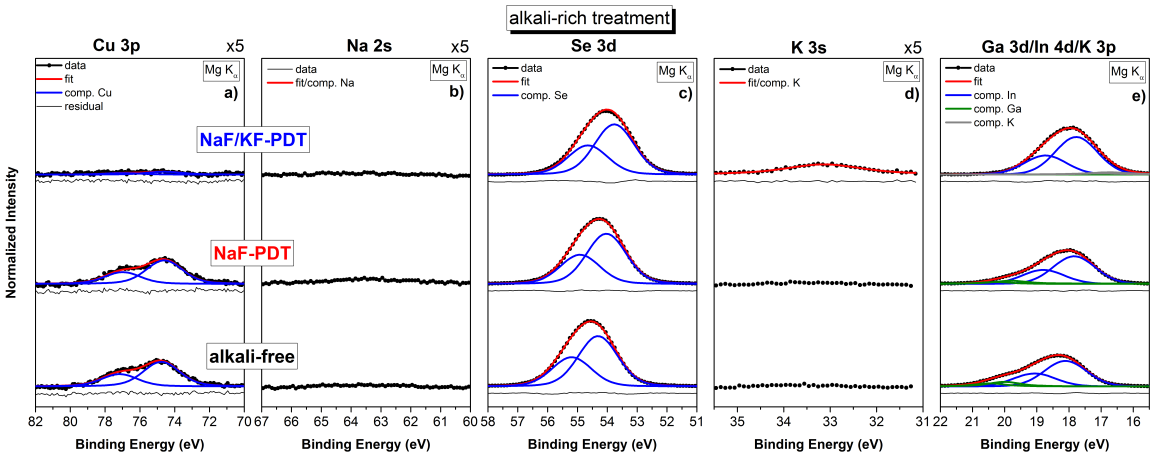

Figure A.4: *Photoemission data with respective Voigt fits of the differently treated absorbers (alkali-free [bottom], NaF-PDT [center], and NaF/KF-PDT [top]): Cu 3p (a), Na 2s (b), Se 3d (b), K 3s (d), and Ga 3d, In 4d, and K 3p (e), measured with an excitation energy of 1253.56 eV (Mg K_α). All spectra are displayed area-normalized to the Se 3d peak area and after subtraction of a linear background. For better visibility, the Cu 3p, Na 2s, and K 3s spectra are magnified by a factor of ×5. For each fit, the residual is shown as well.*

Figures A.4 and A.5 show the shallow core level data simultaneously fitted using Voigt profiles and a linear background. In the leftmost panels (a), the Cu 3p data excited with Mg K_α and 2 keV is shown, together with the corresponding fits and its residual. Lorentzian and Gaussian widths [106] are linked for each excitation energy, and the doublet separation is fixed to 2.39 eV.[107] Panels (b) show the Na 2s peak, which exhibits appreciable intensity only for the alkali-rich NaF-PDT sample measured with 2 keV. Panels (c) display the fits of the Se 3d data using a fixed doublet separation of 0.83 eV.[108] For the alkali-rich NaF/KF-PDT CIGSe sample excited at 2 keV, three species are needed to achieve a satisfactory fit using Voigt profiles of coupled Lorentzian and Gaussian widths. The blue doublet (Se_a) is ascribed to the CIGSe absorber, and the cyan doublet (Se_b) is attributed to the suggested K-In-Se surface species. For 2 keV excitation, the additional orange doublet (Se_c) is most likely the result of surface oxidation of the sample, forming an In-Se-O compound. Panels (d) depict the K 3s spectral region. As expected, potassium can only be detected for both NaF/KF-PDT CIGSe samples. The more pronounced K 3s line observed for 2 keV excitation is indicative of a significant increase of the photoionization cross-section relative to that of the other shallow core level lines. Panels (e) show the fits of the Ga 3d, In 4d, and K 3p

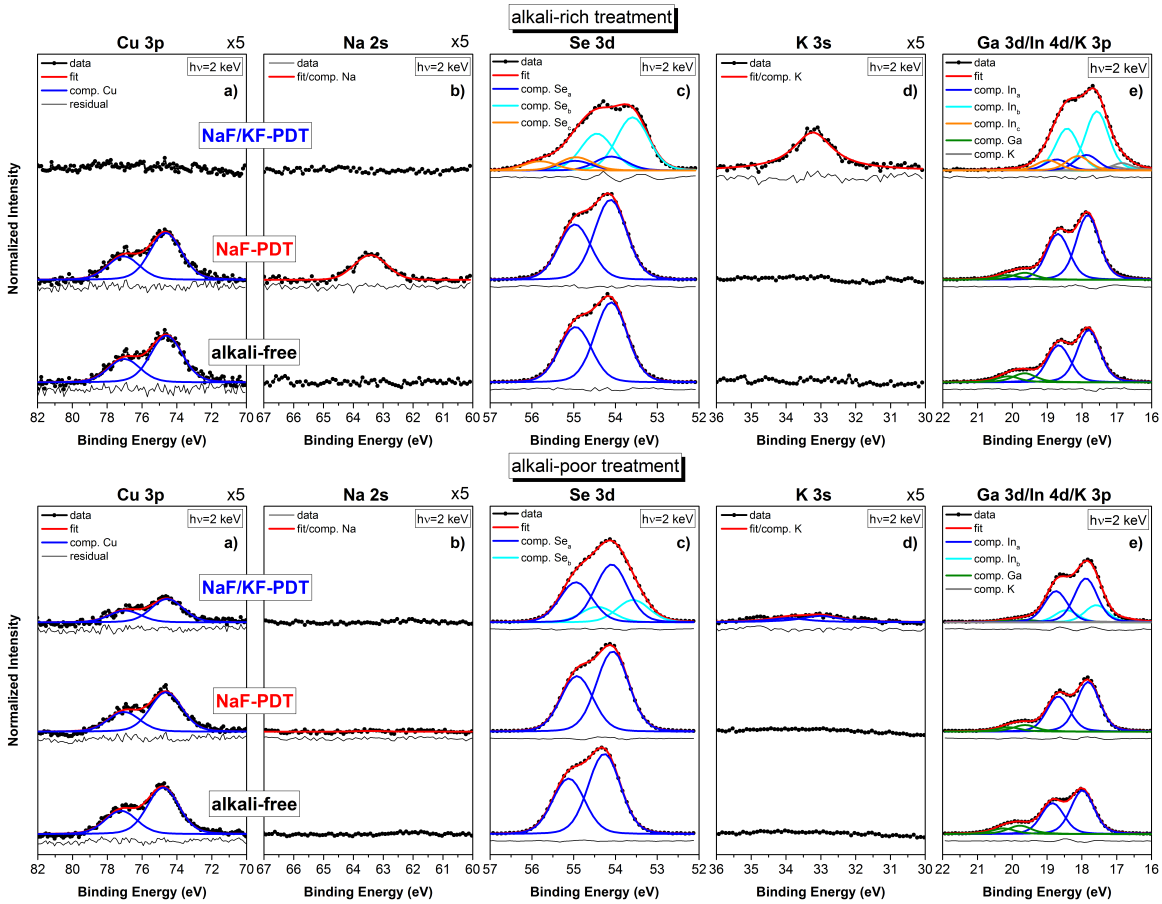

Figure A.5: *Photoemission data with respective Voigt fits of the differently treated absorbers (alkali-free [bottom], NaF-PDT [center], and NaF/KF-PDT [top]): Cu 3p (a), Na 2s (b), Se 3d (b), K 3s (d), and Ga 3d, In 4d, and K 3p (e), measured with an excitation energy of 2 keV for alkali-rich [top panels] and alkali-poor [bottom panels]. All spectra are displayed area-normalized to the Se 3d peak area and after subtraction of a linear background. For better visibility, the Cu 3p, Na 2s, and K 3s spectra are magnified by a factor of ×5. For each fit, the residual is shown as well.*

lines using doublet separations of 0.86 eV for In 4d, [109] 0.46 eV for Ga 3d, [110] and 0.25 eV for K 3p.[111] For the alkali-rich NaF/KF-PDT CIGSe surface, no or only a very weak Ga 3d signal is found. Nevertheless, the Ga 3d line was included in the fit by fixing its position to that of the alkali-rich NaF-PDT CIGSe sample. To describe the In 4d line of the alkali-rich NaF/KF-PDT CIGSe sample, three species are necessary for a reasonable fit. The blue doublet (In_a) is ascribed to (the underlying) CIGSe material, and the cyan doublet (In_b) represents the K-In-Se – type surface layer. The orange doublet (In_c) is most likely the

result of surface oxidation of the sample, forming an In-Se-O compound. The ratio of the intensities of the In_a and In_b components is the same as the one of the Se_a and Se_b components for the respective excitation energy. For the fit, the weak K 3p line is linked in area and position to the K 3s signal using the respective cross-section ratio and the difference in binding energy of the K 3s (E_B=34.70 eV [112]) and K $3p_{3/2}$ (E_B=18.34 eV [111]) line of 16.36 eV.

A.3 Cu Estimation alkali-rich NaF/KF-PDT CIGSe for hν=2 keV

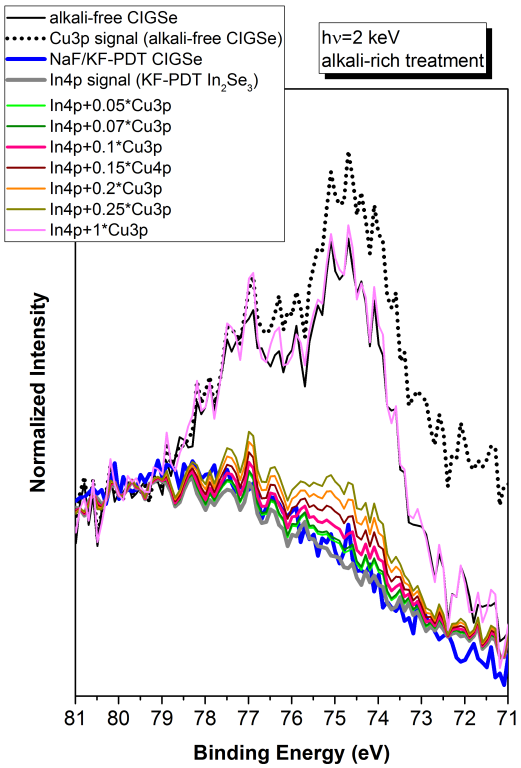

Figure A.6: *Estimation of the Cu 3p contribution in the alkali-rich NaF/KF-PDT sample (blue) using the Cu 3p signal of the alkali-free sample (black) and the In 4p signal of the KF-PDT In_2Se_3 sample (gray). Different ratios of Cu 3p are added to the In 4p signal.*

Figure A.6 shows the estimation of the Cu 3p contribution in the alkali-rich NaF/KF-PDT sample (blue). The signal-to-noise ratio is too low for the NaF/KF-PDT sample to subtract a meaningful In 4p background as was done according to Appendix A.1. However, a noticeable Cu 2p signal is detected for that sample. Therefore, the Cu 3p signal of the alkali-free sample (black), i.e., without the In 4p background (see Appendix A.1), and the In 4p signal of the KF-PDT In_2Se_3 sample (gray) is used for estimating the Cu contribution of the NaF/KF-PDT sample.
The Cu 3p signal has to be less than 0.1 of the Cu 3p (pink spectra) of the respective alkali-free sample. A higher amount of Cu would have been already visible in the spectra. This value is then used for further calculations.

A.4 Artificial HAXPES-derived XES Spectra

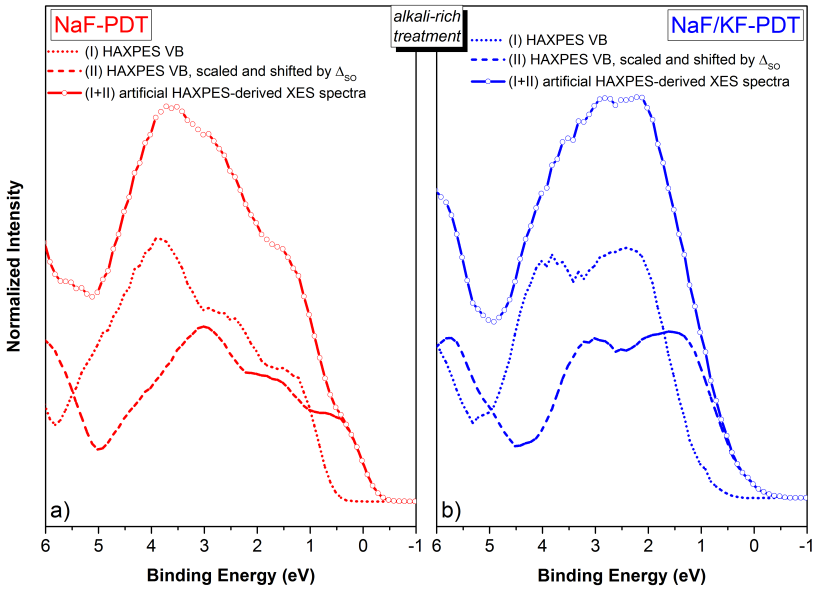

Figure A.7: *8 keV HAXPES valence band (VB) spectra of alkali-rich NaF-PDT (a) and NaF/KF-PDT (b) CIGSe absorbers (I). Spectra (II) represent the same spectra but scaled down by a factor of 2/3 due to $3d_{3/2} - 3d_{5/2}$ multiplicity and shifted by the Se 3d doublet separation Δ_{SO}. The sum of spectra (I) and (II) are then considered to be the corresponding "artificial HAXPES-derived XES spectra."*

Figure A.7 shows the superposition of two 8 keV photoemission valence band spectra for alkali-rich NaF-PDT and NaF/KF-PDT CIGSe that have been offset by the Se $3d_{3/2}$ and $3d_{5/2}$ doublet separation of 0.83 eV [108] and scaled according to the multiplicity (2j+1). The superposition is considered to represent an "artificial HAXPES-derived XES spectra."

A.5 VBM alkali-free CIGSe

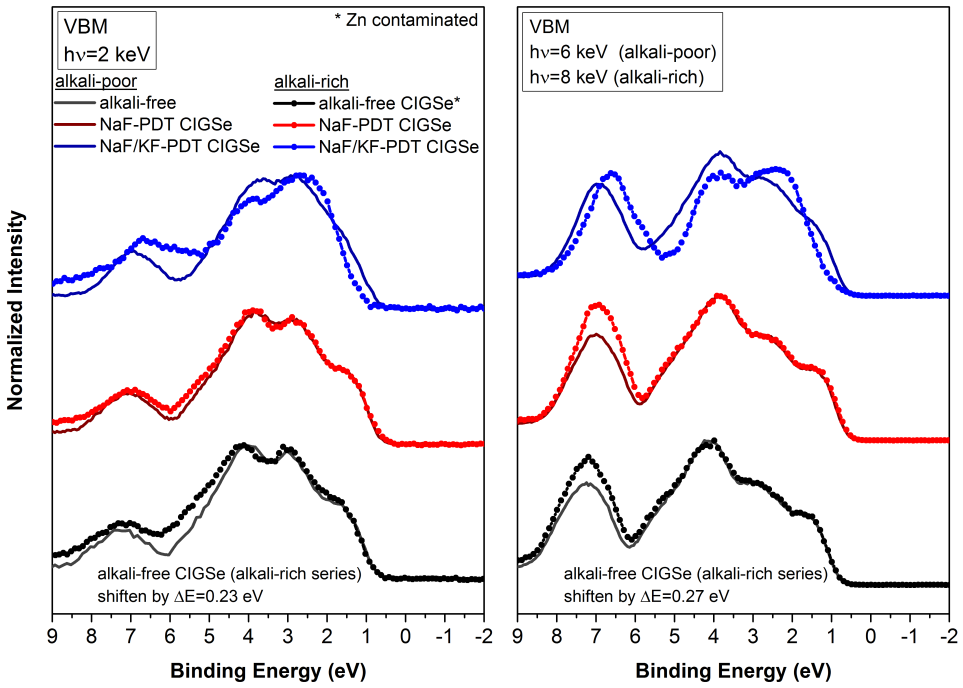

Figure A.8: *Comparison of the valence band region including the valence band maximum for the differently treated alkali-rich absorbers (alkali-free [dotted black], NaF-PDT [dotted red], and NaF/KF-PDT [dotted blue]) and alkali-poor absorbers (alkali-free [gray], NaF-PDT [brown], and NaF/KF-PDT [dark blue]), measured with excitation energies of hν=2 keV [left] and hν=6/8 keV [right]. The alkali-free absorber of the alkali-rich series exhibits Zn contamination.*

Figure A.8 shows the valence band region including the valence band maximum of the two different absorber series with an alkali-rich and an alkali-poor treatment for excitation energies of hν=2 keV and 6/8 keV. For those excitation energies the alkali-free absorber of the alkali-rich series (dotted black) exhibits minor Zn contamination (Zn:Cu ratio about 5%) and

therefore a shift to lower binding energies.
To use a more meaningful value for the VBM of the contaminated alkali-free absorber the spectra is shifted by ΔE=0.23 eV for 2 keV and 0.27 eV for 8 keV, respectively, to overlap with the alkali-free absorber of the alkali-poor series. Therefore, due to the almost exact spectral similarity it seems legitimate to employ the derived VBM values of the alkali-free sample from the alkali-poor series for the contaminated alkali-free sample.

A.6 Rinsing Procedure for $CH_3NH_3PbI_{(3-x)}Cl_x$ on compact TiO_2

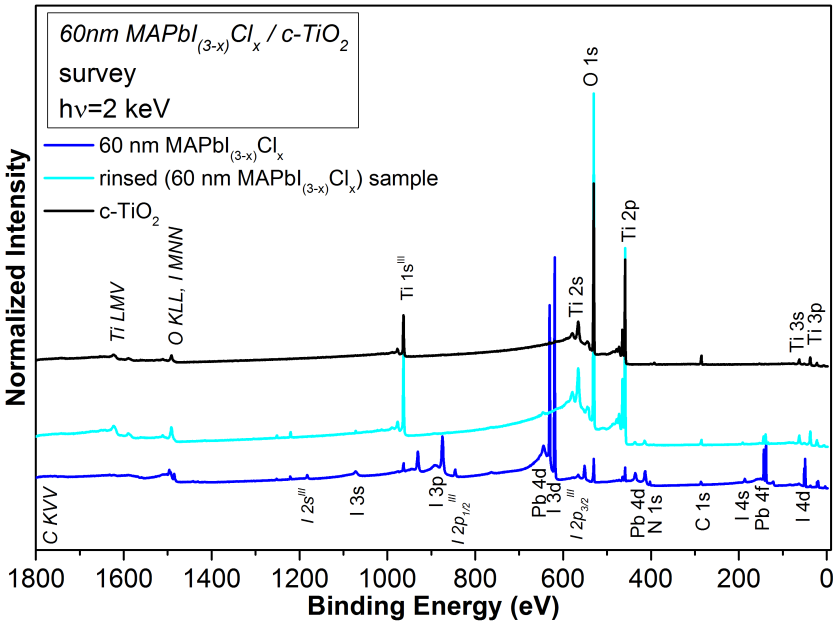

Figure A.9: *Survey spectra of bare compact TiO_2 (c-TiO_2) as substrate material (black), 60 nm $CH_3NH_3PbI_{(3-x)}Cl_x$ (blue) on top of c-TiO_2 and the 60 nm $CH_3NH_3PbI_{(3-x)}Cl_x$ rinsed (cyan) using DMF measured with an excitation energy of hν=2 keV. The core level and Auger lines are marked. Vertical offset added for clarity.*

Figure A.10 shows the survey spectra of the bare c-TiO_2 substrate (black) and a 60 nm $CH_3NH_3PbI_{(3-x)}Cl_x$ sample (blue) on c-TiO_2 also prepared according to the description in chapter 2.2.2. The perovskite layer was rinsed with DMF revealing the remnants and possible formations directly at the TiO_2 interface. After the rinsing procedure mainly Pb, Ti, O, and C are left. However, taking a closer look at selected core levels shown in Figure A.10

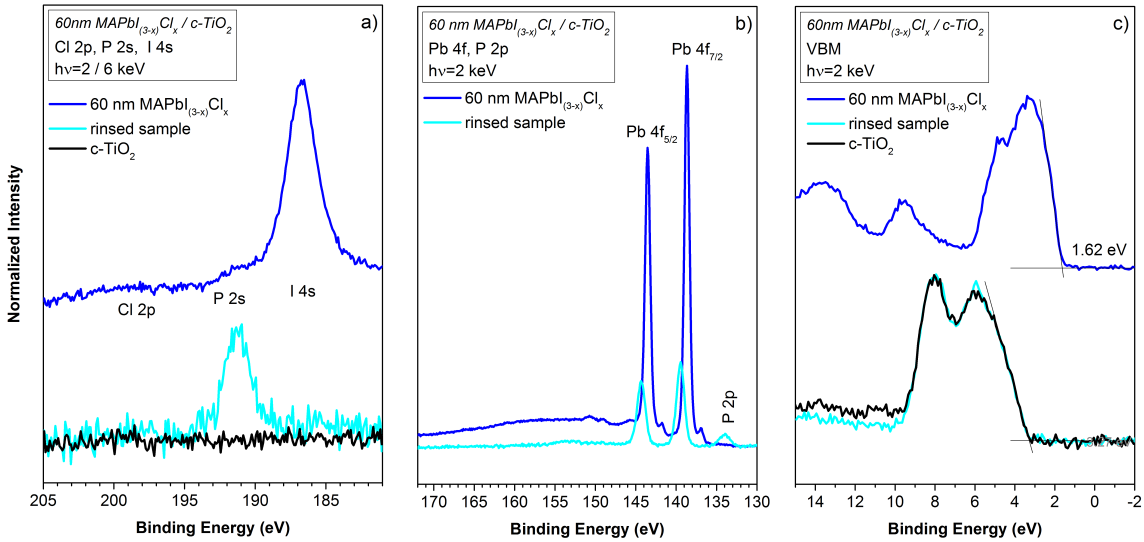

Figure A.10: *a) Cl 2p, P 2s, and I 4s core level region of bare compact TiO_2 (c-TiO_2) as substrate material (black), 60 nm $CH_3NH_3PbI_{(3-x)}Cl_x$ (blue) on top of c-TiO_2 and the 60 nm $CH_3NH_3PbI_{(3-x)}Cl_x$ rinsed (cyan) using DMF measured with an excitation energy of hν=2 keV. Panel b) shows the Pb 4f and P 2p region of the 60 nm $MAPbI_{(3-x)}Cl_x$ sample before and after the rinsing procedure and c) displays the VBM of the three samples.*

it clearly can be seen that due to rinsing phosphorous is introduced (see Figure A.10a,b). After rinsing no detectable amount of iodine is present. The Pb 4f peaks are shifted to higher binding energies indicating Pb-Ti bonds. Further, the VBM of the rinsed sample is identical to the c-TiO_2 one.

A.7 Comparison compact TiO_2 and mesoporous TiO_2

Figure A.11 shows the comparison of the Ti 2p and O 1s core level of the mp-TiO_2 and the c-TiO_2 as well as the O KLL Auger line. All three lines show no difference in spectral shape. However, in all three cases the spectra of the mp-TiO_2 sample is shifted to higher binding energies or lower kinetic energy of about $\Delta E \sim 0.2$ eV, respectively. Nevertheless, no additional species due to different Ti oxidation states, OH and/or H_2O is present.

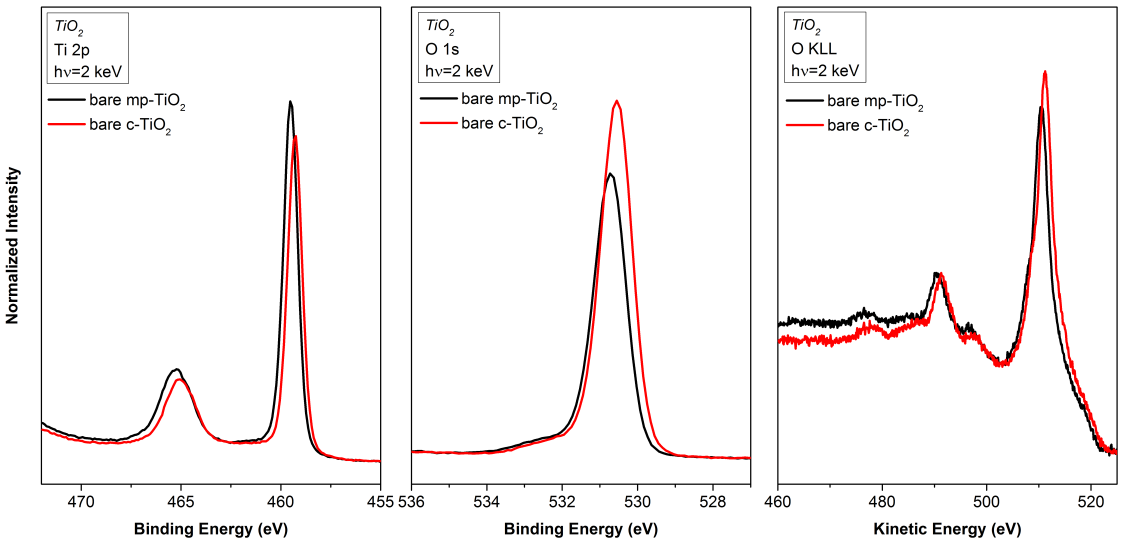

Figure A.11: *Photoemission data of the Ti 2p [left], O 1s [center] lines, and O KLL Auger line [right] of the bare mesoporous TiO_2 (mp-TiO_2, black) and compact TiO_2 (c-TiO_2, red) sample.*

A.8 Cl 2p, P 2s, and I 4s fits on compact TiO_2 and mesoporous TiO_2

Figure A.12 shows the core level data (Cl 2p, P 2s, and I 4s) simultaneously fitted using Voigt profiles and a linear background excited with hν=2 keV, together with the corresponding fits and its residual. Lorentzian and Gaussian widths [106] are linked for each excitation energy. The doublet separation of Cl 2p is 1.72 eV.
The fits are used to calculated the respective Cl:I and P:I ratios toghether with the respective photoionization cross-sections.[84, 85]

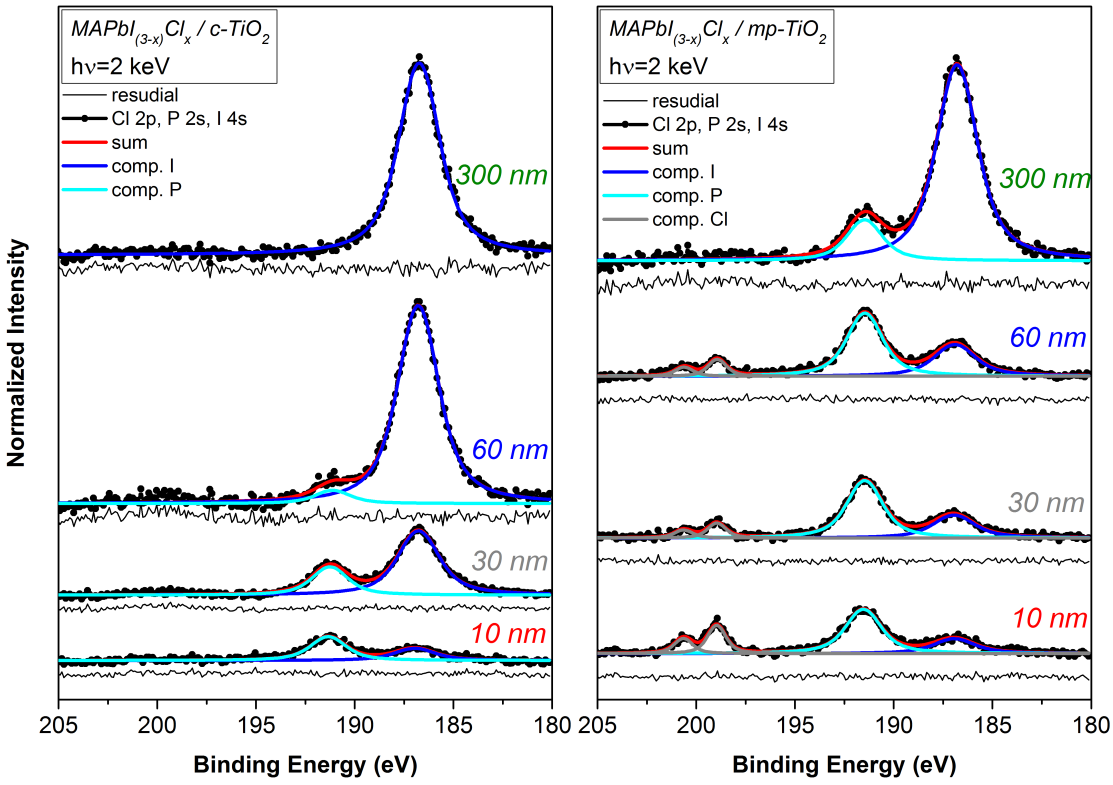

Figure A.12: *Photoemission data with respective Voigt fits of the differently treated absorbers 10, 30, 60, and 300 nm $MAPbI_{(3-x)}Cl_x$ on compact TiO_2 [left] and mesoporous TiO_2 [right]: Cl 2p, P 2s, and I 4s measured with an excitation energy of 2 keV. All spectra are displayed after subtraction of a linear background. For each fit, the residual is shown as well.*

Bibliography

[1] P. Jackson, R. Wuerz, D. Hariskos, E. Lotter, W. Witte, and M. Powalla, "Effects of heavy alkali elements in Cu(In,Ga)Se_2 solar cells with efficiencies up to 22.6%", physica status solidi (RRL) – Rapid Research Letters **10**, 583–586 (2016).

[2] R. Kamada, T. Yagioka, S. Adachi, A. Handa, K. F. Tai, T. Kato, and H. Sugimoto, "New world record Cu(In,Ga)(Se,S)$_2$ thin film solar cell efficiency beyond 22%", in 2016 IEEE 43rd photovoltaic specialists conference (PVSC) (June 2016), pp. 1287–1291.

[3] *NREL efficiency chart*, `http://www.nrel.gov/pv/assets/images/efficiency_chart.jpg` (visited on 10/31/2016).

[4] A. Chirilă, P. Reinhard, F. Pianezzi, P. Bloesch, A. R. Uhl, C. Fella, L. Kranz, D. Keller, C. Gretener, H. Hagendorfer, D. Jaeger, R. Erni, S. Nishiwaki, S. Buecheler, and A. N. Tiwari, "Potassium-induced surface modification of Cu(In,Ga)Se_2 thin films for high-efficiency solar cells", Nature Materials **12**, 1107–1111 (2013).

[5] D. Herrmann, P. Kratzert, S. Weeke, M. Zimmer, J. Djordjevic-Reiss, R. Hunger, P. Lindberg, E. Wallin, O. Lundberg, and L. Stolt, "CIGS module manufacturing with high deposition rates and efficiencies", in Photovoltaic specialist conference (PVSC), 2014 IEEE 40th (June 2014), pp. 2775–2777.

[6] M. Nakamura, N. Yoneyama, K. Horiguchi, Y. Iwata, K. Yamaguchi, H. Sugimoto, and T. Kato, "Recent R&D Progress in Solar Frontier's Small-sized Cu(InGa)(SeS)$_2$ Solar Cells", in 2014 IEEE 40th photovoltaic specialist conference (PVSC) (June 2014), pp. 0107–0110.

[7] P. Jackson, D. Hariskos, R. Wuerz, O. Kiowski, A. Bauer, T. M. Friedlmeier, and M. Powalla, "Properties of Cu(In,Ga)Se_2 solar cells with new record efficiencies up to 21.7%", physica status solidi (RRL) – Rapid Research Letters **9**, 28–31 (2015).

[8] A. Kojima, K. Teshima, Y. Shirai, and T. Miyasaka, "Organometal Halide Perovskites as Visible-Light Sensitizers for Photovoltaic Cells", Journal of the American Chemical Society **131**, 6050–6051 (2009).

[9] M. M. Lee, J. Teuscher, T. Miyasaka, T. N. Murakami, and H. J. Snaith, "Efficient Hybrid Solar Cells Based on Meso-Superstructured Organometal Halide Perovskites", Science **338**, 643–647 (2012).

[10] N. J. Jeon, J. H. Noh, Y. C. Kim, W. S. Yang, S. Ryu, and S. I. Seok, "Solvent engineering for high-performance inorganic–organic hybrid perovskite solar cells", Nature Materials **13**, 897–903 (2014).

[11] J. T.-W. Wang, J. M. Ball, E. M. Barea, A. Abate, J. A. Alexander-Webber, J. Huang, M. Saliba, I. Mora-Sero, J. Bisquert, H. J. Snaith, and R. J. Nicholas, "Low-Temperature Processed Electron Collection Layers of Graphene/TiO_2 Nanocomposites in Thin Film Perovskite Solar Cells", Nano Letters **14**, 724–730 (2014).

[12] K. Wojciechowski, M. Saliba, T. Leijtens, A. Abate, and H. J. Snaith, "Sub-150°C processed meso-superstructured perovskite solar cells with enhanced efficiency", Energy & Environmental Science **7**, 1142–1147 (2014).

[13] G. E. Eperon, V. M. Burlakov, P. Docampo, A. Goriely, and H. J. Snaith, "Morphological Control for High Performance, Solution-Processed Planar Heterojunction Perovskite Solar Cells", Advanced Functional Materials **24**, 151–157 (2014).

[14] H. Zhou, Q. Chen, G. Li, S. Luo, T.-b. Song, H.-S. Duan, Z. Hong, J. You, Y. Liu, and Y. Yang, "Interface engineering of highly efficient perovskite solar cells", Science **345**, 542–546 (2014).

[15] M. Liu, M. B. Johnston, and H. J. Snaith, "Efficient planar heterojunction perovskite solar cells by vapour deposition", Nature **advance online publication** (2013) `10.1038/nature12509`.

[16] Q. Dong, Y. Yuan, Y. Shao, Y. Fang, Q. Wang, and J. Huang, "Abnormal crystal growth in $CH_3NH_3PbI_{3-x}Cl_x$ using a multi-cycle solution coating process", **8**, 2464–2470 (2015).

[17] W. Nie, H. Tsai, R. Asadpour, J.-C. Blancon, A. J. Neukirch, G. Gupta, J. J. Crochet, M. Chhowalla, S. Tretiak, M. A. Alam, H.-L. Wang, and A. D. Mohite, "High-efficiency solution-processed perovskite solar cells with millimeter-scale grains", Science **347**, 522–525 (2015).

[18] S. Albrecht, M. Saliba, J.-P. Correa-Baena, K. Jäger, L. Korte, A. Hagfeldt, M. Grätzel, and B. Rech, "Towards optical optimization of planar monolithic perovskite/silicon-heterojunction tandem solar cells", Journal of Optics **18**, 064012 (2016).

[19] C. D. Bailie, M. G. Christoforo, J. P. Mailoa, A. R. Bowring, E. L. Unger, W. H. Nguyen, J. Burschka, N. Pellet, J. Z. Lee, M. Grätzel, R. Noufi, T. Buonassisi, A. Salleo, and M. D. McGehee, "Semi-transparent perovskite solar cells for tandems with silicon and CIGS", Energy & Environmental Science **8**, 956–963 (2015).

[20] F. Fu, T. Feurer, T. Jäger, E. Avancini, B. Bissig, S. Yoon, S. Buecheler, and A. N. Tiwari, "Low-temperature-processed efficient semi-transparent planar perovskite solar cells for bifacial and tandem applications", Nature Communications **6**, 8932 (2015).

[21] L. Kranz, A. Abate, T. Feurer, F. Fu, E. Avancini, J. Löckinger, P. Reinhard, S. M. Zakeeruddin, M. Grätzel, S. Buecheler, and A. N. Tiwari, "High-efficiency polycrystalline thin film tandem solar cells", The Journal of Physical Chemistry Letters **6**, 2676–2681 (2015).

[22] C. J. Chen, "Appendix E: AM1.5 Reference Solar Spectrum", in *Physics of solar energy* (John Wiley & Sons, Inc., 2011), pp. 307–312.

[23] L. M. Peter, "Towards sustainable photovoltaics: the search for new materials", Philosophical Transactions of the Royal Society of London A: Mathematical, Physical and Engineering Sciences **369**, 1840–1856 (2011).

[24] W. Shockley and H. J. Queisser, "Detailed Balance Limit of Efficiency of p-n Junction Solar Cells", Journal of Applied Physics **32**, 510–519 (1961).

[25] J. E. Jaffe and A. Zunger, "Electronic structure of the ternary chalcopyrite semiconductors $CuAlS_2$, $CuGaS_2$, $CuInS_2$, $CuAlSe_2$, $CuGaSe_2$, and $CuInSe_2$", Physical Review B **28**, 5822–5847 (1983).

[26] M. Bär, W. Bohne, J. Röhrich, E. Strub, S. Lindner, M. C. Lux-Steiner, C.-H. Fischer, T. P. Niesen, and F. Karg, "Determination of the band gap depth profile of the penternary $Cu(In_{1-X}Ga_X)(S_YSe_{1-Y})_2$ chalcopyrite from its composition gradient", Journal of Applied Physics **96**, 3857–3860 (2004).

[27] M. Gloeckler and J. R. Sites, "Band-gap grading in Cu(In,Ga)Se_2 solar cells", Journal of Physics and Chemistry of Solids, The 14th International Conference on Ternary and Multinary Compounds **66**, 1891–1894 (2005).

[28] A. Chirila, S. Buecheler, F. Pianezzi, P. Bloesch, C. Gretener, A. R. Uhl, C. Fella, L. Kranz, J. Perrenoud, S. Seyrling, R. Verma, S. Nishiwaki, Y. E. Romanyuk, G. Bilger, and A. N. Tiwari, "Highly efficient Cu(In,Ga)Se_2 solar cells grown on flexible polymer films", Nature Materials **10**, 857–861 (2011).

[29] K. Moriwaki, M. Nomoto, S. Yuuya, N. Murakami, T. Ohgoh, K. Yamane, S. Ishizuka, and S. Niki, "Monolithically integrated flexible Cu(In,Ga)Se_2 solar cells and submodules using newly developed structure metal foil substrate with a dielectric layer", Solar Energy Materials and Solar Cells **112**, 106–111 (2013).

[30] M. Morkel, L. Weinhardt, B. Lohmüller, C. Heske, E. Umbach, W. Riedl, S. Zweigart, and F. Karg, "Flat conduction-band alignment at the CdS/$CuInSe_2$ thin-film solar-cell heterojunction", Applied Physics Letters **79**, 4482–4484 (2001).

[31] D. Schmid, M. Ruckh, F. Grunwald, and H. W. Schock, "Chalcopyrite/defect chalcopyrite heterojunctions on the basis of $CuInSe_2$", Journal of Applied Physics **73**, 2902–2909 (1993).

[32] T. Dullweber, G. Hanna, U. Rau, and H. W. Schock, "A new approach to high-efficiency solar cells by band gap grading in Cu(In,Ga)Se_2 chalcopyrite semiconductors", Solar Energy Materials and Solar Cells, PVSEC 11 - PART III **67**, 145–150 (2001).

[33] M. Turcu, O. Pakma, and U. Rau, "Interdependence of absorber composition and recombination mechanism in Cu(In,Ga)$(Se,S)_2$ heterojunction solar cells", Applied Physics Letters **80**, 2598–2600 (2002).

[34] M. B. Zellner, R. W. Birkmire, E. Eser, W. N. Shafarman, and J. G. Chen, "Determination of activation barriers for the diffusion of sodium through CIGS thin-film solar cells", Progress in Photovoltaics: Research and Applications **11**, 543–548 (2003).

[35] A. Rockett, K. Granath, S. Asher, M. M. Al Jassim, F. Hasoon, R. Matson, B. Basol, V. Kapur, J. S. Britt, T. Gillespie, and C. Marshall, "Na incorporation in Mo and $CuInSe_2$ from production processes", Solar Energy Materials and Solar Cells **59**, 255–264 (1999).

[36] C. Heske, R. Fink, E. Umbach, W. Riedl, and F. Karg, "Na-induced effects on the electronic structure and composition of Cu(In,Ga)Se_2 thinfilm surfaces", Applied Physics Letters **68**, 3431–3433 (1996).

[37] X. Song, R. Caballero, R. Félix, D. Gerlach, C. A. Kaufmann, H.-W. Schock, R. G. Wilks, and M. Bär, "Na incorporation into Cu(In,Ga)Se_2 thin-film solar cell absorbers deposited on polyimide: Impact on the chemical and electronic surface structure", Journal of Applied Physics **111**, 034903 (2012).

[38] M. Lammer, U. Klemm, and M. Powalla, "Sodium co-evaporation for low temperature Cu(In,Ga)Se_2 deposition", Thin Solid Films, Proceeedings of Symposium N on Thin Film Photovoltaicmaterials of the E-MRS Spring Conference **387**, 33–36 (2001).

[39] T. Nakada, D. Iga, H. Ohbo, and A. Kunioka, "Effects of Sodium on Cu(In,Ga)Se_2-Based Thin Films and Solar Cells", Japanese Journal of Applied Physics **36**, 732 (1997).

[40] D. Rudmann, A. F. d. Cunha, M. Kaelin, F. Kurdesau, H. Zogg, A. N. Tiwari, and G. Bilger, "Efficiency enhancement of Cu(In,Ga)Se_2 solar cells due to post-deposition Na incorporation", Applied Physics Letters **84**, 1129–1131 (2004).

[41] R. Wuerz, A. Eicke, F. Kessler, S. Paetel, S. Efimenko, and C. Schlegel, "CIGS thin-film solar cells and modules on enamelled steel substrates", Solar Energy Materials and Solar Cells, Photovoltaics, Solar Energy Materials, and Technologies: Cancun 2010 **100**, 132–137 (2012).

[42] P. Pistor, D. Greiner, C. A. Kaufmann, S. Brunken, M. Gorgoi, A. Steigert, W. Calvet, I. Lauermann, R. Klenk, T. Unold, and M.-C. Lux-Steiner, "Experimental indication for band gap widening of chalcopyrite solar cell absorbers after potassium fluoride treatment", Applied Physics Letters **105**, 063901 (2014).

[43] A. Laemmle, R. Wuerz, and M. Powalla, "Efficiency enhancement of Cu(In,Ga)Se_2 thin-film solar cells by a post-deposition treatment with potassium fluoride", physica status solidi (RRL) – Rapid Research Letters **7**, 631–634 (2013).

[44] A. Laemmle, R. Wuerz, and M. Powalla, "Investigation of the effect of potassium on Cu(In,Ga)Se_2 layers and solar cells", Thin Solid Films, E-MRS 2014 Spring Meeting, Symposium A, Thin-Film Chalcogenide Photovoltaic Materials **582**, 27–30 (2015).

[45] D. Rudmann, D. Brémaud, A. F. da Cunha, G. Bilger, A. Strohm, M. Kaelin, H. Zogg, and A. N. Tiwari, "Sodium incorporation strategies for CIGS growth at different temperatures", Thin Solid Films, EMRS 2004Proceedings of Symposium O on Thin Film Chalcogenide Photovoltaic Materials, EMRS 2004 Conference, Strasbourg, France, May 24-28, 2004 **480–481**, 55–60 (2005).

[46] D. Hariskos, M. Powalla, N. Chevaldonnet, D. Lincot, A. Schindler, and B. Dimmler, "Chemical bath deposition of CdS buffer layer: prospects of increasing materials yield and reducing waste", Thin Solid Films, Proceeedings of Symposium N on Thin Film Photovoltaicmaterials of the E-MRS Spring Conference **387**, 179–181 (2001).

[47] H. S. Jung and N.-G. Park, "Perovskite Solar Cells: From Materials to Devices", Small **11**, 10–25 (2015).

[48] B. O'Regan and M. Grätzel, "A low-cost, high-efficiency solar cell based on dye-sensitized colloidal TiO_2 films", Nature **353**, 737–740 (1991).

[49] *EPFL achieves 21% efficiency - 2015-12-08*, `http://www.dyesol.com/media/wysiwyg/Documents/2015-asx-announcements/2015-12-08-DYE0397_-_EPFL_achieves_21_efficiency.pdf` (visited on 03/30/2016).

[50] D. Weber, "$CH_3NH_3PbX_3$, ein Pb(II)-System mit kubischer Perowskitstruktur / $CH_3NH_3PbX_3$, a Pb(II)-System with Cubic Perovskite Structure", Zeitschrift für Naturforschung B **33**, 1443–1445 (2014).

[51] S. D. Stranks, G. E. Eperon, G. Grancini, C. Menelaou, M. J. P. Alcocer, T. Leijtens, L. M. Herz, A. Petrozza, and H. J. Snaith, "Electron-Hole Diffusion Lengths Exceeding 1 Micrometer in an Organometal Trihalide Perovskite Absorber", Science **342**, 341–344 (2013).

[52] S. Colella, E. Mosconi, P. Fedeli, A. Listorti, F. Gazza, F. Orlandi, P. Ferro, T. Besagni, A. Rizzo, G. Calestani, G. Gigli, F. De Angelis, and R. Mosca, "$MAPbI_{3-x}Cl_x$ Mixed Halide Perovskite for Hybrid Solar Cells: The Role of Chloride as Dopant on the Transport and Structural Properties", Chemistry of Materials **25**, 4613–4618 (2013).

[53] J. Liu and O. V. Prezhdo, "Chlorine Doping Reduces Electron–Hole Recombination in Lead Iodide Perovskites: Time-Domain Ab Initio Analysis", The Journal of Physical Chemistry Letters **6**, 4463–4469 (2015).

[54] H. Yu, F. Wang, F. Xie, W. Li, J. Chen, and N. Zhao, "The Role of Chlorine in the Formation Process of "$CH_3NH_3PbI_{3-x}Cl_x$" Perovskite", Advanced Functional Materials **24**, 7102–7108 (2014).

[55] R. Lindblad, D. Bi, B.-w. Park, J. Oscarsson, M. Gorgoi, H. Siegbahn, M. Odelius, E. M. J. Johansson, and H. Rensmo, "Electronic Structure of TiO_2/$CH_3NH_3PbI_3$ Perovskite Solar Cell Interfaces", The Journal of Physical Chemistry Letters **5**, 648–653 (2014).

[56] P. Schulz, E. Edri, S. Kirmayer, G. Hodes, D. Cahen, and A. Kahn, "Interface energetics in organo-metal halide perovskite-based photovoltaic cells", Energy & Environmental Science **7**, 1377–1381 (2014).

[57] E. Edri, S. Kirmayer, S. Mukhopadhyay, K. Gartsman, G. Hodes, and D. Cahen, "Elucidating the charge carrier separation and working mechanism of $CH_3NH_3PbI_{3-x}Cl_x$ perovskite solar cells", Nature Communications **5**, 3461 (2014).

[58] J. M. Ball, M. M. Lee, A. Hey, and H. J. Snaith, "Low-temperature processed meso-superstructured to thin-film perovskite solar cells", Energy & Environmental Science **6**, 1739–1743 (2013).

[59] J. Burschka, N. Pellet, S.-J. Moon, R. Humphry-Baker, P. Gao, M. K. Nazeeruddin, and M. Grätzel, "Sequential deposition as a route to high-performance perovskite-sensitized solar cells", Nature **499**, 316–319 (2013).

[60] H. Hertz, "Ueber einen Einfluss des ultravioletten Lichtes auf die electrische Entladung", Annalen der Physik **267**, 983–1000 (1887).

[61] W. Hallwachs, "Über den Einfluss des Lichtes auf electrostatisch geladene Körper", Annalen der Physik **269**, 301–312 (1888).

[62] A. Einstein, "Über einen die Erzeugung und Verwandlung des Lichtes betreffenden heuristischen Gesichtspunkt [AdP 17, 132 (1905)]", Annalen der Physik **14**, 164–181 (2005).

[63] S. Hüfner, *Photoelectron Spectroscopy* (Springer-Verlag, 1995).

[64] F. Reinert and S. Hüfner, "Photoemission spectroscopy - from early days to recent applications", New Journal of Physics **7**, 97 (2005).

[65] D. Briggs and M. P. Seah, *Auger and X-Ray Photoelectron Spectroscopy: Practical Surface Analysis* (John Wiley & Sons, Chichester, 1983), 533 pp.

[66] J. H. Hubbell, P. N. Trehan, N. Singh, B. Chand, D. Mehta, M. L. Garg, R. R. Garg, S. Singh, and S. Puri, "A Review, Bibliography, and Tabulation of K, L, and Higher Atomic Shell XRay Fluorescence Yields", Journal of Physical and Chemical Reference Data **23**, 339–364 (1994).

[67] M. O. Krause, "Atomic radiative and radiationless yields for K and L shells", Journal of Physical and Chemical Reference Data **8**, 307–327 (1979).

[68] M. O. Krause and J. H. Oliver, "Natural widths of atomic K and L levels, Kα Xray lines and several KLL Auger lines", Journal of Physical and Chemical Reference Data **8**, 329–338 (1979).

[69] C. D. Wagner, L. H. Gale, and R. H. Raymond, "Two-dimensional chemical state plots: a standardized data set for use in identifying chemical states by x-ray photoelectron spectroscopy", Analytical Chemistry **51**, 466–482 (1979).

[70] C. D. Wagner, "Auger lines in x-ray photoelectron spectrometry", Analytical Chemistry **44**, 967–973 (1972).

[71] C. D. Wagner, "Auger parameter in electron spectroscopy for the identification of chemical species", Analytical Chemistry **47**, 1201–1203 (1975).

[72] G. Moretti, "Auger parameter and Wagner plot in the characterization of chemical states by X-ray photoelectron spectroscopy: a review", Journal of Electron Spectroscopy and Related Phenomena **95**, 95–144 (1998).

[73] C. D. Wagner and A. Joshi, "The auger parameter, its utility and advantages: a review", Journal of Electron Spectroscopy and Related Phenomena **47**, 283–313 (1988).

[74] N. V. Smith, "Inverse photoemission", Reports on Progress in Physics **51**, 1227 (1988).

[75] N. V. Smith and D. P. Woodruff, "Inverse photoemission from metal surfaces", Progress in Surface Science **21**, 295–370 (1986).

[76] V. Dose, "Momentum-resolved inverse photoemission", Surface Science Reports **5**, 337–378 (1985).

[77] D. Abou-Ras, T. Kirchartz, and U. Rau, *Advanced Characterization Techniques for Thin Film Solar Cells* (WILEY-VCH Verlag GmbH & Co. KGaA, Weinheim, 2011), 547 pp.

[78] M. P. Seah and W. A. Dench, "Quantitative electron spectroscopy of surfaces: A standard data base for electron inelastic mean free paths in solids", Surface and Interface Analysis **1**, 2–11 (1979).

[79] S. Tanuma, C. J. Powell, and D. R. Penn, "Calculations of electron inelastic mean free paths. V. Data for 14 organic compounds over the 50-2000 eV range", Surface and Interface Analysis **21**, 165–176 (1994).

[80] E. Handick, P. Reinhard, J.-H. Alsmeier, L. Köhler, F. Pianezzi, S. Krause, M. Gorgoi, E. Ikenaga, N. Koch, R. G. Wilks, S. Buecheler, A. N. Tiwari, and M. Bär, "Potassium Postdeposition Treatment-Induced Band Gap Widening at Cu(In,Ga)Se_2 Surfaces - Reason for Performance Leap?", ACS Applied Materials & Interfaces **7**, 27414–27420 (2015).

[81] M. Bär, L. Weinhardt, O. Fuchs, J. Klaer, J. Peiser, H. W. Schock, and C. Heske, "Chemical Bath Deposition of CdS Thin Films on $CuInS_2$ and Si Substrates - A Comparative X-Ray Emission Study", in 2006 IEEE 4th world conference on photovoltaic energy conference, Vol. 1 (May 2006), pp. 416–419.

[82] B. L. Henke, E. M. Gullikson, and J. C. Davis, "X-Ray Interactions: Photoabsorption, Scattering, Transmission, and Reflection at E = 50-30,000 eV, Z = 1-92", Atomic Data and Nuclear Data Tables **54**, 181–342 (1993).

[83] *X-ray attenuation length*, `http://henke.lbl.gov/optical_constants/atten2.html` (visited on 10/30/2016).

[84] M. B. Trzhaskovskaya, V. I. Nefedov, and V. G. Yarzhemsky, "Photoelectron Angular Distribution Parameters for Elements Z=1 to Z=54 in the Photoelectron Energy Range 100-5000 eV", Atomic Data and Nuclear Data Tables **77**, 97–159 (2001).

[85] M. B. Trzhaskovskaya, V. I. Nefedov, and V. G. Yarzhemsky, "Photoelectron Angular Distribution Parameters for Elements Z=55 to Z=100 in the Photoelectron Energy Range 100-5000 eV", Atomic Data and Nuclear Data Tables **82**, 257–311 (2002).

[86] M. B. Trzhaskovskaya, V. K. Nikulin, V. I. Nefedov, and V. G. Yarzhemsky, "Nondipole second order parameters of the photoelectron angular distribution for elements Z = 1–100 in the photoelectron energy range 1–10 keV", Atomic Data and Nuclear Data Tables **92**, 245–304 (2006).

[87] D. Eich, K. Ortner, U. Groh, Z. H. Chen, C. R. Becker, G. Landwehr, R. Fink, and E. Umbach, "Band Discontinuity and Band Gap of MBE Grown HgTe/CdTe(001) Heterointerfaces Studied by k-Resolved Photoemission and Inverse Photoemission", physica status solidi (a) **173**, 261–267 (1999).

[88] T. Gleim, C. Heske, E. Umbach, C. Schumacher, W. Faschinger, C. Ammon, M. Probst, and H.-P. Steinrück, "Reduction of the ZnSe/GaAs(100) valence band offset by a Te interlayer", Applied Physics Letters **78**, 1867–1869 (2001).

[89] T. Gleim, C. Heske, E. Umbach, C. Schumacher, S. Gundel, W. Faschinger, A. Fleszar, C. Ammon, M. Probst, and H.-P. Steinrück, "Formation of the ZnSe/ (Te/) GaAs (1 0 0) heterojunction", Surface Science **531**, 77–85 (2003).

[90] J. R. Waldrop, R. W. Grant, S. P. Kowalczyk, and E. A. Kraut, "Measurement of semiconductor heterojunction band discontinuities by xray photoemission spectroscopy", Journal of Vacuum Science & Technology A **3**, 835–841 (1985).

[91] D. Briggs and M. P. Seah, *Auger and X-Ray Photoelectron Spectroscopy: Practical Surface Analysis (Appendix 1)* (John Wiley & Sons, Chichester, 1983), 533 pp.

[92] D. Attwood, *Soft x-ray and extreme ultraviolet radiation - principles and applications* (Cambridge University Press, 1999).

[93] M. Gorgoi, S. Svensson, F. Schäfers, G. Öhrwall, M. Mertin, P. Bressler, O. Karis, H. Siegbahn, A. Sandell, H. Rensmo, W. Doherty, C. Jung, W. Braun, and W. Eberhardt, "The high kinetic energy photoelectron spectroscopy facility at BESSY progress and first results", Nuclear Instruments and Methods in Physics Research Section A: Accelerators, Spectrometers, Detectors and Associated Equipment, Special issue in honour of Prof. Kai Siegbahn **601**, 48–53 (2009).

[94] F. Schaefers, M. Mertin, and M. Gorgoi, "KMC-1: A high resolution and high flux soft x-ray beamline at BESSY", Review of Scientific Instruments **78**, 123102 (2007).

[95] S. Ueda, Y. Katsuya, M. Tanaka, H. Yoshikawa, Y. Yamashita, S. Ishimaru, Y. Matsushita, and K. Kobayashi, "Present Status of the NIMS Contract Beamline BL15XU at SPring-8", in AIP conference proceedings, Vol. 1234 (June 23, 2010), pp. 403–406.

[96] S. Ueda, "Application of hard X-ray photoelectron spectroscopy to electronic structure measurements for various functional materials", Journal of Electron Spectroscopy and Related Phenomena, Recent advances in Hard X-ray Photoelectron Spectroscopy (HAXPES) **190, Part B**, 235–241 (2013).

[97] E. Ikenaga, M. Kobata, H. Matsuda, T. Sugiyama, H. Daimon, and K. Kobayashi, "Development of high lateral and wide angle resolved hard X-ray photoemission spectroscopy at BL47XU in SPring-8", Journal of Electron Spectroscopy and Related Phenomena, Recent advances in Hard X-ray Photoelectron Spectroscopy (HAXPES) **190, Part B**, 180–187 (2013).

[98] J. J. Jia, T. A. Callcott, J. Yurkas, A. W. Ellis, F. J. Himpsel, M. G. Samant, J. Stöhr, D. L. Ederer, J. A. Carlisle, E. A. Hudson, L. J. Terminello, D. K. Shuh, and R. C. C. Perera, "First experimental results from IBM/TENN/TULANE/LLNL/LBL undulator beamline at the advanced light source", Review of Scientific Instruments **66**, 1394–1397 (1995).

[99] E. Handick, P. Reinhard, R. G. Wilks, F. Pianezzi, R. Félix, M. Gorgoi, T. Kunze, S. Buecheler, A. N. Tiwari, and M. Bär, "NaF/KF post-deposition treatments and their influence on the structure of Cu(In,Ga)Se_2 absorber surfaces", in 2016 IEEE 43rd photovoltaic specialists conference (PVSC) (June 2016), pp. 0017–0021.

[100] E. Handick, P. Reinhard, R. G. Wilks, F. Pianezzi, T. Kunze, D. Kreikemeyer-Lorenzo, L. Weinhardt, M. Blum, W. Yang, M. Gorgoi, E. Ikenaga, D. Gerlach, S. Ueda, Y. Yamashita, T. Chikyow, C. Heske, S. Buecheler, A. N. Tiwari, and M. Bär, "Formation of a K—In—Se Surface Species by NaF/KF Postdeposition Treatment of Cu(In,Ga)Se_2 Thin-Film Solar Cell Absorbers", ACS Applied Materials & Interfaces **9**, 3581–3589 (2017).

[101] P. Reinhard, B. Bissig, F. Pianezzi, H. Hagendorfer, G. Sozzi, R. Menozzi, C. Gretener, S. Nishiwaki, S. Buecheler, and A. N. Tiwari, "Alkali-Templated Surface Nanopatterning of Chalcogenide Thin Films: A Novel Approach Toward Solar Cells with Enhanced Efficiency", Nano Letters **15**, 3334–3340 (2015).

[102] P. Reinhard, B. Bissig, F. Pianezzi, E. Avancini, H. Hagendorfer, D. Keller, P. Fuchs, M. Döbeli, C. Vigo, P. Crivelli, S. Nishiwaki, S. Buecheler, and A. N. Tiwari, "Features of KF and NaF Postdeposition Treatments of Cu(In,Ga)Se_2 Absorbers for High Efficiency Thin Film Solar Cells", Chemistry of Materials **27**, 5755–5764 (2015).

[103] L. L. Kazmerski, O. Jamjoum, P. J. Ireland, S. K. Deb, R. A. Mickelsen, and W. Chen, "Initial oxidation of $CuInSe_2$", Journal of Vacuum Science & Technology **19**, 467–471 (1981).

[104] D. Cahen, P. J. Ireland, L. L. Kazmerski, and F. A. Thiel, "Xray photoelectron and Auger electron spectroscopic analysis of surface treatments and electrochemical decomposition of $CuInSe_2$ photoelectrodes", Journal of Applied Physics **57**, 4761–4771 (1985).

[105] R. Würz, M. Rusu, T. Schedel-Niedrig, M. C. Lux-Steiner, H. Bluhm, M. Hävecker, E. Kleimenov, A. Knop-Gericke, and R. Schlögl, "In situ X-ray photoelectron spectroscopy study of the oxidation of $CuGaSe_2$", Surface Science **580**, 80–94 (2005).

[106] *Contents — fityk 0.9.4 manual*, `file:///C:/Program%20Files%20(x86)/Fityk/html/fityk-manual.html` (visited on 07/27/2016).

[107] A. Lebugle, U. Axelsson, R. Nyholm, and N. Mårtensson, "Experimental L and M Core Level Binding Energies for the Metals 22 Ti to 30 Zn", Physica Scripta **23**, 825 (1981).

[108] N. J. Shevchik, M. Cardona, and J. Tejeda, "X-Ray and Far-uv Photoemission from Amorphous and Crystalline Films of Se and Te", Physical Review B **8**, 2833–2841 (1973).

[109] R. T. Poole, P. C. Kemeny, J. Liesegang, J. G. Jenkin, and R. C. G. Leckey, "High resolution photoelectron studies of the d bands of some metals", Journal of Physics F: Metal Physics **3**, L46 (1973).

[110] D. M. Poirier and J. H. Weaver, "GaAs(110) by XPS", Surface Science Spectra **2**, 201–208 (1993).

[111] G. K. Wertheim and D. M. Riffe, "Evidence for crystal-field splitting in surface-atom photoemission from potassium", Physical Review B **52**, 14906–14910 (1995).

[112] L.-G. Petersson and S.-E. Karlsson, "Clean and Oxygen Exposed Potassium Studied by Photoelectron Spectroscopy", Physica Scripta **16**, 425–431 (1977).

[113] C. P. Muzzillo, L. M. Mansfield, K. Ramanathan, and T. J. Anderson, "Properties of $Cu_1xK_xInSe_2$ alloys", Journal of Materials Science, 1–12 (2016).

[114] M. Bär, S. Nishiwaki, L. Weinhardt, S. Pookpanratana, O. Fuchs, M. Blum, W. Yang, J. D. Denlinger, W. N. Shafarman, and C. Heske, "Depth-resolved band gap in $Cu(In,Ga)(S,Se)_2$ thin films", Applied Physics Letters **93**, 244103 (2008).

[115] D. Liao and A. Rockett, "Cu depletion at the $CuInSe_2$ surface", Applied Physics Letters **82**, 2829–2831 (2003).

[116] J. Tuttle, D. Albin, and R. Noufi, "Thoughts on the microstructure of polycrystalline thin film $CuInSe_2$ and its impact on material and device performance", Solar Cells **30**, 21–38 (1991).

[117] E. Ghorbani, J. Kiss, H. Mirhosseini, G. Roma, M. Schmidt, J. Windeln, T. D. Kühne, and C. Felser, "Hybrid-Functional Calculations on the Incorporation of Na and K Impurities into the $CuInSe_2$ and $CuIn_5Se_5$ Solar-Cell Materials", The Journal of Physical Chemistry C **119**, 25197–25203 (2015).

[118] C.-S. Lee, S. Kim, E. A. Al-Ammar, H. Kwon, and B. T. Ahn, "Effects of Zn Diffusion from (Zn,Mg)O Buffer to CIGS Film on the Performance of Cd-Free $Cu(In,Ga)Se_2$ Solar Cells", ECS Journal of Solid State Science and Technology **3**, Q99–Q103 (2014).

[119] D. Schmid, M. Ruckh, and H. W. Schock, "Photoemission studies on $Cu(In,Ga)Se_2$ thin films and related binary selenides", Applied Surface Science **103**, 409–429 (1996).

[120] C. C. Landry and A. R. Barron, "Synthesis of Polycrystalline Chalcopyrite Semiconductors by Microwave Irradiation", Science **260**, 1653–1655 (1993).

[121] J. F. Moulder, W. F. Stickle, P. E. Sobol, and K. D. Bomben, *Handbook of X-Ray Photoelectron Spectroscopy* (Perkin-Elmer Corporation, Minnesota, USA, 1992), 261 pp.

[122] P. A. Bertrand, "XPS study of chemically etched GaAs and InP", Journal of Vacuum Science & Technology **18**, 28–33 (1981).

[123] E. Laine, M. Tamminen, R. Mäkelä, and M. Pessa, "An X-ray diffraction and electron spectroscopic study of metallic glass $In_{20}Te_{80}$", Journal of Materials Science **18**, 295–298 (1983).

[124] G. E. McGuire, G. K. Schweitzer, and T. A. Carlson, "Core electron binding energies in some Group IIIa, Vb, and VIb compounds", Inorganic Chemistry **12**, 2450–2453 (1973).

[125] S. Kohiki, M. Nishitani, T. Negami, and T. Wada, "X-ray photoelectron spectroscopy of $CuInSe_2$", Physical Review B **45**, 9163–9168 (1992).

[126] A. J. Nelson, S. Gebhard, L. L. Kazmerski, E. Colavita, M. Engelhardt, and H. Höchst, "Formation and Schottky barrier height of Au contacts to $CuInSe_2$", Journal of Vacuum Science & Technology A **9**, 978–982 (1991).

[127] A. J. Nelson, S. P. Frigo, and R. Rosenberg, "Valency and type conversion in $CuInSe_2$ with H_2 plasma exposure: A photoemission investigation", Journal of Applied Physics **73**, 8561–8564 (1993).

[128] C. J. Powell, "Recommended Auger-electron kinetic energies for 42 elemental solids", Journal of Electron Spectroscopy and Related Phenomena **182**, 11–18 (2010).

[129] M. K. Bahl, R. L. Watson, and K. J. Irgolic, "LMM Auger spectra of selenium and some of its compounds", The Journal of Chemical Physics **72**, 4069–4077 (1980).

[130] N. Martensson, B. Reihl, and O. Vogt, "Binding energies and heat-of-formation data for USb_xTe_{1-x} and UAs_xSe_{1-x} compounds as derived from photoelectron spectroscopy", Physical Review B **25**, 824–829 (1982).

[131] C.-H. Ho and Y.-C. Chen, "Thickness-tunable band gap modulation in γ-In_2Se_3", RSC Advances **3**, 24896–24899 (2013).

[132] T. Löher, A. Klein, C. Pettenkofer, and W. Jaegermann, "Partial density of states in the $CuInSe_2$ valence bands", Journal of Applied Physics **81**, 7806–7809 (1997).

[133] T. V. Kuznetsova, V. I. Grebennikov, H. Zhao, C. Derks, C. Taubitz, M. Neumann, C. Persson, M. V. Kuznetsov, I. V. Bodnar, R. W. Martin, and M. V. Yakushev, "A photoelectron spectroscopy study of the electronic structure evolution in $CuInSe_2$-related compounds at changing copper content", Applied Physics Letters **101**, 111607 (2012).

[134] J. H. Scofield, "Hartree-Slater subshell photoionization cross-sections at 1254 and 1487 eV", Journal of Electron Spectroscopy and Related Phenomena **8**, 129–137 (1976).

[135] P. Reinhard, F. Pianezzi, L. Kranz, S. Nishiwaki, A. Chirilă, S. Buecheler, and A. N. Tiwari, "Flexible $Cu(In,Ga)Se_2$ solar cells with reduced absorber thickness", Progress in Photovoltaics: Research and Applications **23**, 281–289 (2015).

[136] P. E. Batson, "Carbon 1s near-edge-absorption fine structure in graphite", Physical Review B **48**, 2608–2610 (1993).

[137] F. Sette, B. Sinkovic, Y. J. Ma, and C. T. Chen, "Crystal-field splitting of core excitons in ionic crystals", Physical Review B **39**, 11125–11130 (1989).

[138] F. M. F. de Groot, J. C. Fuggle, B. T. Thole, and G. A. Sawatzky, "$L_{2,3}$ x-ray-absorption edges of d^0 compounds: K^+, Ca^{2+}, Sc^{3+}, and Ti^{4+} in O_h (octahedral) symmetry", Physical Review B **41**, 928–937 (1990).

[139] M. Yanagihara, H. Maezawa, T. Sasaki, and Y. Iguchi, "$K^+L_{2,3}$ Core Level Absorption in Potassium Halides", Journal of the Physical Society of Japan **54**, 3628–3631 (1985).

[140] S. D'Addato, D. A. C. Gregory, A. W. Robinson, A. Santaniello, C. Hellwig, C. Jung, and D. A. Evans, "An X-ray absorption spectroscopy study of the KGaAs(110) interface", Solid State Communications **93**, 11–16 (1995).

[141] Y. Ma, P. Rudolf, C. T. Chen, and F. Sette, "Potassium adsorption on the Si(100)(2x1) surface studied by Si and K core level photoemission and photoabsorption spectroscopy", Journal of Vacuum Science & Technology A **10**, 1965–1969 (1992).

[142] S. D'Addato, D. E. Ramaker, R. Cosso, D. Gregory, T. P. Morrison, P. Unsworth, L. Duò, G. Panaccione, S. Nannarone, and P. Weightman, "Charge-Transfer Satellites in K L_{23} XAS Data for K/Si(111)-(2 x 1): Evidence for Strong Ionic Bonds", EPL (Europhysics Letters) **26**, 85 (1994).

[143] T. Lepetit, S. Harel, L. Arzel, G. Ouvrard, and N. Barreau, "Coevaporated $KInSe_2$: A Fast Alternative to KF Postdeposition Treatment in High-Efficiency $Cu(In,Ga)Se_2$ Thin Film Solar Cells", IEEE Journal of Photovoltaics **6**, 1316–1320 (2016).

[144] A. Hofmann and C. Pettenkofer, "The $CuInSe_2$–$CuIn_3Se_5$ defect compound interface: Electronic structure and band alignment", Applied Physics Letters **101**, 062108 (2012).

[145] D. Rudmann, G. Bilger, M. Kaelin, F. J. Haug, H. Zogg, and A. N. Tiwari, "Effects of NaF coevaporation on structural properties of Cu(In,Ga)Se_2 thin films", Thin Solid Films, Proceedings of Symposium B, Thin Film Chalcogenide Photovoltaic Materials, E-MRS Spring Meeting **431–432**, 37–40 (2003).

[146] P. Reinhard, F. Pianezzi, B. Bissig, A. Chirila, P. Blosch, S. Nishiwaki, S. Buecheler, and A. Tiwari, "Cu(In,Ga)Se Thin-Film Solar Cells and Modules - A Boost in Efficiency Due to Potassium", IEEE Journal of Photovoltaics **5**, 656–663 (2015).

[147] S. B. Zhang, S.-H. Wei, A. Zunger, and H. Katayama-Yoshida, "Defect physics of the $CuInSe_2$ chalcopyrite semiconductor", Physical Review B **57**, 9642–9656 (1998).

[148] H. Mönig, C. H. Fischer, R. Caballero, C. A. Kaufmann, N. Allsop, M. Gorgoi, R. Klenk, H. W. Schock, S. Lehmann, M. C. Lux-Steiner, and I. Lauermann, "Surface Cu depletion of Cu(In,Ga)Se_2 films: An investigation by hard X-ray photoelectron spectroscopy", Acta Materialia **57**, 3645–3651 (2009).

[149] H. Mönig, C.-H. Fischer, A. Grimm, B. Johnson, C. A. Kaufmann, R. Caballero, I. Lauermann, and M. C. Lux-Steiner, "Surface Cu-depletion of Cu(In,Ga)Se_2 thin films: Further experimental evidence for a defect-induced surface reconstruction", Journal of Applied Physics **107**, 113540 (2010).

[150] Z. Kish, E. Peresh, V. Lazarev, and E. Semrad, "Systematics and the Rules of Variations in the Properties of the $A^I B^{III} C_2^{VI}$ - Type Compounds", Izv. Akad. Nauk SSSR, Neorg. Mater. **23**, 777 (1987).

[151] V. Lazarev, Z. Kish, E. Peresh, and E. Semrad, *Complex Chalcogenides in the A^I - B^{III} - C^{VI} Systems* (Metallurgiya, Moscow, 1993).

[152] A. Niemegeers, M. Burgelman, and A. D. Vos, "On the CdS/$CuInSe_2$ conduction band discontinuity", Applied Physics Letters **67**, 843–845 (1995).

[153] R. Klenk, "Characterisation and modelling of chalcopyrite solar cells", Thin Solid Films, Proceeedings of Symposium N on Thin Film Photovoltaicmaterials of the E-MRS Spring Conference **387**, 135–140 (2001).

[154] T. Minemoto, T. Matsui, H. Takakura, Y. Hamakawa, T. Negami, Y. Hashimoto, T. Uenoyama, and M. Kitagawa, "Theoretical analysis of the effect of conduction band offset of window/CIS layers on performance of CIS solar cells using device simulation", Solar Energy Materials and Solar Cells, PVSEC 11 - PART III **67**, 83–88 (2001).

[155] T. M. Friedlmeier, P. Jackson, D. Kreikemeyer-Lorenzo, D. Hauschild, O. Kiowski, D. Hariskos, L. Weinhardt, C. Heske, and M. Powalla, "A closer look at initial CdS growth on high-efficiency Cu(In,Ga)Se_2 absorbers using surface-sensitive methods", in 2016 IEEE 43rd photovoltaic specialists conference (PVSC) (June 2016), pp. 0457–0461.

[156] B. Ümsür, W. Calvet, A. Steigert, I. Lauermann, M. Gorgoi, K. Prietzel, D. Greiner, C. A. Kaufmann, T. Unold, and M. C. Lux-Steiner, "Investigation of the potassium fluoride post deposition treatment on the CIGSe/CdS interface using hard X-ray photoemission spectroscopy – a comparative study", Physical Chemistry Chemical Physics **18**, 14129–14138 (2016).

[157] F. Wang, X. Zhang, L. Wang, Y. Jiang, C. Wei, S. Xu, and Y. Zhao, "Improved amorphous/crystalline silicon interface passivation for heterojunction solar cells by low-temperature chemical vapor deposition and post-annealing treatment", Physical Chemistry Chemical Physics **16**, 20202–20208 (2014).

[158] F. Pianezzi, P. Reinhard, A. Chirilă, B. Bissig, S. Nishiwaki, S. Buecheler, and A. N. Tiwari, "Unveiling the effects of post-deposition treatment with different alkaline elements on the electronic properties of CIGS thin film solar cells", Physical Chemistry Chemical Physics **16**, 8843–8851 (2014).

[159] P. Jackson, D. Hariskos, R. Wuerz, O. Kiowski, A. Bauer, and M. Powalla, "Properties of High Efficiency Cu(In,Ga)Se_2 Solar Cells", 2015 MRS Spring Meeting & Exhibit; B7.02, San Francisco, Apr. 9, 2015.

[160] H. Ellis, S. K. Eriksson, S. M. Feldt, E. Gabrielsson, P. W. Lohse, R. Lindblad, L. Sun, H. Rensmo, G. Boschloo, and A. Hagfeldt, "Linker Unit Modification of Triphenylamine-Based Organic Dyes for Efficient Cobalt Mediated Dye-Sensitized Solar Cells", The Journal of Physical Chemistry C **117**, 21029–21036 (2013).

[161] E. L. Unger, A. R. Bowring, C. J. Tassone, V. L. Pool, A. Gold-Parker, R. Cheacharoen, K. H. Stone, E. T. Hoke, M. F. Toney, and M. D. McGehee, "Chloride in Lead Chloride-Derived Organo-Metal Halides for Perovskite-Absorber Solar Cells", Chemistry of Materials **26**, 7158–7165 (2014).

[162] D. E. Starr, G. Sadoughi, E. Handick, R. G. Wilks, J. H. Alsmeier, L. Köhler, M. Gorgoi, H. J. Snaith, and M. Bär, "Direct observation of an inhomogeneous chlorine distribution in $CH_3NH_3PbI_{3-x}Cl_x$ layers: surface depletion and interface enrichment", Energy & Environmental Science **8**, 1609–1615 (2015).

[163] E. Mosconi, E. Ronca, and F. De Angelis, "First-Principles Investigation of the TiO_2/Organohalide Perovskites Interface: The Role of Interfacial Chlorine", The Journal of Physical Chemistry Letters **5**, 2619–2625 (2014).

[164] J. Even, L. Pedesseau, J.-M. Jancu, and C. Katan, "Importance of Spin–Orbit Coupling in Hybrid Organic/Inorganic Perovskites for Photovoltaic Applications", The Journal of Physical Chemistry Letters **4**, 2999–3005 (2013).

[165] J. Chae, Q. Dong, J. Huang, and A. Centrone, "Chloride Incorporation Process in $CH_3NH_3PbI_{3-x}Cl_x$ Perovskites via Nanoscale Bandgap Maps", Nano Letters **15**, 8114–8121 (2015).

[166] A. Dualeh, N. Tétreault, T. Moehl, P. Gao, M. K. Nazeeruddin, and M. Grätzel, "Effect of Annealing Temperature on Film Morphology of Organic–Inorganic Hybrid Pervoskite Solid-State Solar Cells", Advanced Functional Materials **24**, 3250–3258 (2014).

[167] S. Colella, E. Mosconi, G. Pellegrino, A. Alberti, V. L. P. Guerra, S. Masi, A. Listorti, A. Rizzo, G. G. Condorelli, F. De Angelis, and G. Gigli, "Elusive Presence of Chloride in Mixed Halide Perovskite Solar Cells", The Journal of Physical Chemistry Letters **5**, 3532–3538 (2014).

[168] K. W. Tan, D. T. Moore, M. Saliba, H. Sai, L. A. Estroff, T. Hanrath, H. J. Snaith, and U. Wiesner, "Thermally Induced Structural Evolution and Performance of Mesoporous Block Copolymer-Directed Alumina Perovskite Solar Cells", ACS Nano **8**, 4730–4739 (2014).

[169] M. Scrocco, "X-ray photoemission spectra of Pb(II) halides: A study of the satellites on the core and valence bands", Physical Review B **25**, 1535–1540 (1982).

[170] G. Sadoughi, D. E. Starr, E. Handick, S. D. Stranks, M. Gorgoi, R. G. Wilks, M. Bär, and H. J. Snaith, "Observation and Mediation of the Presence of Metallic Lead in Organic–Inorganic Perovskite Films", ACS Applied Materials & Interfaces **7**, 13440–13444 (2015).

[171] R. B. Shalvoy, G. B. Fisher, and P. J. Stiles, "Bond ionicity and structural stability of some average-valence-five materials studied by x-ray photoemission", Physical Review B **15**, 1680–1697 (1977).

[172] T. G. Kim, S. W. Seo, H. Kwon, J. Hahn, and J. W. Kim, "Influence of halide precursor type and its composition on the electronic properties of vacuum deposited perovskite films", Physical Chemistry Chemical Physics **17**, 24342–24348 (2015).

[173] D. Leinen, A. Fernández, J. P. Espinós, and A. R. González-Elipe, "XPS and ISS study of $NiTiO_3$ and $PbTiO_3$ subjected to low-energy ion bombardment. I. Influence of the type of ion (Ar^+ and O^{2+})", Surface and Interface Analysis **20**, 941–948 (1993).

[174] R. Schafranek, S. Li, F. Chen, W. Wu, and A. Klein, "$PbTiO_3$/$SrTiO_3$ interface: Energy band alignment and its relation to the limits of Fermi level variation", Physical Review B **84**, 045317 (2011).

[175] H. S. Potdar, S. D. Sathaye, A. B. Mandale, and S. K. Date, "Preparation and characterization of chemically deposited thin films of lead titanate ($PbTiO_3$)", Materials Letters **9**, 71–76 (1990).

[176] B. Conings, L. Baeten, C. De Dobbelaere, J. D'Haen, J. Manca, and H.-G. Boyen, "Perovskite-Based Hybrid Solar Cells Exceeding 10% Efficiency with High Reproducibility Using a Thin Film Sandwich Approach", Advanced Materials **26**, 2041–2046 (2014).

[177] T. L. Barr, M. Yin, and S. Varma, "Detailed x-ray photoelectron spectroscopy valence band and core level studies of select metals oxidations", Journal of Vacuum Science & Technology A **10**, 2383–2390 (1992).

[178] C. Hinnen, C. Nguyen van Huong, and P. Marcus, "A comparative X-ray photoemission study of $Bi_2Sr_2CaCu_2O_{8+\delta}$ and $Bi_{1.6}Pb_{0.4}Sr_2CaCu_2O_{8+\delta'}$", Journal of Electron Spectroscopy and Related Phenomena **73**, 293–304 (1995).

[179] C. Hartmann, G. Sadoughi, R. Félix, E. Handick, H. W. Klemm, G. Peschel, E. Madej, A. B. Fuhrich, X. Liao, S. Raoux, D. Abou-Ras, T. Schmidt, R. G. Wilks, H. Snaith, and M. Bär, "X-PEEM investigation of chemical and electronic surface properties of solution processed perovskite-based thin-film solar cell structures", (2016).

[180] L. Huang, Z. Hu, G. Yue, J. Liu, X. Cui, J. Zhang, and Y. Zhu, "$CH_3NH_3PbI_{3-x}Cl_x$ films with coverage approaching 100% and with highly oriented crystal domains for reproducible and efficient planar heterojunction perovskite solar cells", **17**, 22015–22022 (2015).

[181] D. O. Scanlon, C. W. Dunnill, J. Buckeridge, S. A. Shevlin, A. J. Logsdail, S. M. Woodley, C. R. A. Catlow, M. J. Powell, R. G. Palgrave, I. P. Parkin, G. W. Watson, T. W. Keal, P. Sherwood, A. Walsh, and A. A. Sokol, "Band alignment of rutile and anatase TiO_2", Nature Materials **12**, 798–801 (2013).

[182] J. Kim, S.-C. Lee, S.-H. Lee, and K.-H. Hong, "Importance of Orbital Interactions in Determining Electronic Band Structures of Organo-Lead Iodide", The Journal of Physical Chemistry C **119**, 4627–4634 (2015).

[183] H. Tang, F. Lévy, H. Berger, and P. E. Schmid, "Urbach tail of anatase TiO_2", Physical Review B **52**, 7771–7774 (1995).

[184] M. Landmann, E. Rauls, and W. G. Schmidt, "The electronic structure and optical response of rutile, anatase and brookite TiO_2", Journal of Physics: Condensed Matter **24**, 195503 (2012).

[185] J. Pascual, J. Camassel, and H. Mathieu, "Fine structure in the intrinsic absorption edge of TiO_2", Physical Review B **18**, 5606–5614 (1978).

[186] E. M. Miller, Y. Zhao, C. C. Mercado, S. K. Saha, J. M. Luther, K. Zhu, V. Stevanović, C. L. Perkins, and J. v. d. Lagemaat, "Substrate-controlled band positions in $CH_3NH_3PbI_3$ perovskite films", Physical Chemistry Chemical Physics **16**, 22122–22130 (2014).

[187] T. Leijtens, S. D. Stranks, G. E. Eperon, R. Lindblad, E. M. J. Johansson, I. J. McPherson, H. Rensmo, J. M. Ball, M. M. Lee, and H. J. Snaith, "Electronic Properties of Meso-Superstructured and Planar Organometal Halide Perovskite Films: Charge Trapping, Photodoping, and Carrier Mobility", ACS Nano **8**, 7147–7155 (2014).

[188] S. M. Sze and K. K. Ng, *Physics of Semiconductor Devices*, 3rd (John Wiley & Sons, Hoboken, New Jersey, USA, Nov. 3, 2006), 828 pp.

Own Publications

First Author Publications

- **Evelyn Handick**, Patrick Reinhard, Regan G. Wilks, Fabian Pianezzi, Thomas Kunze, Dagmar Kreikemeyer-Lorenzo, Lothar Weinhardt, Monica Blum, Wanli Yang, Mihaela Gorgoi, Eiji Ikenaga, Dominic Gerlach, Shigenori Ueda, Yoshiyuki Yamashita, Toyohiro Chikyow, Clemens Heske, Stephan Buecheler, Ayodhya N. Tiwari, and Marcus Bär, "Formation of a K-In-Se surface species by NaF/KF post-deposition treatment of Cu(In,Ga)Se_2 thin-film solar cell absorbers", ACS Applied Materials & Interfaces **9**, 3581-3589 (2017).
- **Evelyn Handick**, Patrick Reinhard, Regan G. Wilks, Fabian Pianezzi, Roberto Félix, Mihaela Gorgoi, Thomas Kunze, Stephan Buecheler, Ayodhya N. Tiwari, and Marcus Bär, "NaF/KF Post-Deposition Treatments and their Influence on the Structure of Cu(In,Ga)Se_2 Absorber Surfaces", Proceedings of the *43rd* IEEE Photovoltaic Specialist Conference (PVSC), 0017–0021 (2016).
- **Evelyn Handick**, Patrick Reinhard, Jan-Hendrik Alsmeier, Leonard Köhler, Fabian Pianezzi, Stefan Krause, Mihaela Gorgoi, Eiji Ikenaga, Norbert Koch, Regan G. Wilks, Stephan Buecheler, Ayodhya N. Tiwari, and Marcus Bär, “Potassium postdeposition treatment-induced band gap widening at Cu(In,Ga)Se_2 surfaces – reason for performance leap?”, ACS Applied Materials & Interfaces **7**, 27414–27420 (2015).

Co-Author Publications

- Dirk Hauschild, **Evelyn Handick**, Sina Göhl-Gusenleitner, Frank Meyer, Holger Schwab, Andreas Benkert, Stephan Pohlner, Jörg Palm, Sven Tougaard, Clemens Heske, Lothar Weinhardt, and Friedrich Reinert, "Band-Gap Widening at the Cu(In,Ga)(S,Se)$_2$ Surface - A Novel Determination Approach Using Reflection Electron Energy Loss Spectroscopy", ACS Applied Materials & Interfaces, **8**, 21101 (2016).

- David E. Starr, Golnaz Sadoughi, **Evelyn Handick**, Regan G. Wilks, Jan-Hendrik Alsmeier, Leonard Köhler, Mihaela Gorgoi, Henry Snaith, and Marcus Bär, "Observation and Mediation of the Presence of Metallic Lead in Organic- Inorganic Perovskite Films" G. Sadoughi, ASC Applied Materials & Interfaces, **7**, 13440 (2015).

- Golnaz Sadoughi, David E. Starr, **Evelyn Handick**, Samuel D. Stranks, Mihaela Gorgoi, Regan G. Wilks, Marcus Bär, and Henry J. Snaith,"Direct observation of an inhomogeneous chlorine distribution in $CH_3NH_3PbI_{3-x}Cl_x$ layers: surface depletion and interface enrichment", Energy & Environmental Science, **8**, 1609 (2015).

- Sina Gusenleitner, **Evelyn Handick**, Dirk Hauschild, and Friedrich Reinert, "Quantitative analysis of electron energy loss spectra and modelling of optical properties of multilayer systems for extreme ultraviolet radiation regime", Journal of Applied Physics, **115**, 123513 (2014).

Acknowledgments

Last but not least I want to thank all those people without this thesis would not have been possible.

First I would like to thank *Prof. Dr. Marcus Bär* for giving me the opportunity to work in his young investigator group on these interesting topics. For me he was the best supervisor and mentor a PhD student could hope for, being always passionate and enthusiastic about our research and of course the spectroscopy techniques within our "tool chest". He gave me the opportunity to decide my sample systems of choice, had always an open door for data discussion, when help was needed, and for all other problems. Further he financially supported my research and provided me with the possibilities to measure at different synchrotrons and attend various conferences around the world.
I would like to thank *Prof. Dr. Bernd Rech* for being my substitute-advisor at HZB always giving input and feedback on my progress reports and being a reviewer of this thesis. Further I want to thank *Prof. Dr. Dieter Schmeißer* for being reviewer and *Prof. Dr. Michael Bestehorn* as well as *Prof. Dr. Götz Seibold* for being part of my PhD committee.
I am also grateful to *Dr. Regan G. Wilks* for his constant help and feedback on data analysis and interpretation, always being there for us PhD students, and for always being in the mood for good meat.
I am thankful to *Dr. David E. Starr* who convinced and introduced me to the perovskite research and the plenty of fun hours in the chemistry lab and the office with lots of "psychologically" valuable discussions about life.
Leonard Köhler my Kesterite counterpart, who not only became a college on our first day at HZB but a good friend of mine during our PhD period. In this context I would also like to thank *Jan-Hendrik Alsmeier* for introducing me to the solar cell research and building a

good team with me and Leo within and outside of HZB.
I am grateful to *Dr. Patrick Reinhard*, *Dr. Stephan Buecheler*, and *Prof. Dr. Ayodhya N. Tiwari* from Laboratory of Thin Films and Photovoltaics at Empa-Swiss Federal Laboratories for Materials and Science and Technology for providing me with the sample series I based my entire chalcopyrite research on. I would also like to thank *Dr. Golnaz Sadoughi* and *Prof. Dr. Henry J. Snaith* from the Department of Physics, Clarendon Laboratory at University of Oxford for providing the perovskite samples. I appreciated the collaboration with you, the constant input, data discussion and analysis, and your steady feedback. Thank you for giving me the opportunity to be a part of your research groups.
I appreciate the help of *Dr. Thomas Kunze* taking over the lab in Wannsee and being a first contact person in case help was needed. I also want to thank all the past and present members of the EE-NI group.
To the "extended KIT/UNLV/Uni Würzburg family" I thank for the fun times at the ALS in Berkeley during beamtimes, filled with lots of coffee, good food, Thanksgiving dinners, (blackfriday) shopping, and the constant feedback and comments; and here in particular *Dr. Dagmar Kreikemeyer-Lorenzo*, *Dr. Monika Blum*, *Andreas Benkert*, *Dr. Frank Meyer*, *Dr. Dirk Hauschild*, *Dr. Lothar Weinhardt*, and *Prof. Dr. Clemens Heske*.
I am thankful to *Dr. Stefan Krause* and *Prof. Dr. Norbert Koch* for giving me the opportunity to do IPES in their lab and *PD Dr. Daniel Abou-Ras* for doing the SEM and EDX measurements.
Also our visiting scholars *Dr. Michelle Mezher*, *Dr. Riley E. Brandt*, and *Dr. Serge Smolin* for helping getting the lab back running and becoming good friends and travel companions.
Thank you to all my friends within and outside of HZB, especially *Shun*, *Annegret*, and *Nicole* for reminding me that there is more to life than research, keeping me motivated and always being there when I needed someone to talk to.

A big thank you to my older sister *Daniela* who is always there for me in any possible way I could hope for and her husband *Lukas*, who became more like a big brother over the years. She was always the person I looked up to the most and still do.

Finally *my parents* who taught me that I can achieve any goal life if I work for it without giving up. Their constant believe in me kept me going even in times I had my own doubts that I can finish. They supported me financially throughout my entire study but most importantly I am grateful for their love and support throughout my whole life.

Declaration of Academic Integrity

I, Evelyn Handick, declare that this dissertation titled

'Surface and Interface Characterization by X-ray and Electron Spectroscopies - Revealing the Peculiarities of Cu(In,Ga)Se_2 Chalcopyrite and $CH_3NH_3PbI_{(3-x)}Cl_x$ Perovskite-based Thin Film Solar Cell Structures'

and the work presented in it is my own. I confirm that this work was done wholly or mainly while in candidature for a research degree at this University. No part of this thesis has previously been submitted for a degree or any other qualification at this University or any other institution. This thesis is my first submission for a PhD degree at any institution. Where I have consulted the published work of others, this is always clearly attributed. Where I have quoted from the work of others, the source is always given. With the exception of such quotations, this thesis is entirely my own work. I have acknowledged all main sources of help. Already published or submitted parts of this thesis are clearly indicated.